Force calibration and wavefield synthesis for acoustical tweezers

Dan Zhao

SORBONNE UNIVERSITÉ
CRÉATEURS DE FUTURS DEPUIS 1257

Sorbonne Université

École Doctorale de Sciences Mécaniques, Acoustique, Électronique et Robotique de Paris (SMAER ED391)

Thèse de doctorat

Force Calibration and Wavefield Synthesis for Acoustical Tweezers

Par Dan ZHAO

Thèse de doctorat d'Acoustique Physique

Dirigée par : Jean-Louis Thomas et Régis Marchiano

Présentée et soutenue publiquement le : 29/11/2019

Devant un jury composé de :

M. Jean-Louis Thomas	Directeur de Recherche	Directeur de thèse
M. Régis Marchiano	Professeur	Co-directeur de thèse
Mme. Hélène Bailliet	Maître de conférences	Rapporteur
M. Valentin Leroy	Directeur de Recherche	Rapporteur
M. Régis Wunenburger	Professeur	Examinateur
M. Thomas Brunet	Maître de conférences	Examinateur

Abstract

Single beam acoustical tweezers have been developed and applied to numerous applications in biological and biochemical domains. Their application in precise manipulations requires accurate control of the acoustical trap. This work sets out to calibrate the force exerted by acoustical tweezers and synthesize the desired wavefield.

The single beam acoustical tweezers are achieved by a focused vortex beam. An object in interaction with the acoustic waves is trapped thanks to the radiation pressure. This three-dimensional force can be obtained by knowing the incident beam shape coefficients as well as the scattering coefficients. Therefore, the computation of the forces can be achieved by measuring the wavefield. The first part of the thesis concentrates on assessing different methods to compute the beam shape coefficients from the pressure field to estimate the radiation force exerted on an elastic sphere. Then, in the second part, the synthesis of the field using the inverse filtering method is carried out. A proper synthesis of the field requires a suitable distribution of control points where the wave propagation information is recorded. To synthesize the appropriate vortex beam, three kinds of distributions were compared.

For the single beam acoustical tweezers, the most challenging part is the axial restoring force. In order to overcome this difficulty, the spherical vortex beam with high pressure gradient in the axial direction is introduced. This spherical vortex beam is intended to trap large spheres with diameters close to the wavelength. The feasibility of this vortex is analyzed numerically and experimentally.

Keywords: nonlinear acoustics, radiation pressure, acoustical tweezers, calibration, wavefield synthesis, scattering

Résumé

Les pinces acoustiques à faisceau unique ont été développées et appliquées à de nombreuses applications dans les domaines biologiques et biochimiques. Leur application lors de manipulations précises nécessite une connaissance complète des forces appliquées sur l'objet. Ce travail a pour objectif de calibrer la force exercée par une pince acoustique et de synthétiser le champ d'onde souhaité.

Les pinces acoustiques à faisceau unique sont réalisées par un faisceau vortex focalisé. Un objet en interaction avec les ondes acoustiques est piégé grâce à la pression de radiation. Cette force tridimensionnelle peut être obtenue en connaissant les coefficients du champ incident ainsi que les coefficients de diffusion. Par conséquent, le calcul des forces peut être réalisé en mesurant le champ incident. La première partie de la thèse se concentre sur l'évaluation de différentes méthodes permettant de calculer ces coefficients du champ incident à partir de la mesure du champ de pression calibré. Ensuite, dans la deuxième partie, le champ est synthétisé en utilisant la méthode du filtre inverse. L'efficacité de cette méthode dépend de la distribution des points de contrôle. Les choix de distribution sont comparés.

Pour les pinces acoustiques, une difficulté majeure est d'obtenir une force de rappel axiale d'amplitude suffisamment large pour compenser le poid de la sphère. Afin de surmonter cette difficulté, un nouveau champ de type vortex sphérique est introduit. Ce champ est destiné à piéger de grandes sphères de diamètres proches de la longueur d'onde afin d'obtenir en plus des forces de grande amplitude, une sélectivité améliorée de la pince. La faisabilité de ce vortex est analysée numériquement et expérimentalement.

Mots-clés : acoustique nonlinéaire, pression de radiation, pince acoustique, calibration, synthèse du champ, diffusion

Acknowledgements

This work was supported by French state funds managed by the ANR within the In-405 vestissements d'Avenir programme under reference ANR-11-IDEX-0004-02, and more specifically within the framework of the Cluster of Excellence MATISSE led by Sorbonne Universites.

First and foremost, I would like to express my sincere gratitude to my supervisors Jean-Louis Thomas and Régis Marchiano, for their continuous support and guidance of my PhD study and research. I am grateful not only for their insightful suggestions and comments to my questions but also for their patience and supportive encouragement. Our discussions have always been illuminating and I was really impressed by their good sense of humor which made the discussion more interesting and delightful. Without their guidance, I would not have been able to accomplish my thesis.

I would also like to thank the members of the jury: Mme. Bailliet Hélène, M. Leroy Valentin, M. Wunenburger Régis, and M. Brunet Thomas. It is no doubt a laborious and time-consuming process to read the thesis and I am grateful for their precious time evaluating this work.

I also have the great pleasure to express my gratitude for my colleagues in Institut des NanoSciences de Paris and Institut Jean Le Rond d'Alembert for always being friendly. They are always willing to give a hand without hesitation. I appreciate the time we spent together for lunch and coffee, as well as the moments we laughed together. The atmosphere between colleagues has always been relaxing and enjoyable. This priceless time together is an unexpected gift for my life.

My heartfelt appreciation goes to my friends in Paris, who are like my family in France. I am grateful for the moments we spent with each other, for taking care of me when I didn't feel good, for the companionship that saved me out of loneliness. Special thanks to my friends Yuxi and Angus for helping to correct the English writing of this thesis.

I would like to express my gratitude for the administrative team in both Institut des NanoSciences de Paris and Institut Jean Le Rond d'Alembert for all the assistance in the

administrative procedures and thank you all for being patience and kind. I would like to mention and thank Simona Otarasanu for being the sunshine of Institut Jean Le Rond d'Alembert with her smile and humorous words.

Last but not least, I would like to thank my parents for their support during the past three years. Without their unconditional support and encouragement, I would not have been able to walk this far to get this degree. And I also would like to thank my little brother for being with our parents when I am far away from them.

Contents

Chapter 1

Context and objectives

Contactless manipulation technologies are critical for numerous biological studies and applications: cellular interaction, DNA and RNA replication and segregation, microparticles transportation, separation and selection of cells and bacteria, etc. Technical devices such as optical, magnetic, and acoustic tweezers are developed and employed in biological experiments to study small objects, including cells and proteins. These micro manipulators are in strong demand in the field of biophysics. Among these tweezers, optical tweezers [1, 2, 3, 4] have been developed and used first because of their precision and trap capabilities. In 1971, Arthur Ashkin first developed a stable optical levitator based on counterpropagating laser beams. 15 years later [2], the first single beam optical tweezers were realized by Arthur Ashkin using a tightly focused light beam that gives rise to a more accurate control of trapping. However, the high intensity focus of optical tweezers can lead to photo-damage and heating [5, 6] of the target object, especially for *in vivo* samples. In addition, the applications of optical tweezers are limited by their force range, from 0.1 to 100 pN [7]. Thus, the optical tweezers are suitable for manipulations at the sub-cellular levels. As for the studies on the scale of larger organisms, the optical forces are minuscule. Magnetic tweezers can avoid photo-damage compared to optical tweezers. They are widely used in the biology field, especially for manipulation and analyses of DNA and RNA [8, 9]. The main drawback of magnetic tweezers is the limited range of constant force. Besides, the target objects are limited to magnetic particles or require pre-tagging (attach or bind magnetic particles to the target object) [7]. Moreover, applying large force requires high-current electromagnets which would cause heating or production of non constant-force. The radiation force is proportional to the energy density divided by the speed of propagation. As the velocity

of light is 5 orders of magnitude larger than sound speed, acoustic tweezers can afford large forces with much smaller intensity than optical tweezers. The acoustic tweezers are, therefore, a solution for the heating issue. Moreover, no pre-tagging is required for acoustic tweezers and the sizes of the trapped particle range from hundred nanometers to millimeter. This advantage emphasizes their potential for *in vivo* studies and enables a wide range of applications in various domains: materials science, biophysical properties of cells and molecules, micro-rheology, and biophysical characterization of DNA, etc.

As acoustic tweezers are anticipated as a powerful tool with numerous advantages, different kinds of acoustic traps are developed. Early studies of the acoustic traps[10, 11] were based on plane standing waves to trap particles at the nodes or anti-nodes. Among the studies of the acoustic radiation pressure, Gorkov [12] proposed an approach to obtain the radiation force on objects much smaller than the acoustic wavelength in an acoustic field due to standing waves. According to Gorkov's expression, the radiation pressure of standing waves could be written as a gradient force. His theory is widely used and has accelerated the development of acoustic trap by standing waves. The first acoustic tweezers are investigated by Wu [13] using two collimated focused ultrasonic beams propagating along opposite directions with which radial selectivity was achieved [see Fig. 1.1- (1)]. Latex particles and clusters of frog eggs were trapped in the potential well. Acoustic levitation, known for a longtime [14, 15], has achieved significant success in many research areas, such as measurement of liquid surface tension [16], studies on liquid droplets [17, 18, 19] and biochemical analysis [20]. The simplest configurations of acoustic levitator is called single-axis acoustic levitator. It can be formed by a single transducer and a reflector [15, 21, 22], by two opposing transducers [17] or by two opposing arrays of transducers [23]. Xie and Wei have demonstrated a single-axis device [24] that allows stable levitation of high-density solid sphere, liquid droplet [21], and even living animals [25]. As illustrated in Fig. 1.1-(2) and (3), an iridium sphere and a mercury drop are both trapped in the levitator; small animals like ant, ladybug, and small fish are levitated without losing their vitality. Standing surface acoustic waves (SSAWs) can also create acoustic traps, which have opened up a new area for the development of particle sorting. In microfluidics systems, 'acoustophoresis' describes the effect of radiation pressure acting on particles in suspension when exposed to an acoustic standing wave field. It is widely applied to manipulate micro objects

[26] (particle, bubble, droplet, etc.) like patterning[27, 28, 29], separation and transportation [30, 31, 32, 33, 34, 35]. The radiation force exerting on gas bubbles in interaction with sound waves, known as Bjerknes force, have been used to manipulate gas bubbles [36, 37]. Recently, the SSAWs have been extensively utilized in the biological field to separate cells [38, 39, 40] due to their noninvasiveness. Some of the SSAWs' applications are represented in Fig. 1.2: (1) an effective microparticle patterning system established by SSAWs; (2) droplets with different densities sorted by SSAWs; (3) nanoscale particle sorting using two-stage SSAWs (separation of exosomes from blood); (4) separation of lipid particles from red blood cells with efficiency close to 100%.

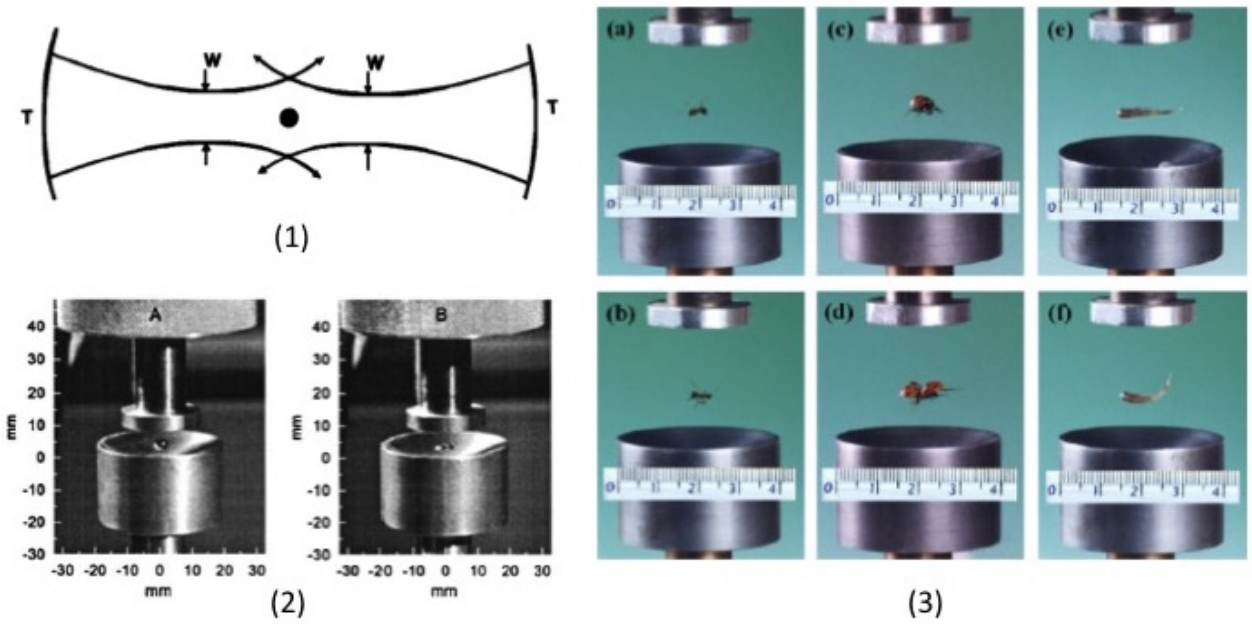

Figure 1.1: (1) Two focused collimated ultrasonic beams propagating along opposite directions a reused to generate a force potential well to trap a spherical particle.T represents a focusing PZT transducer. W is the beam width at its focal point. (2) Single-axis acoustic levitation of an iridium sphere and a mercury drop. (3) Acoustic levitation of small living animals by a resonant single-axis device (Reprinted from [13, 21, 25]).

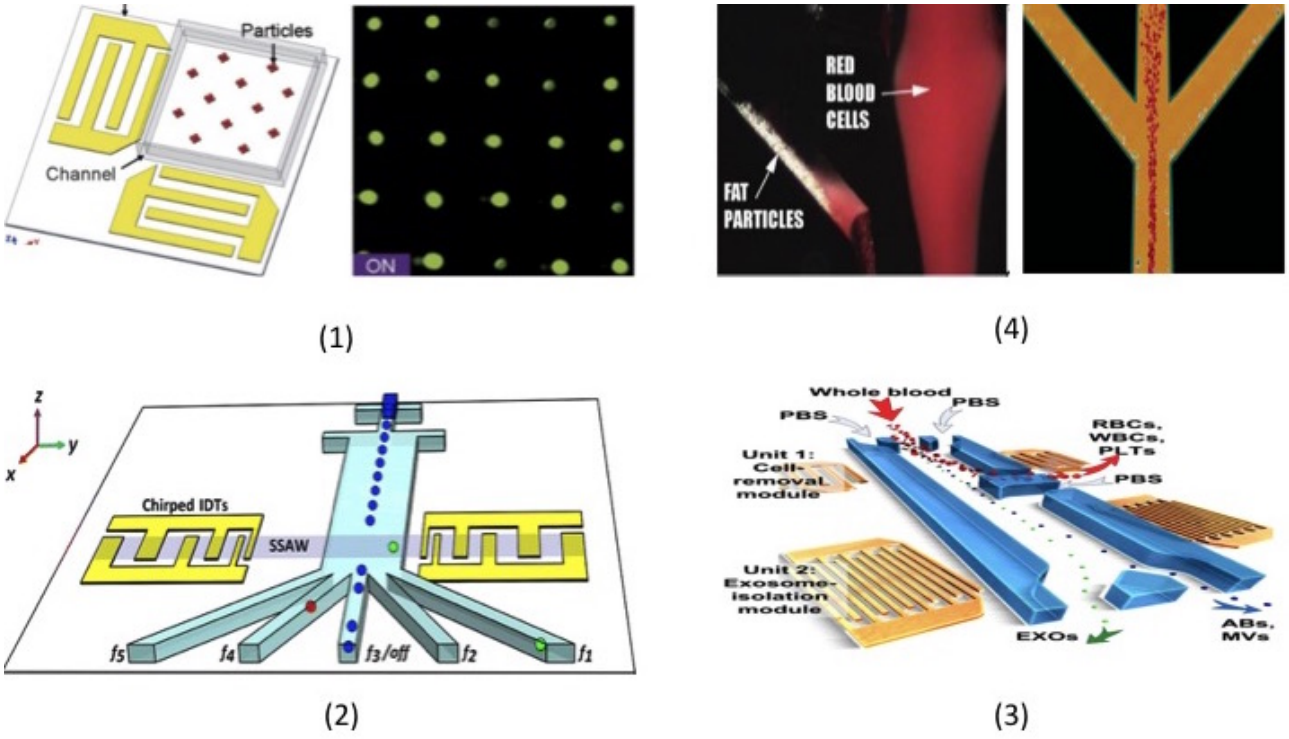

Figure 1.2: (1) Particles patterned into dot clusters in a 2D standing acoustic field [27]. (2) Schematic of the SSAW-based multichannel droplet sorter constructed by two interdigital transducers (IDTs). [34]. (3) Separation of nanoparticles (exosomes) from blood using two-stage SSAWs [40]. (4)Acoustic separation of human lipid particles and human erythrocytes by different compressibility [41].

In these schemes, all pressure nodes (or anti-nodes depending on the object density and compressibility) act as potential traps. Although the standing wave fields are of significance in collective manipulation of multiple objects or for particles sorting, all those acoustic trapping devices require more than one transducer , and trapped targets which must be located between these transducers. Furthermore, the multiplicity of nodes and anti-nodes precludes any selectivity. On the contrary, optical tweezers are selective traps with a single position of equilibrium. Regarding the advantage of three-dimensional manipulation, the single beam acoustic trap is developed [42, 43, 44]. A recent study demonstrated the feasibility and efficiency of single beam acoustic tweezers. They are characterized by the ability to pick up, trap and manipulate a single small elastic particles in three dimensions [45, 42, 46, 47] as its optical counterpart [48, 49, 50].

The solution to build a single beam acoustic tweezers has been to tailor the incident field

with a focused acoustic vortex. Acoustic vortices are the acoustical equivalent of optical vortices [51], with a helical type of wavefront and a phase singularity at the center of helicoid as shown in Fig. 1.3-(1). The helicoidal beams carry orbital angular momentum that can be transferred to particles and induce rotation [52, 53]. The variation of the phase has a jump of $2m'\pi$ when it undergoes a circle around the center of the vortex. The topological charge, m', is an integer. The sign of the topological charge depends on the direction of rotation through which the phase has positive jumps: positive for counterclockwise and negative for clockwise. On the axis of propagation, since the phase is undefined, the corresponding amplitude of the wave is zero and forms a dark core. Therefore, the amplitude pattern of the vortex beam presents a ring shape, as shown in Fig. 1.3-(2). It is also called a 'doughnut mode'. With the doughnut-shaped intensity distribution, it is possible to trap the targets at the core of acoustic vortex. The radius of the ring grows larger as the topological charge increases. Different types of acoustic vortex abased on their shape of wavefront will be presented later in the following section.

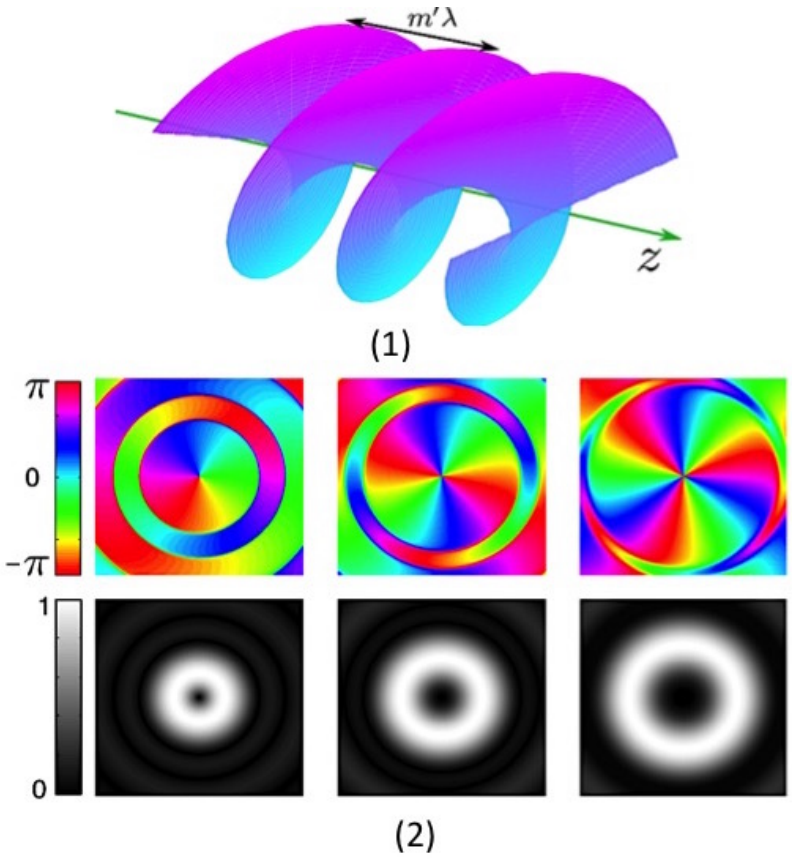

Figure 1.3: (1)Planes of constant phase for a wavefront containing a screw dislocation (helicoidal wavefront). The phase winds around the axis of propagation z and the pitch of the helix is fixed by the topological charge m'. (2) Phase front and corresponding intensity distribution for vortex with topological charge $m' = 1, 2, 3$ (from left to right) [45].

For all the possible applications, the calibration of the force provided by acoustic tweezers is crucial, especially for micro-rheology studies. The optical and magnetic tweezers' forces calibration is achieved mainly by two methods: the first one studies the Brownian motion of trapped objects with sizes comparable to the wavelength, then the force is determined from Hooke's law [54, 55]; the second one uses the viscous drag generated by fluid flow with force determined by Stokes' law [56].

However, the first method is not applicable for acoustic tweezers because the wavelength and the object can be much larger than those of optical tweezers, and the Brownian motion disappears at these scales. As for the second method, the fluid drag forces are also used to calibrate the acoustic trapping force [57], but difficulties arise for single beam acoustic tweezers due to the Magnus effect caused by the rotation of bead in an acoustic vortex beam [58].

The computation of the acoustic radiation force on spherical particles has been developed

for different kinds of wavefields. The study began with a plane wave [10, 59, 60, 61]. Then, the radiation pressure exerted by some more complicated beams such as: focused axisymmetric beams [62, 63, 64], helicoidal Bessel beam [65, 66, 67] were established. Thereafter, the studies were extended to arbitrary wavefront [68, 69, 70, 71]. In viscous fluid, The viscosity correction of the radiation force was considered [72]. Furthermore, the approximation of the radiation force on an object of arbitrary shape in a plane standing wave was also demonstrated [73]. For the force prediction of the single beam acoustic tweezers, we will introduce a new method in this paper. This method is not a direct measurement of the force but allows characterizing the radiation force by measuring the acoustic pressure field of an arbitrary acoustic beam. Previously, the three-dimensional force exerted on a spherical particle was modeled using the incident beam expansion on spherical harmonics. This model depends on the dubbed beam shape coefficients (BSC), A_n^m, and the scattering coefficients of the particle, R_n [74]. As the scattering coefficient depends only on the physical characteristics of the object and propagation medium, we aim to determine the BSC according to the incident acoustic beam pressure. Therefore, our study is divided into four parts. In the first chapter, we introduce the analytical model of radiation force exerted on an elastic sphere. The second chapter consists of different methods with which we determine the BSC. Then, in the third chapter, the inverse filtering method is employed to synthesize the vortex beams. Consequently, the acoustical trapping and manipulating by the vortex beams are experimentally carried out in the last chapter.

Chapter 2

Acoustic radiation force

2.1 Derivation of the acoustic radiation force

This chapter is a compact version of the derivation of the acoustic radiation force on an elastic sphere proposed by Baresch in his thesis [45].

2.1.1 Historical scalar theory

The acoustic radiation pressure is a nonlinear effect that characterizes the average force exerted on an object interacting with the acoustic wave. In 1905, Rayleigh [75] published his work with the first expression of acoustic radiation pressure which depends on the nonlinearity of the medium.

$$\mathcal{P}_R = \beta < E > . \tag{2.1}$$

Where $< E >$ is the time-averaged energy density and β the coefficient of nonlinearity of the medium. This expression can be used under the hypothesis that a plane wave is confined in its propagation medium without communication with the outside environment at rest. After Rayleigh's study, Langevin [76] gives another expression of the radiation pressure in which the plane wave is no longer confined but can communicate with the rest of the medium at rest:

$$\mathcal{P}_L =< E > . \tag{2.2}$$

The expression of Rayleigh Pressure is in agreement with the results of Hertz and Mende

[77]. However, the conditions necessary are too theoretical to obtain this expression. Indeed, communication with the resting medium is inevitable in a free medium. Thus, the experimental configurations lead mainly to the Langevin radiation expression. Another example of Langevin radiation pressure is the radiation force balances that are designed specifically for easy ultrasound power measurements on high power devices.

These theories are scalar, and their range of validity is restricted to plane longitudinal waves incident on plane targets. This is in contrast with optic radiation pressure that was modeled by Maxwell and is given by the Maxwell tensor. A more generic modeling in acoustics accounting for arbitrary wavefronts, targets, and wave polarization was developed by Brillouin and is described in the next section.

2.1.2 Modern tensorial theory

The tensorial nature of radiation pressure was developed in two papers [78, 79] published in French. A translation in English appeared in 1938 [80]. The force exerted by external forces on a portion of a solid is the integral on its surface of the Cauchy stress (minus the pressure for an ideal fluid). The radiation force, i.e radiation pressure, is the mean value of this quantity. In the following, we consider harmonic waves only (steady regime) and hence the time average can be performed on an acoustic period, $T = 2\pi/\omega$.

$$\mathcal{F}_i = -\frac{1}{T}\int_0^T \left(\int_{S(t)} p n_i dS\right) dt = - < \int_{S(t)} p n_i dS > . \tag{2.3}$$

Where $p(\vec{x}, t)$ is the total pressure field in the fluid, index i stands for the axis considered, and $\vec{n}$ is the unit vector normal to the surface of the object and pointing outward. It is an average effect that should be distinguished from the instantaneous force applied to the object that only contributes to the oscillation of it and can be computed in the linear approximation. An acoustic field is, by definition, a local change of particle position and stress. The surface $S(t)$ of the object is, therefore, in oscillation and makes the calculation of the average force a nonlinear process. One possible solution to alleviate this difficulty consists in writing the radiation force in Lagrangian coordinates. However, calculating the net force in Lagrangian coordinates is computationally complicate and not always feasible for fluids. Below, we give a

reminder of the method used to come back to a fixed surface and in Eulerian coordinates.

Fixed surface in Eulerian coordinates

The first step is to write the continuity equation for momentum [81]:

$$\frac{\partial \rho v_i}{\partial t} + \frac{\partial \Pi_{ij}}{\partial x_j} = 0, \tag{2.4}$$

with:

$$\Pi_{ij} = p\delta_{ij} + \rho v_i v_j. \tag{2.5}$$

Where v_i, v_j is the fluid velocity, ρ is the density and Π_{ij} is the momentum flux tensor. By integrating the Eq. (2.4) on the volume contained between the vibrating surface $S(t)$ and a fixed surface S_R surrounding the object (see Fig. 2.1), using the divergence theorem, we obtain:

$$\int_{V(t)} \frac{\partial \rho v_i}{\partial t} dV + \int_{S(t)} \Pi_{ij} n'_j dS + \int_{S_R} \Pi_{ij} n_{Rj} dS = 0. \tag{2.6}$$

with $\vec{n}' = -\vec{n}$ the normal to the surface $S(t)$ of the object but pointing inward and $\vec{n}_R$ the normal outgoing vector at the surface S_R.

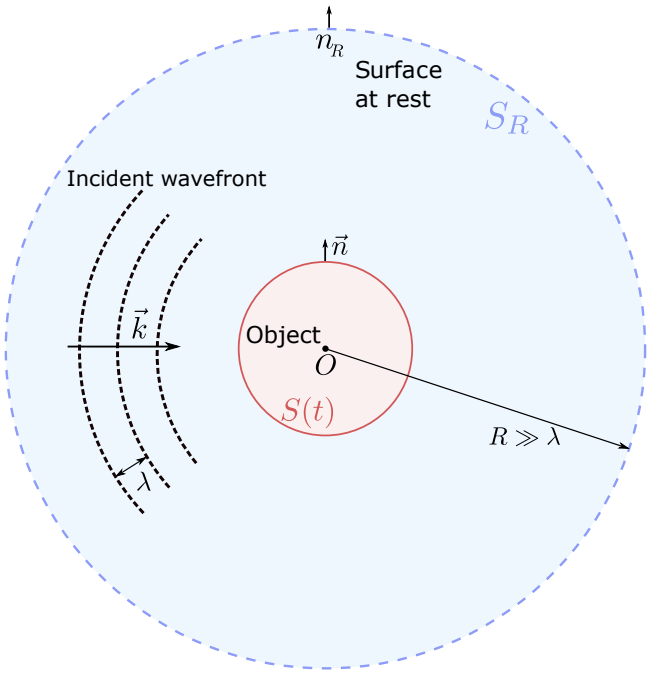

Figure 2.1: Geometry and notations used of the calculation of the force exerted on a particle by an incident acoustic wave [45].

It is now appropriate to re-express the left side of Eq. (2.6) using the Reynolds transport theorem:

$$\frac{\partial}{\partial t}\int_{V(t)} \rho v_i dV = \int_{V(t)} \frac{\partial \rho v_i}{\partial t} dV + \int_{S(t)} \rho v_i v_j n'_j dS. \tag{2.7}$$

Using this theorem, the continuity relation can be written as:

$$\frac{\partial}{\partial t}\int_{V(t)} \rho v_i dV + \int_{S(t)} (\Pi_{ij} - \rho v_i v_j) n'_j dS = -\int_{S_R} \Pi_{ij} n_{Rj} dS_R. \tag{2.8}$$

We now take the average in time of Eq. (2.8). Using the fact that the mean of a time derivative cancels the first term of left hand side. The integrand of the second term is the pressure field and taking into account $\vec{n}' = -\vec{n}$ is the force expression of Eq. (2.3). The force then is expressed by:

$$F_i = -\int_{S_R} < \Pi_{ij} > n_{Rj} dS, \tag{2.9}$$

where $< \Pi_{ij} >$ is named the Brillouin radiation tensor with the following expression:

$$< \Pi_{ij} >=< p > \delta_{ij} + < \rho v_i v_j > . \tag{2.10}$$

For the Brillouin expression of the radiation force, we notice that no hypothesis is necessary on the shape of the object. The average force can therefore be obtained from this integrated tensor on an immobile surface completely surrounding any object. A second order approximation of Π_{ij} is the first non zero contribution $< \Pi_{ij} >$ and is generally sufficient for acoustic wave of finite amplitude. This approximation is discussed in the next part.

Second order approximation

For any acoustics fields, α, is decomposed into a perturbative series at second order:

$$\alpha \approx \alpha_0 + \alpha_1 + \alpha_2. \tag{2.11}$$

with α_0 the value at rest, α_1 the linear acoustic field with $< \alpha_1 >= 0$ and $\alpha_2 \ll \alpha_1$ the second order contribution. For the Reynolds tensor, the second order approximation is obvious : $\rho v_i v_j \approx \rho_0 v_{1i} v_{1j}$. The second order approximation of the pressure field in Eulerian coordinates is given by the second relation of Langevin [82, 83, 84]:

$$p \approx p_0 + \frac{1}{2}\frac{p_1^2}{\rho_0 c_0^2} - \frac{1}{2}\rho_0 \vec{v}_1^2 + C(t). \tag{2.12}$$

Where $C(t)$ is a function of time that only depends on the boundary condition in the far field. The radiation force, Eq. (2.9), results from integration on a closed surface, and hence any constant pressure like term have a null contribution. Thus, the term $(p_0 + C(t))\delta_{ij}$ can be dropped. The expression of Brillouin tensor then becomes:

$$< \Pi_{ij} >= (\frac{1}{2}\frac{< p_1^2 >}{\rho_0 c_0^2} - \frac{1}{2}\rho_0 < \vec{v}_1^2 >)\delta_{ij} + < \rho_0 v_{1i} v_{1j} > . \tag{2.13}$$

With the expression 2.13, the radiation pressure can be calculated directly from the pressure and velocity fields at the first order, the non-linearities of the medium do not intervene. From now on, I will drop the index 1 since all acoustic fields appear at first order only. While the

computation of the Brillouin tensor requires the expression of the acoustic fields at first order in the fluid only, it remains to compute the total field in the fluid that is the sum of the incident and scattered fields.

2.1.3 Radiation pressure on an elastic sphere in an ideal fluid

In the presence of the sphere, the total acoustic pressure field is composed of the incident pressure field p_i and the scattered pressure field p_s:

$$p = p_i + p_s. \tag{2.14}$$

From this stage, a spherical target is assumed, and in these conditions, a spherical coordinates system is the best choice to write the boundary conditions at the object surface that couple incident and scattered field.

We decompose in spherical coordinates, (r, θ, φ):

$$\begin{cases} x = r\sin\theta\cos\varphi, \\ y = r\sin\theta\sin\varphi, \\ z = r\cos\theta. \end{cases} \tag{2.15}$$

With a set of orthogonal functions called spherical harmonics which are defined by:

$$\begin{aligned} Y_n^m(\theta,\varphi) &= \sqrt{\frac{(2n+1)}{4\pi}\frac{(n-m)!}{(n+m)!}}P_n^m(\cos\theta)e^{im\varphi} \\ &= N_n^m P_n^m(\cos\theta)e^{im\varphi}. \end{aligned} \tag{2.16}$$

Where $P_n^m(\cos(\theta))$ are the Legendre polynomials. The azimuthal number m and the radial degree n satisfy $|m| \leq n$. The time convention adopted is $exp(-i\omega t)$.

The point $r = 0$ belongs to the domain of definition of p_i, this yields the choice of the

spherical Bessel function, $j_n(kr)$ with $k = \omega/c_0$ is the wave number:

$$p_i(r,\theta,\varphi,t) = p_a \sum_{n=0}^{\infty} \sum_{|m|<n} A_n^m j_n(kr) Y_n^m(\theta,\varphi) \exp(-i\omega t), \tag{2.17}$$

where the A_n^m are called the beam shape coefficients (BSC) and must be computed.

Linear scattering

Since, from the one hand, only the linear scattering is involved in our problem and on the other hand, the spherical harmonics are orthogonal we can assume that the scattered pressure field can be written:

$$p_s(r,\theta,\varphi,t) = p_a \sum_{n=0}^{\infty} \sum_{|m|<n} R_n^m A_n^m h_n^{(1)}(kr) Y_n^m(\theta,\varphi) \exp(-i\omega t). \tag{2.18}$$

Where $h_n^{(1)}(kr)$ is the spherical Hankel function of the first kind describing the divergent wave scattered by the sphere.

Far field approximation

By applying the expressions Eq. (2.14, 2.17, 2.18) to Eq. (2.13), the components of Brillouin tensor in spherical coordinates can be obtained: $< \Pi_{rr} >$, $< \Pi_{r\theta} >$, $< \Pi_{r\varphi} >$. The derivation is given in [74, 45], and in the following, the steps used are mentioned.

The calculation of these components can be simplified by supposing that the radius R of the surface S is approaching infinity ($R \to \infty$). In practice, the spherical Hankel and Bessel functions take the following asymptotic form:

$$h_n^{(1)}(kR) \simeq (-i)^{(n+1)} \frac{e^{(ikR)}}{kR}, \tag{2.19}$$

and:

$$j_n(kR) = \frac{h_n^{(1)}(kR) + h_n^{*(1)}(kR)}{2}. \tag{2.20}$$

After replacing the spherical Hankel and Bessel functions by their asymptotic forms in Eq. (2.17, 2.18), and applying these expressions of pressure field to calculate $< \Pi_{rr} >$, $< \Pi_{r\theta} >$,

$< \Pi_{r\varphi} >$,the components proportional to $1/R^4$ are negligible since $R \to \infty$. We notice that only one component of the Brillouin tensor $< \Pi_{rr} >$ (proportional to $1/R^2$) intervenes which involves only the flow of radial momentum transported across the surface.

Radiation forces on an elastic sphere in an ideal fluid

Finally, the three components of radiation pressure exerted on an arbitrarily located elastic sphere in a perfect fluid by an arbitrarily incident beam are [74]:

$$F_x = -\frac{\langle V \rangle}{k_0^2} \sum_{n=0}^{\infty} \sum_{|m|<n} \Im(Q_n^{-m} A_n^{m*} A_{n+1}^{m-1} C_n + Q_n^m A_n^m A_{n+1}^{m+1*} C_n^*), \tag{2.21}$$

$$F_y = +\frac{\langle V \rangle}{k_0^2} \sum_{n=0}^{\infty} \sum_{|m|<n} \Re(Q_n^{-m} A_n^{m*} A_{n+1}^{m-1} C_n + Q_n^m A_n^m A_{n+1}^{m+1*} C_n^*), \tag{2.22}$$

$$F_z = -2\frac{\langle V \rangle}{k_0^2} \sum_{n=0}^{\infty} \sum_{|m|<n} \Im(G_n^m A_n^{m*} A_{n+1}^m C_n). \tag{2.23}$$

With :

$$V = p_a^2/(2\rho_0 c_0^2),$$
$$C_n = R_n^* + R_{n+1} + 2R_n^* R_{n+1},$$
$$Q_n^m = \sqrt{(n+m+1)(n+m+2)}/\sqrt{(2n+1)(2n+3)},$$
$$G_n^m = \sqrt{(n+m+1)(n-m+1)}/\sqrt{(2n+1)(2n+3)}.$$

From the theoretical expressions of the radiation pressure, two coefficients are required to determine the forces:

- Scattering coefficients: R_n
- Incident BSC: A_n^m

Here, the scattering coefficients R_n^m are simplified to R_n. The reason will be explained in the next section. The two next sections describe the procedure to compute these two sets of coefficients.

2.2 Scattering coefficient

The study of the scattering problem of a plane longitudinal wave in interaction with spheres begins by Anderson [85] (liquid sphere) and Faran [86] (elastic sphere). The general theory of acoustic diffraction processing for a sphere of any size in front of the wavelength is introduced. Then, Epstein and Carhart[87], as well as Allegra and Hawley[88] have integrated the thermal and viscous effects to these models. However, the above models are valid by supposing the acoustic field is axisymmetric. In the case of the scattering of a plane shear wave, the field is no longer axisymmetric. Truell and al.[89] have used for the first time the scalar potentials of Debye to solve this problem. For different forms of objects, the matrix called "T-matrix"[90, 91] is introduced by Waterman. Nevertheless, this matrix works only for spherical or cylindrical objects.

To break these limitations and get an expression adapted to acoustic tweezers, the study of [45] using the same decomposition as Truell developed the general expression of scattering coefficients of an elastic sphere in any kind of acoustic longitudinal waves. Thus the method of Anderson and Faran was generalized.

The problem is to calculate the scattering coefficients on an elastic sphere in any acoustic field. We select a spherical coordinates system (r, θ, φ) centered on the sphere (see Fig. 2.2). The acoustic waves propagate with speed c_0 in the fluid medium. The sphere is elastic, homogeneous and isotropic, with density ρ_p and radius a. Longitudinal and transverse waves propagate respectively with velocity c_l and c_t.

Potentials decomposition

As presented in the previous section, the acoustic pressure field in the fluid is the solution of the scalar Helmholtz equation and hence can be decomposed in a spherical harmonics function series (Eq. (2.17, 2.18)). In the following, we give a concise presentation of the steps required to do the same kind of decomposition for an elastic medium.

Debye Potentials

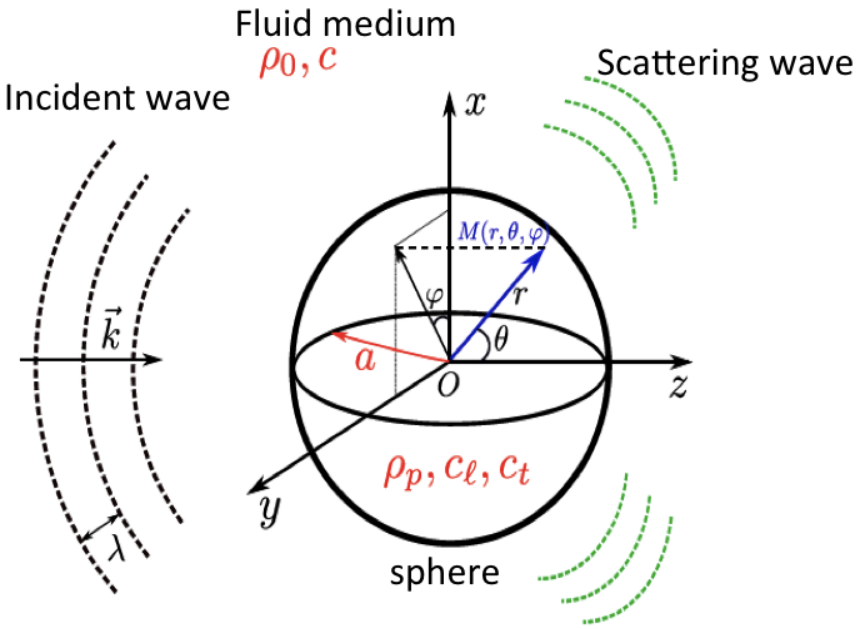

Figure 2.2: Spherical basis of the problem. Sphere of radius a suspended in a fluid of density ρ_0 and sound speed c_0. The sphere scatters the incident acoustic wave. The spherical basis is centered at the sphere center O. Transmitted waves are excited inside the particle of density ρ_p and velocities c_l and c_t for the longitudinal and transverse (or shear) components respectively [45].

The elastic equation of momentum conservation in linear regime is [92]:

$$-\rho_p \omega^2 \vec{u} = (\lambda_p + \mu_p)\vec{\nabla}(\vec{\nabla} \cdot \vec{u}) + \mu_p \vec{\Delta}\vec{u}. \tag{2.24}$$

where $\vec{u}$ is the field of displacement and λ_p and μ_p are the two Lamé parameters. Applying the decomposition of Helmholtz,

$$\vec{u} = \vec{\nabla}\Phi + \vec{\nabla} \wedge \vec{A}. \tag{2.25}$$

we can split this equationin an "irrotational" part and a "solenoidal" part.

$$\begin{aligned} k_l \Phi + \Delta\Phi &= 0, \\ k_t \vec{A} + \vec{\nabla} \wedge \vec{\nabla} \wedge \vec{A} &= 0. \end{aligned} \tag{2.26}$$

with $k_{l,t} = \omega / c_{l,t}$, $c_l = \sqrt{(\lambda_p + 2\mu_p)/\rho_0}$ and $c_t = \sqrt{\mu_p / \rho_0}$

After this step, we go from a vector $\vec{u}$ with three unknowns to a scalar potential and a vector potential with four unknowns in total. To eliminate the indeterminacy, the generic Gauge

condition $\vec{\bigtriangledown} \cdot \vec{A} = 0$ is generally used. However, for a spherical scatterer, the decomposition to use is the Debye coefficients. Indeed the vector potential $\vec{A}$ can be written as a function of two scalar potentials (ψ, χ) (Eq. (2.27)):

$$\vec{A} = \vec{\bigtriangledown} \wedge (r\vec{e_r}\psi) + \vec{\bigtriangledown} \wedge \vec{\bigtriangledown} \wedge (r\vec{e_r}\chi)/k_t. \tag{2.27}$$

Using this decomposition, the equation for the potential vector splits into two scalar Helmholtz equations and the whole problem can now be written:

$$\begin{aligned} \Delta\Phi + k_l^2\Phi &= 0, \\ \Delta\psi + k_t^2\psi &= 0, \\ \Delta\chi + k_t^2\chi &= 0. \end{aligned} \tag{2.28}$$

Therefore, the potentials (Φ, ψ, χ) can be decomposed in the basis of spherical harmonics:

$$\Phi = \frac{\phi_0}{\omega} \sum_{n=0}^{\infty} \sum_{m=-n}^{n} S_n^m A_n^m j_n(kr) Y_n^m(\theta, \varphi), \tag{2.29}$$

$$\psi = \frac{\phi_0}{\omega} \sum_{n=0}^{\infty} \sum_{m=-n}^{n} T_n^m A_n^m j_n(kr) Y_n^m(\theta, \varphi), \tag{2.30}$$

$$\chi = \frac{\phi_0}{\omega} \sum_{n=0}^{\infty} \sum_{m=-n}^{n} U_n^m A_n^m j_n(kr) Y_n^m(\theta, \varphi). \tag{2.31}$$

Four unknowns R_n^m, S_n^m, T_n^m and U_n^m have been introduced and can be determined by applying the boundary conditions on the surface of the sphere with radius a.

Boundary conditions

At the interface, by applying the continuity of normal displacements and the continuity of constraints:

$$\begin{aligned} u_i^f + u_s^f &= u_r, \\ p_i + p_s &= -\tau_{rr}, \\ 0 &= \tau_{r\theta}, \\ 0 &= \tau_{r\varphi}. \end{aligned} \tag{2.32}$$

where $u^f_{i,s}$ is the radial displacement of the fluid particles at the surface of the sphere for the incident and scattered waves. The medium here is fluid and devoid of viscosity which explains the zero tensor of the last two equations of Eq.(2.32). The elements of the Cauchy stress tensor, τ_{ij}, are connected to the components of the displacement vector u_i by Hook's law:

$$\tau_{ij} = \lambda_p \epsilon_{kk} \delta_{ij} + 2\mu_p . \epsilon_{ij} \tag{2.33}$$

Where $\epsilon_{ij} = 0.5(\frac{\partial u_i}{\partial x_j} + \frac{\partial u_j}{\partial x_i})$ is the tensor of the linearized strains and ϵ_{kk} its trace, δ_{ij} is the Kronecker delta. At this point, one could include viscous losses in the sphere considering complex Lamé coefficients.

To write the first boundary conditions, we need a relation between the displacement in the fluid and our potential, i.e the pressure. With the linearized Euler equation in steady regime and $\vec{v} = \frac{\partial \vec{u}}{\partial t}$:

$$\rho_0 \omega^2 \vec{u} = \vec{\bigtriangledown} p. \tag{2.34}$$

Similarly, in the solid, it is necessary to express the displacement $\vec{u}$ and the components of the stress tensor τ_{ij} as a function of the potentials (Φ, ψ, χ) that we have introduced. After the displacement $\vec{u}$ and stress tensor τ_{ij} are expressed in spherical harmonics, the boundary conditions are applied. To get rid of θ, φ dependence, integration on the surface of the sphere is performed and the orthogonal properties of associated Legendre polynomials [93, 94] are used:

$$< P^m_k | P^m_l >= \frac{2(l+m)!}{(2l+1)(l-m)!} \delta_{k,l}. \tag{2.35}$$

With the scalar product defined as:

$$< P^m_n | P^{m'}_{n'} >= \int_0^\pi P^m_n(\cos\theta) P^{m'}_{n'}(\cos\theta) \sin\theta d\theta = \int_{-1}^1 P^m_n(x) P^{m'}_{n'}(x) dx. \tag{2.36}$$

The linear system of 4 equations with four unknown splits in two independent systems of three and one equation respectively. The first one describes an incident longitudinal wave that is coupled to the longitudinal wave and one shear wave in the solid. The second one describes the second shear wave that can not be excited. This property is ascribed to the Debye decomposition. As a consequence, when the incident wave is longitudinal the m dependence can be dropped $R^m_n = R_n$ and the first system of 3 equations is equal to the one derived by

Faran for an incident longitudinal plane wave.

The scattering coefficients expressions are obtained:

$$R_n = -\frac{j_n(ka)\epsilon_n - kaj'_n(ka)}{h_n(ka)\epsilon_n - krh'_n(ka)}, \tag{2.37}$$

ϵ_n is a coefficient which depends only on the properties of the elastic material and is written:

$$\epsilon_n = \frac{1}{2}\frac{\rho_0}{\rho_p}(k_t a)^2 \frac{a_n/b_n - c_n/d_n}{e_n/b_n - f_n/d_n}, \tag{2.38}$$

with:

$$\begin{aligned}
a_n &= k_l a j'_n(k_l a),\\
b_n &= k_l a j'_n(k_l a) - j_n(k_l a),\\
c_n &= 2n(n+1)j_n(k_t a),\\
d_n &= -2k_t a j'_n(k_t a) - ((k_t a)^2 - 2n(n+1) + 2)j_n(k_t a),\\
e_n &= 2k_l a j'_n(k_l a) + (\frac{(k_t a)^2}{2} - n(n+1))j_n(k_l a),\\
f_n &= 2n(n+1)(j_n(k_t a) - k_t a j'_n(k_t a)).
\end{aligned} \tag{2.39}$$

The scattering coefficient R_n therefore depends only on the mechanical parameters of the sphere (ρ_p, c_l, c_t), its radius, (a), the excitation angular frequency, ω, and the incident medium properties ρ_0, c_0. The results correspond identically to those obtained conventionally by Faran [86] in the case of an incident longitudinal plane wave.

2.3 Incident beam shape coefficients

As already mentioned, the incident field can be expressed in terms of spherical harmonics (Eq. (2.17)). Then, the spatial part of the field depends on the BSC A_n^m:

$$p_i(r,\theta,\varphi) = p_a \sum_{n=0}^{\infty} \sum_{|m|<n} A_n^m j_n(kr) Y_n^m(\theta,\varphi). \tag{2.40}$$

These coefficients are mandatory for the determination of the radiation pressure. For a given position of the sphere, with a spherical coordinates system centered on the sphere, coefficients A_n^m can be obtained analytically for different fields like plane wave, Bessel beam or focused vortex beam. The expressions of the incident BSC for these three fields are given in the

following paragraphs.

Beam shape coefficients for a plane wave

A plane wave propagating along the $z-$axis has the following expression in a Cartesian coordinates system:

$$p_i(\vec{x}, t) = p_a e^{i(kz-\omega t)}, \tag{2.41}$$

and in spherical coordinates (see the convention provided in Eq. (2.15)):

$$p_i(\vec{x}, t) = p_a e^{i(kr\cos\theta-\omega t)}. \tag{2.42}$$

The decomposition of the spatial dependency into the basis of spherical harmonics (defined Eq. (2.17)) is:

$$e^{ikr\cos\theta} = \sum_{n=0}^{\infty} c_n N_n P_n(\cos\theta). \tag{2.43}$$

Here, the symmetries of the plane wave implies that there is no azimuthal dependency and thus no summation on the index m. The coefficients N_n corresponds to the coefficients N_n^0 defined Eq. (2.16) and the coefficients c_n have to be determined.

By using the orthogonality of the associated Legendre polynomials, one obtains:

$$c_n = \frac{1}{N_n}\frac{2n+1}{2}\int_0^{\pi} e^{(ikr\cos\theta)} P_n(\cos\theta)\sin\theta d\theta. \tag{2.44}$$

Knowing that the integral form of the spherical Bessel function is:

$$j_n(kr) = \frac{1}{2i^n}\int_0^{\pi} e^{(ikr\cos\theta)} P_n(\cos\theta)\sin\theta d\theta, \tag{2.45}$$

the Eq. (2.43) then becomes:

$$e^{ikr\cos\theta} = \sum_{n=0}^{\infty} \frac{i^n(2n+1)}{N_n} j_n(kr) P_n(\cos\theta). \tag{2.46}$$

Finally, the incident BSC of a plane wave propagating along the $z-$axis are:

$$A_n^m = \begin{cases} i^n\sqrt{4\pi(2n+1)} & \text{if } m = 0, \\ 0 \text{ if} \qquad m \neq 0. \end{cases} \tag{2.47}$$

Beam shape coefficients for a Bessel beam

A Bessel beam is a superposition of plane wave with wave vectors distributed over a cone of aperture angle β. Note that a cylindrical wave of charge m' can be expressed in the spherical coordinate with the following form[95]:

$$\Phi = \Phi_0 \sum_{n=|m'|}^{\infty} i^{(n-m')}\frac{(n-m')!}{(n+m')!}(2n+1)j_n(kr)e^{im'\varphi}P_n^{m'}(\cos\theta)P_n^{m'}(\cos\beta), \tag{2.48}$$

where m' is an fixed integer and the coefficient A_n^m:

$$A_n^m = 4\pi i^{(n-m')}Y_{n'}^{m'}(m', n, \varphi = 0, \theta = \beta). \tag{2.49}$$

Focused cylindrical vortex beam

This beam is very important because, it is the keystone to create acoustic tweezers [42, 45, 46, 96]. The BSC for a focused vortex beam are[42]:

$$A_n^m = \delta_{m,m'}4\pi N_n^{m'}(kr_0)^2 h_n^{(1)}(kr_0)\int_{\pi-\alpha_0}^{\pi} P_n^{m'}(\cos\theta')\sin\theta' d\theta'. \tag{2.50}$$

With $h_n^{(1)}$ the spherical Hankel function of the first kind, m' the topological charge of the vortex and α_0, a_0, r_0 are respectively the aperture angle, the radius of the transducer and the focal distance as illustrated on top of Fig. 2.3. Note that the expression of coefficients A_n^m is not exactly the same as in reference [42] because of the different definitions of spherical harmonics. In this paper, we use the expression of normalized spherical harmonics with a factor N_n^m, as shown in Eq. (2.16).

Using Eq. (2.50), the pressure field can be computed anywhere. Figure 2.3 shows the pressure field for a focused vortex beam of charge $m' = 1$ (top row), and the BSC (bottom). The pressure field has a zero amplitude along the axis of propagation. This is a common feature

associated with the vortex beam [97, 98]. This feature is important for acoustical tweezers since elastic bead smaller than the wavelength are trapped at pressure nodes, i.e a positive intensity gradient. The focusing is important because the aperture of the transducer is $5.5cm$, $7.5cm$ away from the focus (corresponding to an angle equal to $\alpha_0 = 43^o$). Note that the lateral energy density gradient is much larger than its axial counterpart and this results in a larger radial radiation force than the axial one. As expected, the BSC are restricted to the column $m = 1$ with a non-intuitive variation in function of the radial degree.

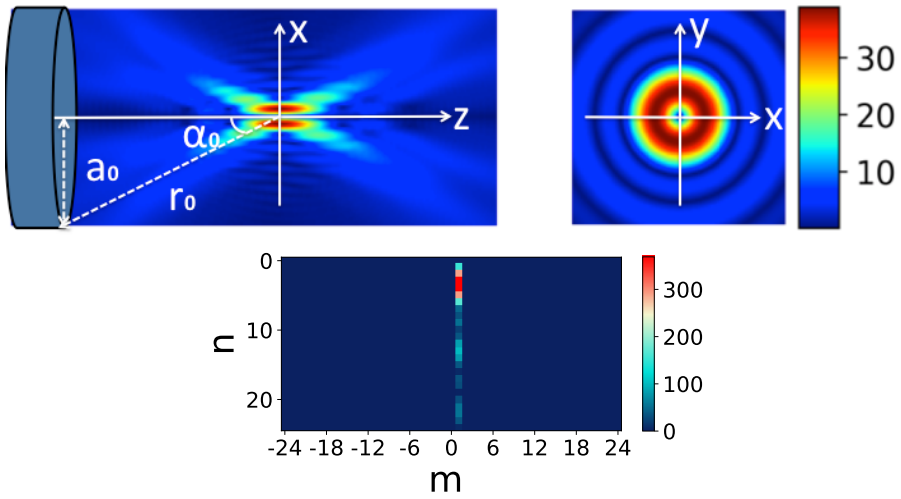

Figure 2.3: (Top) Modulus of the complex pressure field at frequency $f_0 = 1.2\,\mathrm{MHz}$ and (bottom) BSC, for a focused vortex with topological charge $m' = 1$ generated with a concave spherical transducer: aperture angle $\alpha_0 = 43^o$, radius of the transducer $a_0 = 5.5\,\mathrm{cm}$, geometrical focus $r_0 = 7.5\,\mathrm{cm}$, the spherical basis is centered at the focus of the incident beam.

Focused spherical vortex beam

Another design of the vortex beam is called the spherical vortex beam with the sound field identical to a sphere at the focal position. The coefficients are different from the focused cylindrical vortex beam. In the integral, Eq. (2.50), an associated Legendre polynomial normalized to unity is added $\tilde{P}_l^{m'}(\cos\theta') = P_l^{m'}(\cos\theta')/\max_{\theta'\in\{\pi-\alpha_0,\pi\}}\left(P_l^{m'}(\cos\theta')\right)$. This amplitude modulation of the source aperture discriminate focused acoustical vortices from spherical vortices. Comparing Figs. 2.3 and 2.4, one can notice that it changes the energy density around the focus radically and strongly increase the energy density axial gradient. The radial degree l is chosen so that the amplitude variates smoothly in the range of $\theta_0 = [\pi - \alpha_0 : \pi]$ (the source aperture) and gently drops near zero for $\theta_0 = \pi - \alpha_0$ to avoid strong secondly lobes in the

radiated field. To shorten expressions, the change of variable : $x = -\cos\theta'$ is used in the following. Integrands can be further simplified with the relation $P_l^{m'}(-x) = (-1)^{l+m'} P_l^{m'}(x)$.

$$A_n^m = \delta_{m,m'} 4\pi N_n^{m'} (kr_0)^2 h_n^{(1)}(kr_0)(-1)^{n+l} \int_{\cos\alpha_0}^{1} \tilde{P}_l^{m'}(x) P_n^{m'}(x) dx. \tag{2.51}$$

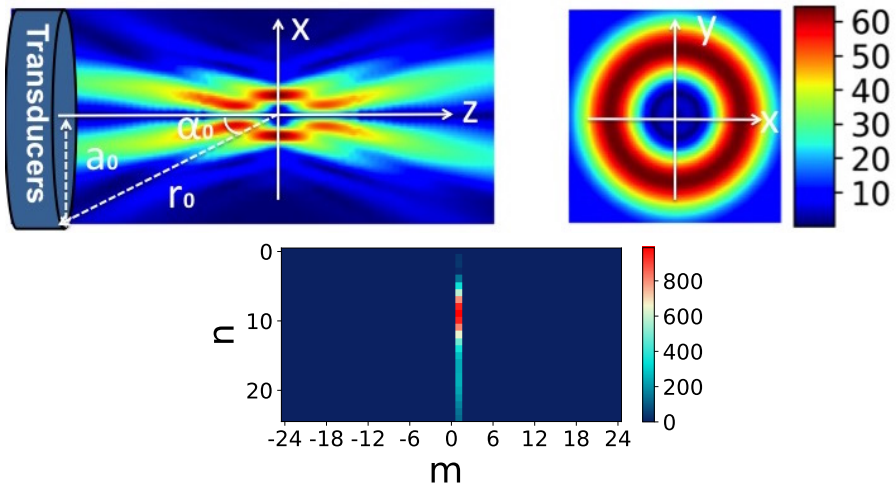

Figure 2.4: (Top) Modulus of the complex pressure field at frequency $f_0 = 1.2\,\text{MHz}$ and (bottom) BSC, for a focused spherical vortex with topological charge $m' = 1$, radial degree $l = 8$ generated with a concave spherical transducer: aperture angle $\alpha_0 = 43^o$, radius of the transducer $a_0 = 5.5\,\text{cm}$, geometrical focus $r_0 = 7.5\,\text{cm}$, the spherical basis is centered at the focus of the incident beam.

Beam shape	A_n^m
wave plane	$i^n\sqrt{4\pi(2n+1)}$
Bessel beam	$4\pi i^{(n-m')} Y_{n'}^{m'}(m', n, \varphi = 0, \theta = \beta)$
Focused cylindrical vortex beam	$\delta_{m,m'} 4\pi N_n^{m'} (kr_0)^2 h_n^{(1)}(kr_0)(-1)^{n+m'} \int_{\cos\alpha_0}^{1} P_n^{m'}(x) dx$
Focused spherical vortex beam	$\delta_{m,m'} 4\pi N_n^{m'} (kr_0)^2 h_n^{(1)}(kr_0)(-1)^{n+l} \int_{\cos\alpha_0}^{1} \tilde{P}_l^{m'}(x) P_n^{m'}(x) dx$

Table 2.1: Coefficients A_n^m for different beam shapes.

In addition to the analytical method, the quadrature method using the orthogonal property of the spherical harmonic functions permits to calculate the coefficients A_n^m at any position by knowing the incident acoustic pressure field p_i. Different methods of A_n^m determination by

quadratures based on Eq. (2.52) will be detailed and compared in chapter 3.

$$A_n^m = \frac{1}{p_0 j_n(kr)} \int_\Omega p_i Y_n^{m*} d\Omega, \tag{2.52}$$

where Ω is a spherical surface. To calculate the radiation pressure exerted on the sphere at numerous different positions, the determination of coefficients A_n^m by quadrature method can be very tedious and numerically expensive. Nevertheless, we can make use of the property of orthogonality of spherical harmonics to obtain operators of rotation and translation. First, the BSC for one location of the sphere are calculated either numerically or analytically. Second, the new set of coefficients corresponding to other locations of the sphere are computed by applying linear operator of translation and rotation of the spherical basis to the first set. As described below, this method is made of two rotations and one translation (Fig. 2.5). As presented

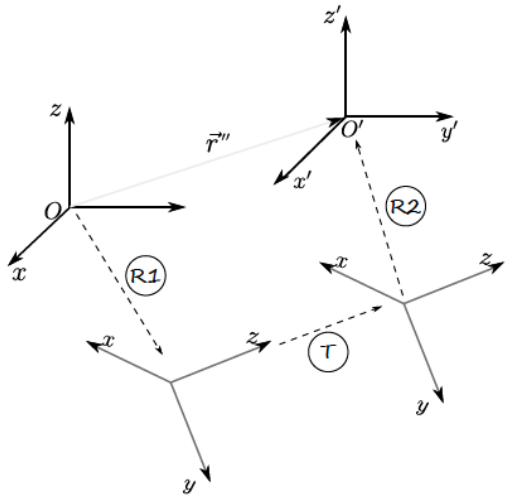

Figure 2.5: Arbitrary translation $\vec{r}$" decomposed into two rotations and one translation [45].

in Fig. 2.5, the first rotation $R1$ orients the axis Oz in the direction of the translation vector $\vec{r}$", then the translation operator T is applied in this direction, using the addition theorem to spherical harmonics. When the target arrives at the new position O, the second rotation $R2$ gives back their original direction to the basis vectors. Thus, the coefficients $\widetilde{A_n^m}$ at any new positions can be obtained by applying these rotations and translation to the initial A_n^m.

$$\widetilde{A_n^m} = \sum_{v=-n}^{n} D_n^{v,m}(R_2) \sum_{n'=0}^{\infty} C_{n',n}^m(kr") \sum_{m'=-n}^{n} D_n^{m',m}(R_1) A_n^m. \tag{2.53}$$

where the axial translation satisfies :

$$j_n(kr)Y_n^m(\theta,\phi) = \sum_{n'=0}^{\infty} C_{n',n}^m(kr")Y_{n'}^m(\theta',\phi'). \tag{2.54}$$

and for the rotation operator $D_n^{m,m'}$, the spherical harmonics satisfy the property :

$$Y_n^m(\theta,\phi) = \sum_{m'=-n}^{n} D_n^{m,m'}(R)Y_n^{m'}(\theta',\phi'). \tag{2.55}$$

with R the rotation matrix.

Overall, by applying translations and rotations to the coefficients A_n^m at a reference position, configurations at all other positions can be obtained easily.

2.4 Additional effects

Apart from the radiation pressure, some other additional forces can also arise in the single beam trapping system. As our experiments are underwater, acoustic streaming should be taken into consideration. Depending on the origin of the wave attenuation, acoustic streaming is usually divided into boundary streaming and bulk streaming.

Boundary streaming originates from the acoustic energy attenuation occurring in an acoustic viscous boundary of thickness $\sigma_v = \sqrt{2\mu/\rho\omega}$ (μ and ρ are the viscosity and density of the fluid, and ω is the driving angular frequency). It is often divided into inner streaming and outer streaming according to its position whether it's inside or outside the viscous boundary layer. Rayleigh [99] first analyzed and derived a solution of the outer streaming. Therefore the outer streaming is also called 'Rayleigh streaming'. The outer streaming is created from momentum diffusion of the velocity vorticity created near the boundary and not from pressure gradient effects [100]. Schlichting [101] first worked on the inner streaming and estimated the vortex size inside the boundary layer. The thermal dissipation is considered and analyzed [102]. When acoustic waves interact with axisymmetric objects, the viscous effect can induce a rotation of the objects. The viscous torque generated by orthogonal acoustic waves is first analytically calculated by [103]. In acoustic levitation, standing waves can also induce rotation of matter

in air [104] and is capable of rotating spherical particles and cells [105]. Besides, in acoustic vortex beams, the transfer of orbital angular momentum (OAM) to matter has been observed both in air [106, 107] and in water [52, 53]. In the paper [58], the torque of the particles as a result of absorption both in and around the sphere is measured and is at the range of pNm. The radiation pressure is significantly larger than the torque. Meanwhile, the thickness of the acoustic viscous boundary in our case is about 1 µm (with the frequency of ultrasound at 1 MHz in water at temperature 19^o) which is much smaller than the radii of target beads (from 0.1 mm to 0.7 mm) in our case. As a result, boundary streaming can be neglected.

Bulk streaming, also named 'Eckart streaming' [108], is caused by the absorption of the acoustic energy in the bulk of the fluid. Bulk streaming is typically observed in systems much larger than the wavelength. The wave damping is the source of the bulk streaming which is proportional to the square of the frequency. Thus, to generate Eckart streaming requires acoustic absorption over a long distance and it is more obvious in high frequency waves. In our studies, the acoustic beams are at about 1 MHz and are focused at a distance of 8 cm. Knowing that the acoustic attenuation length is about 20 m, the bulk streaming is not noteworthy to be considered.

As demonstrated in [58], the absorption within the sphere, as well as the viscous effect at the boundary, are responsible for the rotation. The viscous elasticity of the sphere material can influence the force exerted on the sphere by modifying the scattering coefficient. However, this effect is negligible compared to the radiation force.

Another effective influence is the generation of harmonics. The energy can be transferred to the harmonics and turn a sinusiodal wave into an acoustical shock wave [109]. This nonlinear effect is small and cumulative. It takes a certain distance to grow. The shock distance for an acoustic wave (with amplitude around 1 MPa, frequency of 1.2 MHz) is about 12 cm. This distance is comparable to the focal distance 8 cm. However, the field of interest in this study are sharply focused, the source aperture is large aperture is high. This results in a depth of field of about 4.6 mm much smaller that the shock distance. The array of transducers and the lens used in our experiment has an antenna gain about 30. Thus the signal amplitudes at the

transducers are much lower than 1 MPa. Therefore, the shock distance is far away from the focal position of the vortex beam. Thus, the generation of harmonics can also be neglected.

Chapter 3

Computation of the radiation force exerted by acoustic tweezers using pressure field measurements

3.1 Introduction

As presented in chapter 2, the radiation pressure exerted on an elastic sphere (Eqs. (2.21-2.23)) can be obtained by knowing the scattering coefficient R_n and the dubbed beam shape coefficients (BSC) A_n^m. Since the scattering coefficient R_n depends only on the physical characteristics of the object and propagation medium which can be computed with the Generalized Lorenz-Mie Theory, the estimation of the radiation pressure can be considered as a problem of calculating the BSC (A_n^m) from the measurement of the incident acoustic pressure field. Thus in this chapter, to obtain the BSC, three methods are investigated and compared: quadrature method, inverse problem regularization by sparsity and angular spectrum method (ASM). The first one consists of measuring the acoustic field on a spherical surface and calculating the spherical functions decomposition by quadratures. The second method is based on the measurement of the acoustic field at random points in a spherical volume and on the resolution of the inverse problem by a sparse method called the orthogonal matching pursuit (OMP). In the third method, the incident beam is measured on a transverse plane, decomposed into a sum of plane waves and then the expansion of coefficients is calculated. These methods are applied in numerical simulation of determining the BSC of a focused vortex beam of topological charge

$m' = 1$. This beam is very important because, it is the keystone to create acoustic tweezers [42, 45, 46, 96]. The theoretical expression of its BSC is presented in chapter 2. Then, experimentally a focused acoustic vortex beam and a focused Gaussian beam are synthesized and the methods of the BSC determination are applied to characterize the experimental radiation pressure. In the following sections, these methods will be demonstrated and compared.

3.2 Quadratures on spherical surface

The first method is based on the orthogonality of the spherical harmonics:

$$< Y_n^m, Y_{n'}^{m'} >= \delta_{n,n'}\delta_{m,m'},$$

where the scalar product on the sphere is defined by:

$$< f(\theta,\varphi), g(\theta,\varphi) >= \int\int f(\theta,\varphi)g(\theta,\varphi)\sin\theta d\theta d\varphi.$$

By applying this property to the incident acoustic field of Eq. (2.17), coefficients A_n^m can be expressed by integrals over a spherical surface:

$$\begin{aligned} A_n^m &= \frac{1}{p_a j_n(kr)} < p, Y_n^m > \\ &= \frac{1}{p_a j_n(kr)} \int_\theta \int_\varphi p(\theta,\varphi) Y_n^{m*}(\theta,\varphi)\sin\theta d\theta d\varphi. \end{aligned} \tag{3.1}$$

Using the quadrature method allows to approximate the integrals in Eq. (3.1) by a weighted sum over the points on a spherical surface. As expected the BSC for a focused vortex beam of topological charge $m' = 1$ are restricted to the column $m = 1$ with a non intuitive variation in function of the radial degree. We assessed numerically the relative error on the radiation force [Eqs. (2.21-2.23)] by decreasing the truncation order n. Thereafter, all series are truncated at $n \leq N = 25$ and the relative error on the force is 0.001. Different quadrature rules have been tested in the following parts: Lebedev quadrature, Legendre-Gauss quadrature, and Chebyshev quadrature [110].

3.2.1 Lebedev quadrature

In the Lebedev quadrature, the number, position and the weight of Lebedev grids defined on an unit sphere [(x_i, y_i, z_i) and weights w_i] have been derived by Sobolev [111]. Therefore,

measuring the pressure field at the Lebedev points (see Fig. 3.1 to visualize their positions) and using this quadrature give the BSC (A_n^m).

$$A_n^m = \frac{1}{j_n(kr)p_a} \sum_{i=0}^{I-1} p(\theta_i, \varphi_i) Y_n^{m*}(\theta_i, \varphi_i) w_i. \tag{3.2}$$

Lebedev quadrature has optimal efficiency, i.e. the number of points required, $I = (\mathcal{N}+1)^2/3$, is the smallest, where $\mathcal{N}$ is the highest order of the polynomials integrated on the sphere. Moreover, the distance between the Lebedev points is roughly constant. This feature is very interesting since it provides an optimal sampling of the sphere in regards with the finite size of an hydrophone, and thus it optimizes the signal-to-noise-ratio (SNR). The integrand is the product of spherical harmonics, Eqs. (2.17) and (3.1). If the series is truncated at $n \leq N$, the integrand is a polynomial of order smaller than $2N$ and hence $\mathcal{N} = 2N$. For our case, $N = 25$ and this yields $I = 867$. It must be noted that the number of Lebedev points is not arbitrary. Here, we use $I = 974$ Lebedev points on a sphere with radius 7 mm (5.6 λ). This choice allows the high order modes (here up until $n = 25$) to be perfectly retrieved. As shown in Fig. 3.1, the BSC are obtained by the Lebedev quadrature for a focused vortex beam.

This previous estimation does not take into account the noise in the measurements. It is known that the determination of the BSC are prone to errors in the presence of noise [112]. To assess the robustness of the method in presence of noise, we proceed in three steps. First, the theoretical BSC of Eq. (2.50), named thereafter $A_{n_{th}}^m$, are computed and the corresponding pressure field calculated with Eq. (2.17) on the Lebdev grid as well as in the focal plane to determine the maximum pressure. Second, a noise with a uniform distribution in an interval of amplitude 5% of this maximum pressure is added to the pressure field calculated on the Lebedev grid. Third, the BSC of this noisy pressure field, noted A_n^m, are estimated with Eq. (3.2) and shown on the bottom of Fig. 3.1.

In Fig. 3.1, the lines where the BSC are very different from the original ones 2.3 correspond to the values closest to zero for the Bessel function (Fig. 3.2). Indeed, since the scalar product with spherical harmonics is a linear operation, the result is the scalar product with the ideal pressure fields plus the scalar product with the noise. Hence the error is proportional to $1/j_n(kr)$. In Fig. 3.2, we can observe a first oscillating part up to $n = 35$ followed by a fast decrease converging to 0. We selected a sphere radius large enough, 7 mm(5.6 λ), so that the

truncation order $N = 25$ is located in the oscillating part. To assess the numerical performance of the method, we compute the relative error:

$$err = \frac{1}{(N+1)^2} \sum_{n=0}^{N} \sum_{m=-n}^{m=n} \frac{|A_n^m - A_{n_{th}}^m|}{\max(|A_{n_{th}}^m|)}. \tag{3.3}$$

Where $(N+1)^2$ is the total number of coefficient A_n^m of order $n \leq N$. Here the relative error is 0.061.

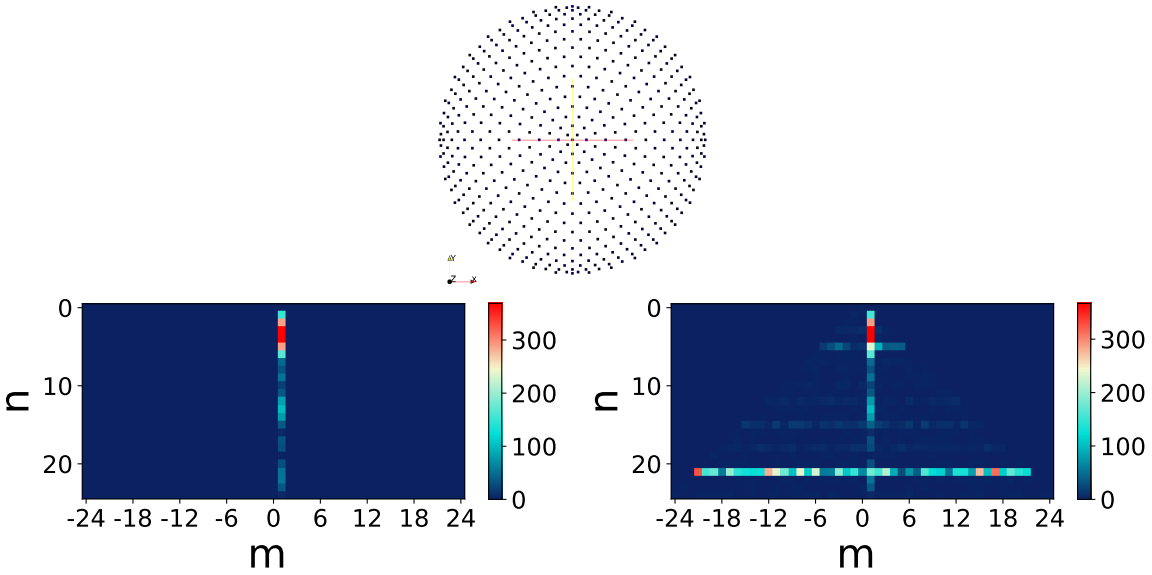

Figure 3.1: (Top) points on a Lebedev sphere, and (Bottom left) reconstructed beam shape coefficients for an incident focused vortex beam without noise and (Bottom right) with 5% noise.

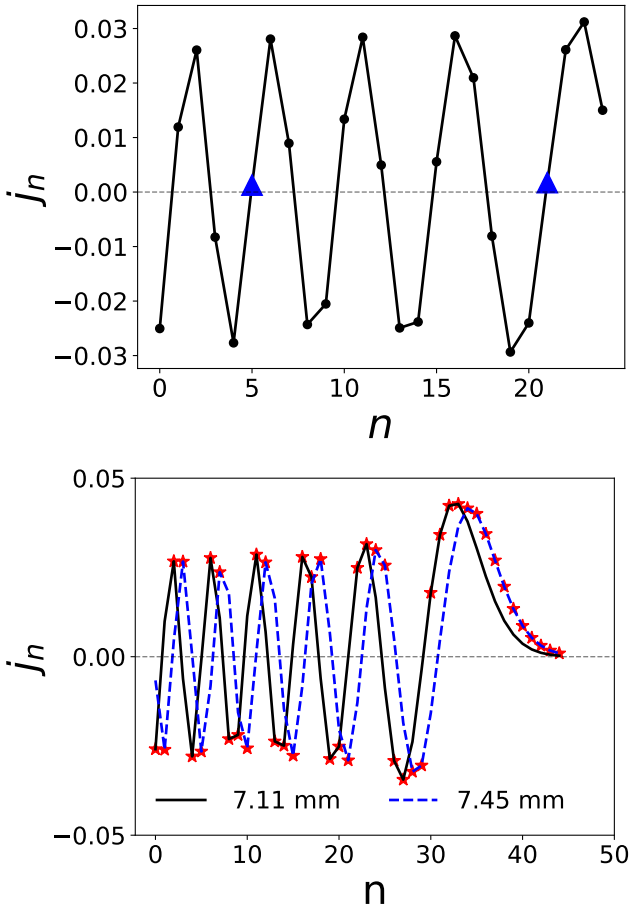

Figure 3.2: (Top) Amplitude of the spherical Bessel $j_n(kr)$ function for a radius r=7 mm (the blue triangles show the values close to zero) and (Bottom) for two different radii r_1=7.11 mm and r_2=7.45 mm (the red points show the maximum values between $|j_n(kr_1)|$ and $|j_n(kr_2)|$ for each order n). The frequency is f_0=1.2 MHz.

An upgrade in order to mitigate the detrimental effect of noise is to use a double layer Lebedev sphere [112]. The idea is to use two spheres with different radii and to apply the Lebedev quadrature, for a given ordrer n, to the sphere for which the Bessel function has the greatest absolute value. Using the asymptotic behavior of Bessel function for large x compared to n, $j_n(x) \approx \cos(x - \pi/2)/x$, in Fig. 3.2, we selected the radius of the second sphere such that $j_n(x') \approx \sin(x' - \pi/2)/x'$ to optimize the estimation, this leads to r_1=7.11 mm (5.7 λ) and r_2=7.45 mm (6λ). The red stars indicate the chosen value between the two Bessel functions to compute the beam shape coefficient of order n. Therefore, two spheres of different sizes are used. The double layer Lebedev sphere grids are presented in Fig. 3.3. For each sphere, 974 Lebedev points are used. Figure 3.3 shows the BSC obtained for an incident focused vortex beam with 5% of noise. They are close to the original ones 2.3. The double layer method

efficiently cancels the large errors introduced by the division of the Bessel functions and the relative error decreases from 0.06 to 0.015. Nevertheless, one can see that the BSC for $m \neq 1$ are not strictly equal to zero and thus a weak error remains on the estimated BSC.

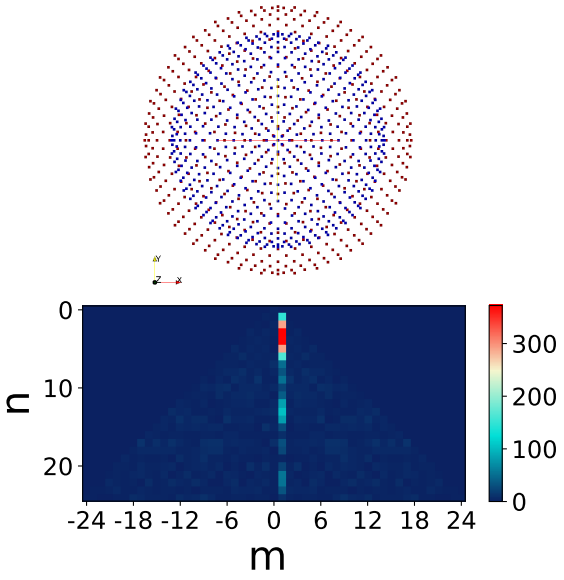

Figure 3.3: (Top) measurement points of a double layer Lebedev sphere, (Bottom) reconstructed beam shape coefficients for an incident focused vortex beam with 5% noise by the double layer Lebedev quadrature method.

3.2.2 Legendre-Gauss quadrature

The two-dimensional integrals in Eq. (3.1) can be considered as two one-dimensional integrals over θ and φ. Replacing the $Y_n^{m*}(\theta, \varphi)$ by Eq. (2.16), we obtain:

$$A_n^m = \frac{1}{p_a j_n(kr)} \int_\theta \int_\varphi p(\theta, \varphi) N_n^m P_n^m(\cos\theta) e^{-im\varphi} \sin\theta d\theta d\varphi, \tag{3.4}$$

With:

$$F^m(\theta) = \frac{1}{2\pi} \int_{\varphi=0}^{2\pi} p(\theta, \varphi) e^{-im\varphi} d\varphi, \tag{3.5}$$

which is a Fourier series decomposition, and can be approached by:

$$F^m(\theta) = \frac{1}{2K} \sum_{k=0}^{2K-1} p(\theta, \varphi_k) e^{-im\varphi_k}. \tag{3.6}$$

Where K is the number of points on φ. Then the Eq. (3.4) can be simplified by:

$$A_n^m = \frac{2\pi}{p_a j_n(kr)} N_n^m \int_{\theta=0}^{\pi} F^m(\theta) P_n^{m*}(\cos\theta)\sin\theta d\theta, \tag{3.7}$$

If we replace $\cos\theta$ by x, we obtain the following expression:

$$A_n^m = \frac{2\pi}{p_a j_n(kr)} N_n^m \int_{-1}^{1} F^m(\theta) P_n^{m*}(x) dx. \tag{3.8}$$

The Legendre-Gauss quadrature is a method to approximate a one-dimensional integral in the interval $[-1, 1]$:

$$\int_{-1}^{1} f(x)dx = \sum_{i=0}^{I_g-1} f(x_i) w_i. \tag{3.9}$$

Where x_i is the Gauss point position (I_g: the number of points on θ) and w_i the weight given by $w_i = \frac{2}{(1-x_i^2)[P_n'(x_i)]^2}$. With Eq. (3.9), the coefficients A_n^m can finally be calculated by:

$$A_n^m = \frac{1}{p_a j_n(kr)} \frac{\pi}{K} \sum_{i=0}^{I_g-1} \sum_{k=0}^{2K-1} p(\theta_i, \varphi_k) Y_n^{m*}(\theta_i, \varphi_k) w_i. \tag{3.10}$$

The points θ_i of the Gauss-Legendre quadrature are calculated by: $\theta_i = \arccos(x_i)$, and φ_k are distributed evenly between 0 and 2π.

We adopt here a grid of 30 points on θ and 60 points on φ (1800 points on total, comparable to the Lebedev grids), as shown on the top of Fig. 3.4. The sphere has a same radius with Lebedev quadrature [7.11 mm (5.7λ)]. With the same procedure of calculation as presented in the Lebedev quadrature, the BSC estimated with Eq. (3.10) are shown on the bottom of Fig. 3.4. The BSC obtained without noise in the incident beam are depicted on the left of Fig. 3.4. The BSC on column $m = 1$ are well retrieved, however, some noise appears on other columns where the BSC are supposed to be zeros. On the right side of Fig. 3.4 shows the BSC estimated when a 5% noise is added to the incident pressure field. The noise in the BSC augments with a relative error of 0.025 which is higher than the Lebedev method.

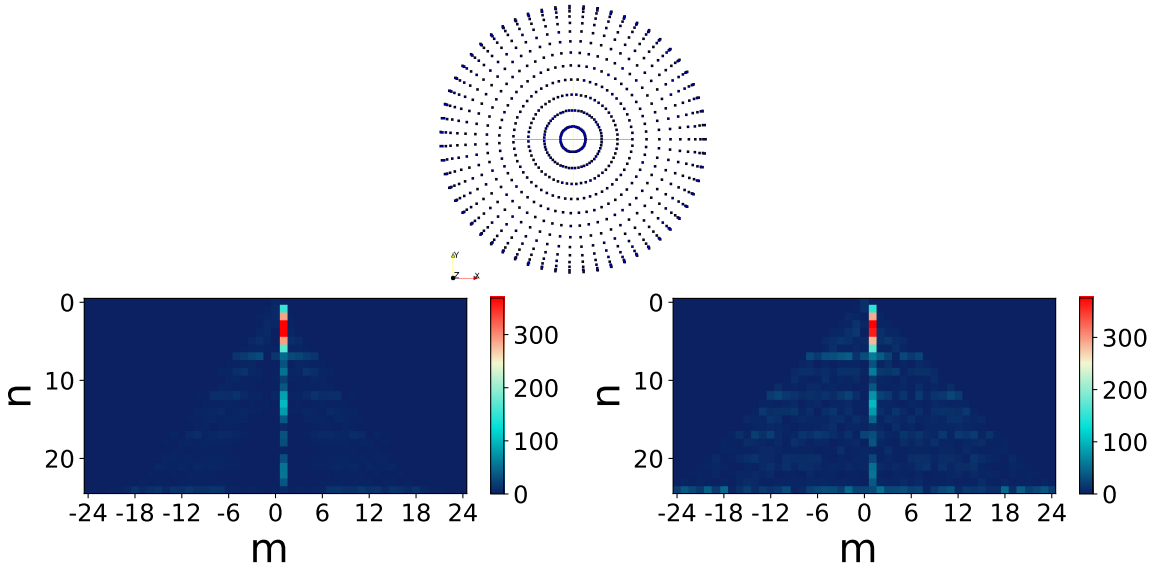

Figure 3.4: (Top) points on a Gauss-Legendre sphere, and (Bottom left) reconstructed BSC for an incident focused vortex beam without noise and (Bottom right) with 5% noise.

3.2.3 Chebyshev quadrature

For the Chebyshev quadrature, all the weights associated with nodes on the sphere are equal with $w_i = \frac{4\pi}{I}$ (I is the total number of nodes). And the coefficients can be expressed by:

$$A_n^m = \frac{4\pi}{j_n(kr)p_a I} \sum_{i=0}^{I-1} p(\theta_i, \varphi_i) Y_n^{m*}(\theta_i, \varphi_i). \tag{3.11}$$

Since the weights are identical to all the nodes, it is important to choose an optimal distribution of the points. We have assessed the efficiency of three kinds of distributions: the first is 30×60 points distributed regularly on θ and on φ respectively; the second is 1800 points distributed arbitrarily on the sphere; the last is a uniform distribution named t-design [113]. The radius of the sphere remains always the same. For the first and second distributions, we use the same number of points as the Gauss-Legendre quadrature (1800 points), however the t-design points can't be a random number. Here we adopt a grid of 1801 points. The distributions are depicted in Fig. 3.5 and the BSC are shown in Fig. 3.6.

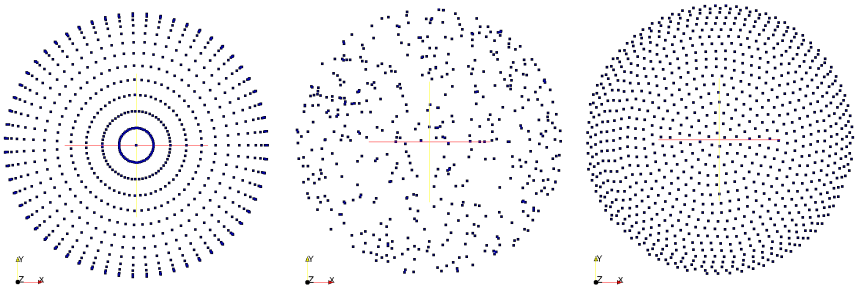

(a) Regular distribution (b) Random distribution (c) T-design

Figure 3.5: (Lef) Regular distribution, (Middle) random distribution, and (Right) t-design grids.

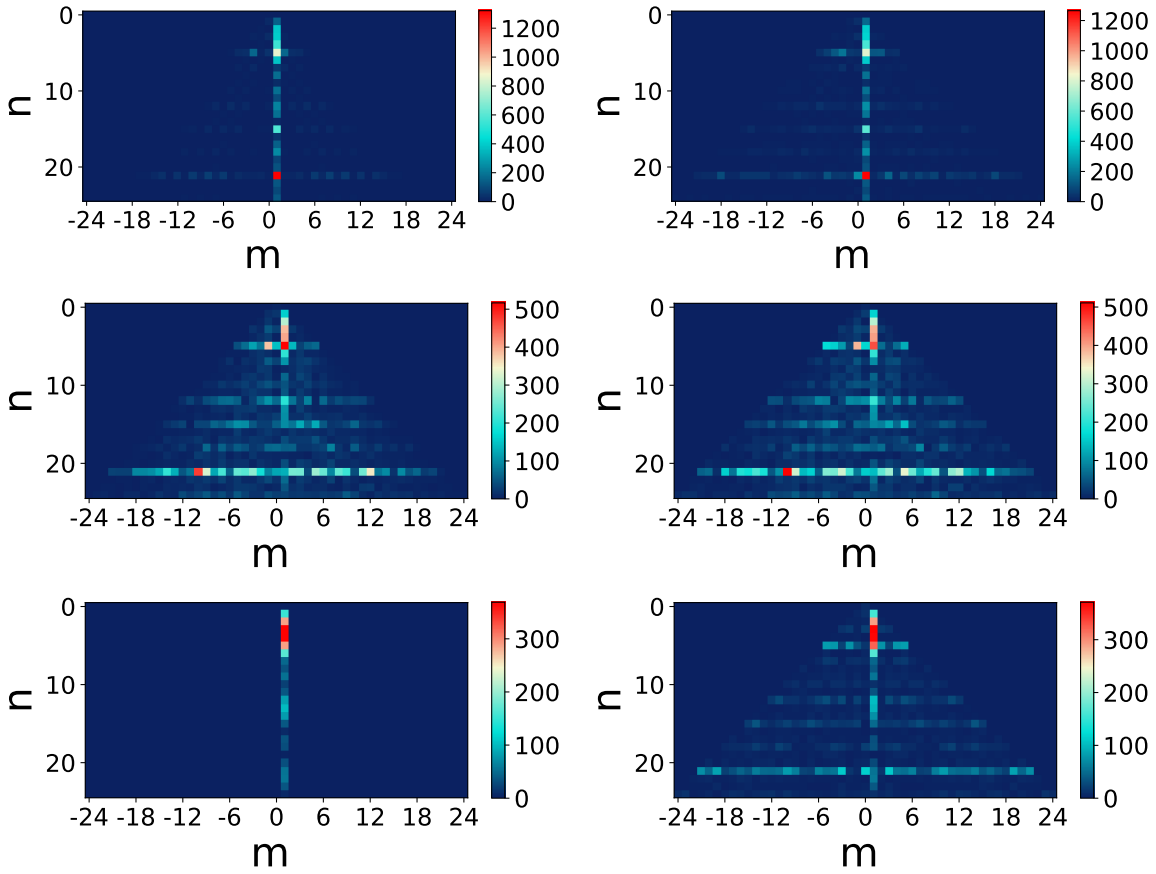

Figure 3.6: (Top) BSC on a regular sphere, and (Middle) BSC on a random sphere, and (Bottom) BSC on a t-design sphere (Left) without noise and (Right) with 5% noise in the incident beam.

Among all the grids tested with the Chebyshev quadratures, only the t-design points permit to find the exact BSC in the case without noise. In the case with 5% noise, the relative error of A_n^m obtained by t-design is 0.0323. Furthermore, we have increased the number of nodes to

1986. However, the relative error (0.029) does not decrease significantly and is always larger than the double layer Lebedev quadrature. Therefore, comparing the relative errors obtained by each quadrature method, the double layer Lebedev is the optimal method.

3.3 Regularization of the inverse problem by a sparse method

3.3.1 The OMP method

Instead of solving Eq. (3.1) with its discretized version Eq. (3.2), another strategy consists of solving Eq. (2.17) whose discretized counterpart can be reformulated under a matrix/vector form:

$$\underline{P} = \underline{\underline{M}}\,\underline{A} + \underline{\epsilon}, \tag{3.12}$$

with vector $\underline{P}$ whose components are the Fourier transform of the pressure field at frequency f_0 at point of discretization (x_i, y_i, z_i): $\hat{p}(x_i, y_i, z_i, f_0)$ of length I, vector $\underline{A}$ whose components are the BSC $A_l = A_n^m$ with $l = n(n+1)+m$ of length $L = (N+1)^2$, the matrix $\underline{\underline{M}}$ whose elements are $(j_n(kr_i)Y_n^m(\theta_i, \varphi_i))$ with $(r_i, \theta_i, \varphi_i)$ the points (x_i, y_i, z_i) written in spherical coordinates of size $(I \times L)$, and vector $\underline{\epsilon}$ the additive noise on points (x_i, y_i, z_i). Because of the noise, the direct inversion is not possible and a regularization has to be used. As can be seen on Fig. 2.3 for a focused vortex beam, a large number of beam shape coefficients are null. So, vector $\underline{A}$ is sparse. This *a priori* can be used to regularize the inversion:

$$\underline{\tilde{A}} = argmin||\underline{A}||_0 \ such\ as\ \underline{P} = \underline{\underline{M}}\ \underline{A}. \tag{3.13}$$

With this formulation, vector $\underline{\tilde{A}}$ is searched with a particular constraint: it must contain a minimum of non-zero terms. In practice, to find $\underline{A}$ we have to measure (or simulate) $\underline{P}$ on a set of points and to build matrix $\underline{\underline{M}}$ on the set of chosen points with a maximal number of modes for the truncature. To solve Eq. (3.13), we choose to use Orthogonal Matching Pursuit algorithm (OMP) [114]. This algorithm is iterative. For each iteration, the component of $\underline{\underline{M}}$ with the highest inner product with the remaining part of vector $\underline{P}$ is selected. Then its contribution is subtracted and the iterations continue on the residue. This procedure stops when the iteration

reaches the number of non-zero elements of the coefficients (25 in our case) or when the residual reaches a limit.

As previously, the truncature order is set to 25. At this stage the distribution of the points is free, the BSC can be calculated on any type of grids. A regular distribution of 45×45 points in a transverse plan (x, y) at the focal position $z = 0$ of size $7\,\text{mm} \times 7\,\text{mm}$ ($5.6\lambda \times 5.6\lambda$) is firstly used. In the case without noise, the BSC in column $m = 1$ obtained by OMP are depicted in Fig. 3.7. As shown in the figure, the BSC obtained by OMP are nulls for all the degree with odd numbers. However, for the even numbers, the results agree well with the theoretical values. In fact, the zero values are due to the associated Legendre polynomials $P_n^m(\cos\theta)$. In Fig. 3.7, the $P_n^m(\cos\theta)$ with $m = 1$ are plotted in plan (x, y) with $z = 0$ ($\theta = \pi/2$). As shown in the figure, $P_n^m(\cos\theta)$ equals zero for degree n with odd numbers. Thus, the plane (x, y) at $z = 0$ permits only to retrieve half of the BSC we need. To avoid the zeros, we take another plane (x, y) of same size at $z = 1\,\text{cm}$ (8λ). In this plane, θ is no longer at $\pi/2$. The BSC at column $m = 1$ obtained without noise, as shown in Fig. 3.8, superimpose with the theoretical values. However, by adding 5% of noise in the incident field, huge noise appear in the BSC (see Fig. 3.9). Accordingly, this distribution is very sensitive to noise.

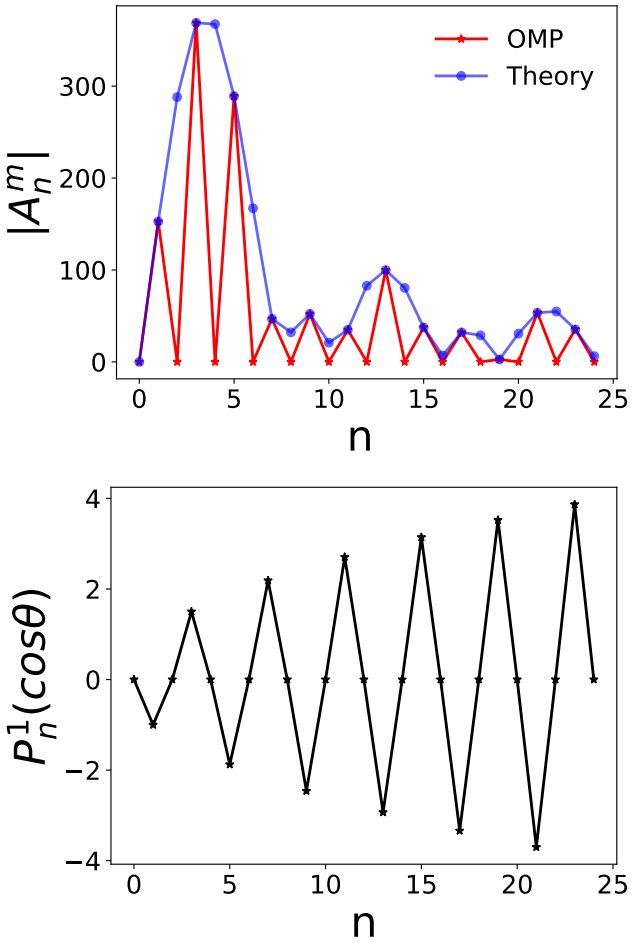

Figure 3.7: (Top) Modulus of BSC in column $m = 1$ of a focused acoustic vortex, and (Bottom) associated Legendre polynomials $P_n^m(\cos\theta)$ with $m = 1$ and $\theta = \pi/2$.

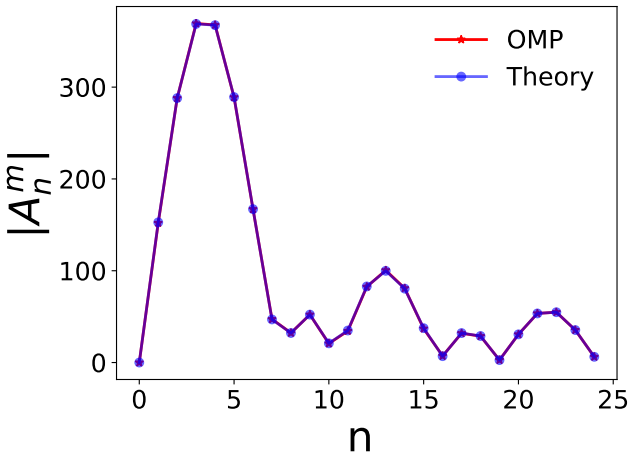

Figure 3.8: Modulus of BSC in column $m = 1$ of a focused acoustic vortex calculated in a plane at z =1 cm without noise.

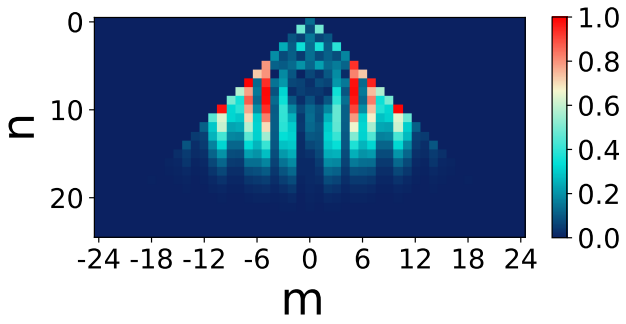

Figure 3.9: Modulus of BSC of a focused acoustic vortex calculated in a plane at z =1 cm with 5% noise in the incident wavefield.

To avoid an ill-conditioned matrix, the best choice is a set of random points distributed in a spherical volume as illustrated on Fig. 3.10. Because of the noise, the matrix $\underline{\underline{M}}$ is always full rank, the direct inversion is then always possible but unstable in regard of a small change in the noise. This ill-posed problem required regularization to get a meaningful solution. To compare this method with the double layer Lebedev sphere quadrature, we set the same number of points: 1948 dispersed in a spherical volume of identical radius $r = 7.11mm(5.7\lambda)$.

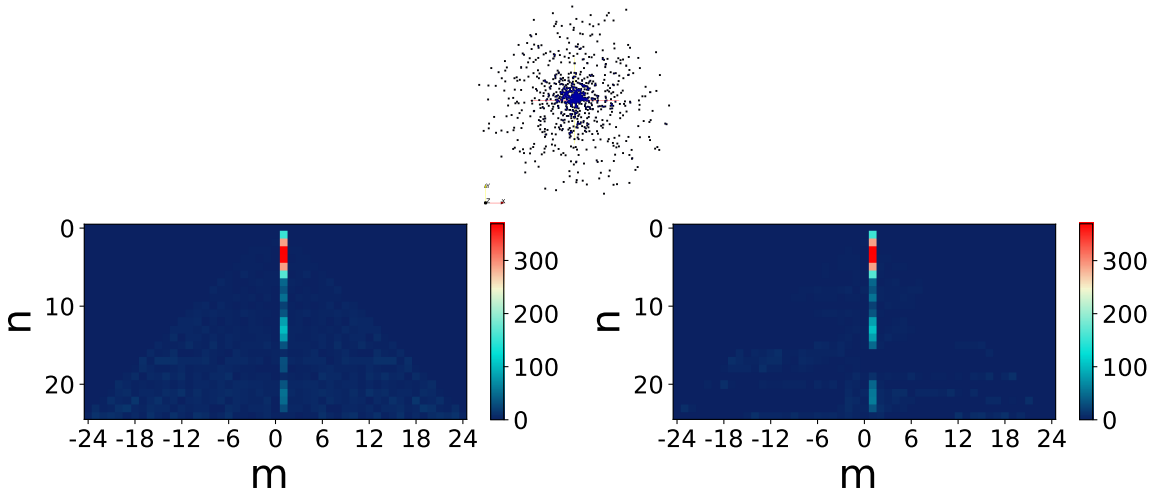

Figure 3.10: (Top) randomly distributed measurement points in a sphere, and (Bottom left) reconstructed beam shape coefficients for an incident focused vortex beam with 5% noise obtained by the OMP method and (Bottom right) block-OMP method.

With the OMP method, we should be able to recover the coefficients in column $m = 1$ with 25 iterations. However, tests for a vortex beam have shown the inefficiency of this stopping criterion. Thus, the stopping criterion of the OMP procedure will be the residual limit (lower than $1e-3$). Figure. 3.10 shows the BSC obtained with the OMP algorithm for the same

noisy field as before. There is a very good agreement with the original set of coefficients even if some coefficients are not exactly set to zero. Here, the relative error is 0.0141 close to the 0.015 obtained with le double layer Lebedev quadrature. A drawback is the number of iteration required, the computation can be very long.

3.3.2 The Block-OMP

A method to improve this is the Block version of OMP. It's the same procedure but with the matrix $\underline{\underline{M}}$ in a block version [115]. The algorithm is the same but the measurement matrix M and the coefficient A_l of size $N \times 1$ are divided in to blocks. This method helps us to take less iteration but obtain the same results as the OMP method.

$$\begin{aligned} \underline{A} &= [\underbrace{a_1 ... a_d}_{A[1]} \ \underbrace{a_{d+1} ... a_{2d}}_{A[2]} ... \underbrace{a_{N-d+1} ... a_N}_{A[n]}] \\ \underline{\underline{M}} &= [\underbrace{m_1 ... m_d}_{m[1]} \ \underbrace{m_{d+1} ... m_{2d}}_{m[2]} ... \underbrace{m_{N-d+1} ... m_N}_{m[n]}] \end{aligned} \tag{3.14}$$

Fig. 3.10 shows the coefficients obtained by applying the Block-OMP method, the matrix $\underline{\underline{M}}$ is divided into blocks of $(N \times 10)$, and the iteration number is 35 only. An unexpected outcome of using Block-OMP was that the relative error was halved: 0.006.

3.4 Angular spectrum method (ASM)

A third approach is to use a transformation from angular spectrum to spherical harmonics [116]. The Fourier transform of the pressure in plane z can be seen as a superposition of plane waves:

$$\begin{aligned} &\hat{p}(x, y, z, \omega) = \\ &\frac{1}{4\pi^2} \int\int_{k_x^2 + k_y^2 \leq k^2} S(k_x, k_y) e^{ik_x x + ik_y y + i\sqrt{k^2 - k_x^2 - k_y^2} z} dk_x dk_y, \end{aligned} \tag{3.15}$$

where the angular spectrum $S(k_x, k_y)$ is the two-dimensional spatial Fourier transform of the pressure in plane $z = 0$:

$$S(k_x, k_y) = \int_{-\infty}^{+\infty} \int_{-\infty}^{+\infty} \hat{p}(x, y, z = 0, \omega) e^{-i(k_x x + k_y y)} dx dy. \tag{3.16}$$

According to [116], the pressure field can be rewritten:

$$\begin{aligned}\hat{p}(x,y,z,\omega) =& \frac{1}{\pi}\sum_{n=0}^{\infty} i^n j_n(kr) \sum_{m=-n}^{n} Y_{nm}(\theta,\varphi) \\ &\times \int\int_{k_x^2+k_y^2\leq k^2} S(k_x,k_y) Y_{nm}^*(\theta_k,\varphi_k) dk_x dk_y,\end{aligned} \tag{3.17}$$

with:

$$k_x = k\sin(\theta_k)\cos(\varphi_k),\ k_y = k\sin(\theta_k)\sin(\varphi_k) \text{ and } k_z = k\cos(\theta_k).$$

Therefore, the comparison of Eq. (2.17) and Eq. (3.17) shows that the coefficients A_n^m can be written as:

$$A_n^m = \frac{i^n}{\pi}\int\int_{k_x^2+k_y^2\leq k^2} S(k_x,k_y) Y_{nm}^*(\theta_k,\varphi_k) dk_x dk_y. \tag{3.18}$$

The noisy pressure field is simulated here on a square grid of dimension 7 mm × 7 mm ($5.6\lambda \times 5.6\lambda$) regularly sampled with a total of 2500 points. Note that the mesh grids of ASM should be very fine, otherwise errors of integration in Eq. (3.18) arise. The square grid is located at the focal distance $(x, y, z = 0)$. This field is Fourier transformed [Eq. (3.16)] with a discrete Fourier transform (DFT). The sampling after a DFT can be refined by zero-padding, for instance. We performed a polynomial interpolation instead. Indeed, knowing the polynomial coefficients, numerical integration of Eq. (3.18) can be achieved with a variable step method to increase accuracy. Figure 3.11 shows the BSC obtained with the ASM method. The agreement with the original BSC is quite good, especially for column $m = 1$. Nevertheless, other columns contain non null BSC with a relative important amplitude. And the relative error is 0.014.

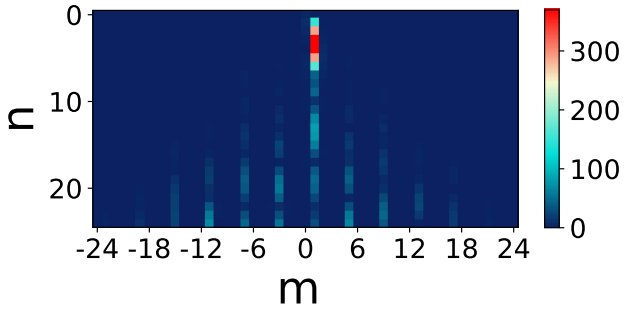

Figure 3.11: Computation of the BSC by angular spectrum decomposition.

Therefore, all methods listed in the Tab. 3.1 allow to retrieve the BSC for a focused vortex beam with a good confidence even in presence of noise.

Methods	Relative Error
Double layer Lebedev quadrature	0.015
OMP	0.014
Block - OMP	0.006
ASM	0.014

Table 3.1: Relative errors for three methods.

3.5 Estimation of the radiation pressure by the three methods

In the previous sections, three methods allow to retrieve the BSC are introduced: the double layer Lebedev quadrature (Lebedev), the block-OMP algorithm (OMP) and the angular spectrum (ASM). To assess the efficiency of each method, we calculate the radiation force exerted on a polystyrene sphere of radius $a = 0.1\lambda$. On the left of Fig. 3.12, the forces are calculated by using all the BSC obtained by the three methods, while on the right of Fig. 3.12, the forces are computed with A_n^1 only. From Fig. 3.12, it is clear that all methods yield accurate estimations of the radial force. On the contrary, the azimuthal force, F_ϕ, has a much weaker amplitude and all methods give poor estimates. Nevertheless, OMP method roughly recovers the original shape of the force. These differences originate from the estimated BSC with finite value outside column $m = 1$. It is shown in Fig. 3.12 that after filtering out these BSC, all methods recover the theoretical force perfectly. In the case of the axial force, F_z, both OMP and the ASM turn out to provide good estimations while again, the Lebedev method is less efficient and leads to fast oscillations around the expected curve. However, these errors can not be reduced by filtering the BSC outside $m = 1$. We may assume that the error is hidden in column $m = 1$.

The oscillations on the axial force calculated by Lebedev method are periodical, similar to those caused by a standing wave. Moreover, we know that the radiation pressure due to a standing wave is much stronger than the one due to a progressive wave [10]. Any error on the estimated BSC in this regard should lead to large discrepancies on the force estimation. In order to investigate this assumption, a weak amplitude wave propagating in the opposite direction is superposed to the incident wave. This can be achieved by adding the $0.005(-1)^{(n+m)}A_n^m$ to the initial BSC. Indeed, the symmetry $z \to -z$ transforms $\cos(\theta)$ into $\cos(\pi - \theta) = -\cos(\theta)$.

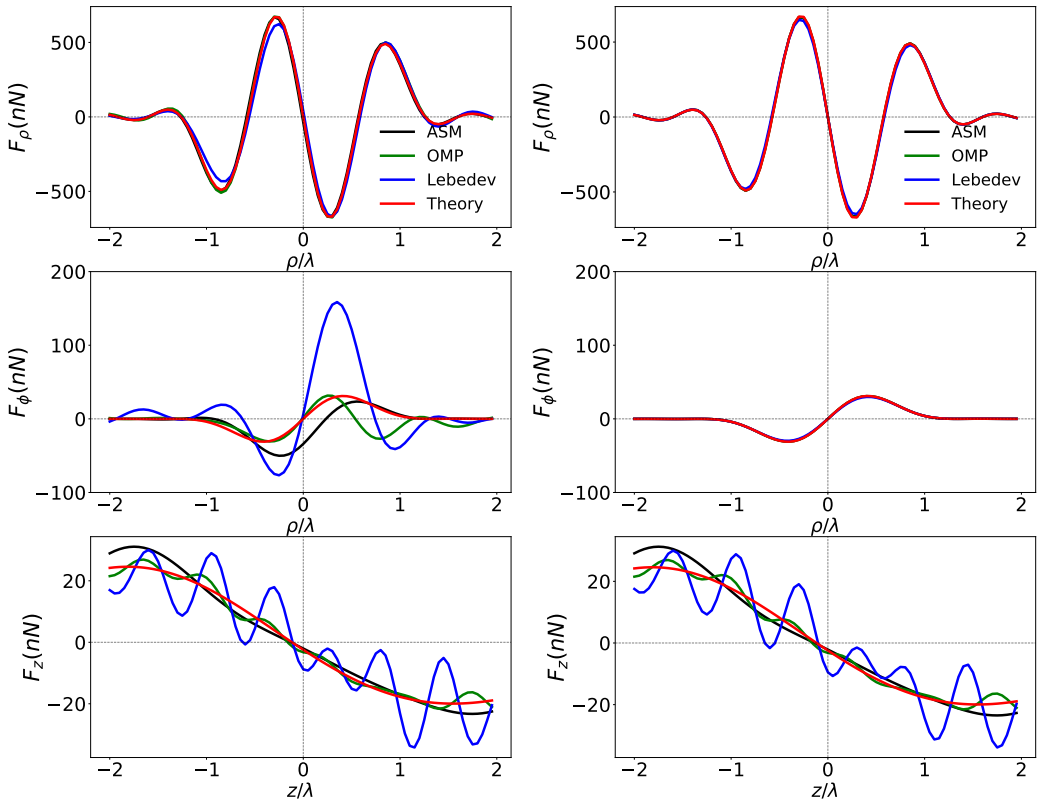

Figure 3.12: (Left) radiation force exerted on a polystyrene sphere of radius $r = 0.1\lambda$ with all the beam shape coefficients, and (Right) with only the beam shape coefficients on column $m = 1$.

Then, considering that the associated Legendre functions $P_n^m(\cos(\theta))$ satisfy the relation :

$$P_n^m(-x) = (-1)^{(n+m)} P_n^m(x), \tag{3.19}$$

with Eq. (2.17) and (2.16), the BSC of the wave propagating in the opposite direction can be computed by multiplying the coefficients by $(-1)^{(n+m)}$. In Fig. 3.13, the axial force for the progressive wave only and with the counterprogating wave superposed are plotted. Comparing with Fig. 3.12, oscillations with the same periodicity but weaker amplitudes are obtained. The difference of amplitude is expected since the 5% noise is applied differently and does not result in the same signal to noise ratio.

There remains to explain why the Lebedev method is more sensitive to the noise than the other two methods. In our simulation, the random noise amplitude is evenly distributed between -5% and 5% of the maximum pressure of the incident beam in all three cases. However for Lebedev quadrature, the pressure field is sampled at the surfaces of two spheres with radius

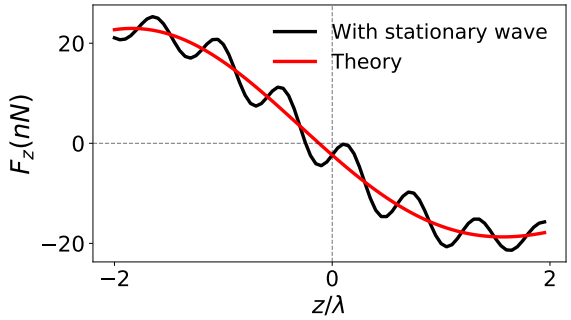

Figure 3.13: Axial force exerted on a polystyrene sphere of radius $r = 0.1\lambda$ with theoretical coefficients A_n^m (black) and theoretical coefficients with a counter propagating wave with 0.5% amplitude (red).

r =7.11 mm and r =7.45 mm where the wave is either yet converging, $z < 0$, or diverging, $z > 0$. Since the wave is sharply focused, on these spheres its amplitude is therefore relatively weak. This results in a poorer signal to noise ratio (SNR). By calculating the SNR at a measurement point where the signal is the maximum for each method, we obtain the results of 22.5, 32.2 and 32.5 dB for the Lebedev quadrature, OMP and ASM respectively. Note that the noise we add in the incident beam is a random value between −5% and 5% of the maximum pressure, so in the SNR calculation, the amplitude of noise taken into account is the mean value of the total noise, which is equal to 2.5%, i.e. 32 dB, of the maximum pressure. On the contrary, the set of points used either inside a spherical volume (OMP) or on a focal plane (ASM) contains locations where the pressure amplitude is maximum and where the SNR is about 10 dB larger than the Lebedev quadrature. In order to explore the influence of the radius of the sphere and confirm the role played by the SNR, the OMP method is now applied in conditions similar to the ones used for Lebedev quadrature. The pressure field is sampled on a set of points randomly distributed on two spherical surfaces for: r =7 mm and r =10 mm. The results are presented on Fig. 3.14. When the sphere radius is the same as for Lebedev method, r =7 mm, the axial force obtained by the two methods are similar with oscillating errors of about the same period and amplitude. Besides, if we increase the radius to r =10 mm, the fluctuations become stronger as expected since the SNR is even more degraded. So according to these results, we can conclude that the oscillations are related to the poorer SNR in Lebedev method. Moreover, the choice of the sphere radius used in the Lebedev quadrature is constrained by the decreasing amplitude of Bessel functions of high order, Fig. 3.2. Thus, decreasing the radius below r =7 mm in our test case would increase the truncature error.

To compare the numerical estimation of the forces by different methods (with all the BSC

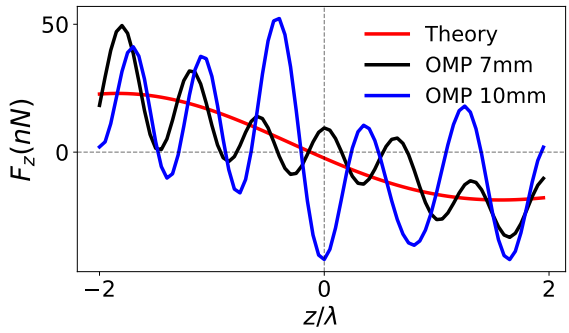

Figure 3.14: Axial force exerted on a polystyrene sphere of radius $r = 0.1\lambda$ with coefficients computed by OMP method on two spherical surfaces (black and blue) and the theoretical force (red).

A_n^m), the relative errors between the force calculated with the A_n^m, F, in the presence of noise and the force computed with the $A_{n_{th}}^m$, F_{th}, are then calculated :

$$err_{force} = \frac{1}{K}\frac{\sum_0^K |F - F_{th}|}{max|F_{th}|}. \tag{3.20}$$

Where K is the total number of positions where the forces are estimated. The results are presented in Tab. 3.2. We can conclude that both the OMP and ASM are effective methods for estimating the radiation force from pressure field measurements with very low relative error as presented in Tab. 3.2. The task is nevertheless difficult since small errors potentially result in spurious standing waves and the radiation pressure exerted by standing waves is much stronger than for progressive waves.

Relative error	T-design	Lebedev	OMP	ASM
F_ρ	0.097	0.036	0.012	0.018
F_ϕ	2.59	0.87	0.23	0.22
F_z	0.38	0.29	0.056	0.096

Table 3.2: Relative errors of the forces for three methods.

3.6 Influence of noise on coefficients and forces estimations

In the previous section, we have observed that the SNR is crucial for retrieving the BSC. However, the sensitivity to the noise level in the wavefield can differ from method to method. Thus in this section, we will analyze the influence of the noise on the BSC and radiation forces. As shown in Fig.3.15, the BSC are computed by each method with different noise level fields.

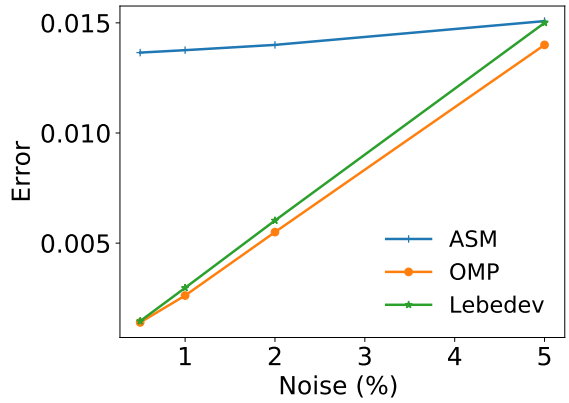

Figure 3.15: Relative errors of the coefficients A_n^m for different methods as a function of the noise.

As can be seen in Fig. 3.15, the relative errors of the BSC (A_n^m) for the three methods are proportional to the noise level. For the Lebedev double layer and OMP method, the relative errors increase more rapidly than the ASM method. The ASM method appears to be more constant under the influence of the noise. In Fig. 3.16 depicted the influence of noises in force estimations. Same as the BSC, the errors of the radiation forces are proportional to the noise level. When the noise level is under 2%, if we compare the relative errors of radial and axial forces, the OMP and Lebedev quadrature show a better performance in the force estimations with smaller relative errors. However, as the noise level grows, the errors of Lebedev quadrature rise more quickly than the other methods. For noise under 5%, the relative errors of OMP method are always the smaller of three methods, even for the axial force. In Fig. 3.12, although, in the F_z of OMP method exists some oscillations, the relative errors are smaller than the ASM method. Nevertheless, the relative errors of the ASM for both the BSC and radiation forces are more consistent with the variation of noise level. Therefore, the ASM is a method that gives reliable results and is less sensitive to the noise.

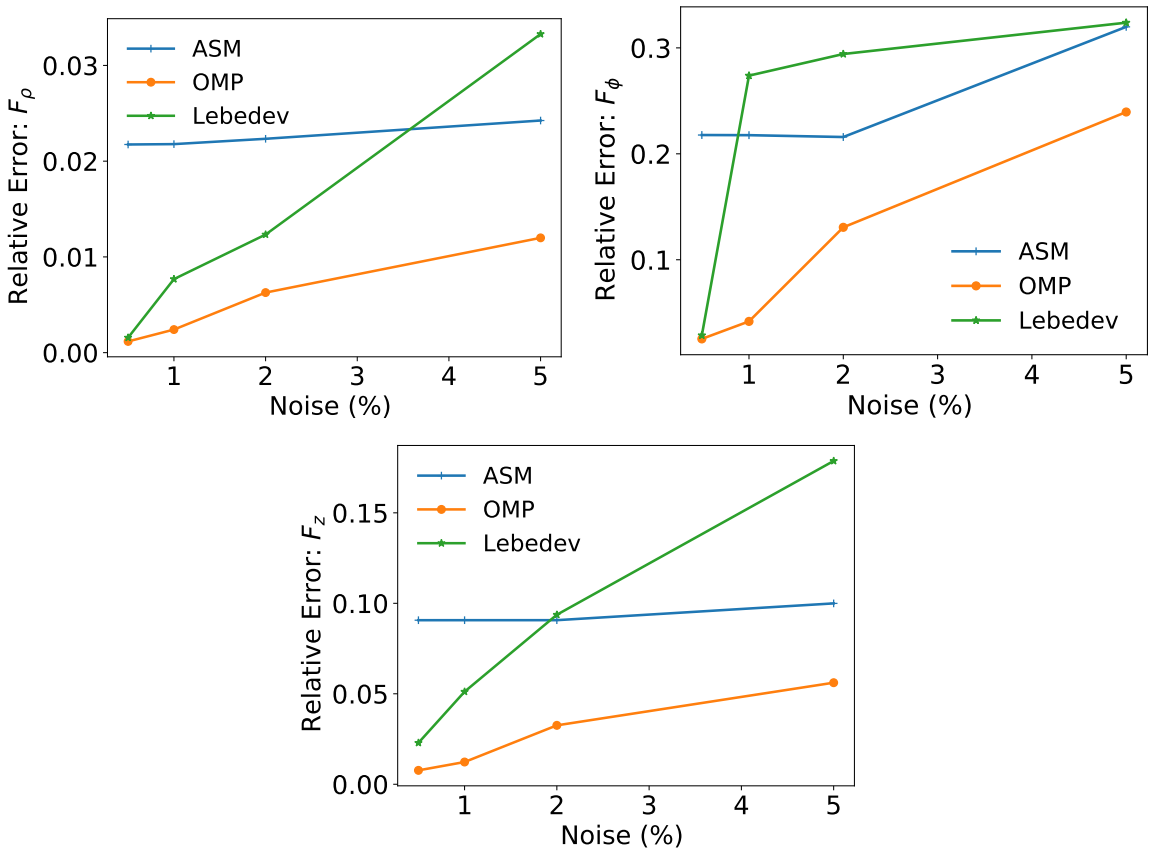

Figure 3.16: Relative errors of the radiation forces for different methods as a function of the noise.

3.7 Experimental measurements

In this section, the three methods are applied on experimental data. The experimental set-up, the method used to synthesize the pressure fields, the optimization of this method for the pressure fields of interest in the context of acoustic tweezers are described in detail in the next chapter. Here we just briefly mention the main features. A focused Gaussian beam, with charge $m' = 0$, and a focused vortex beam with charge $m' = 1$ have been synthesized. The incident sound beam was then measured by a calibrated needle hydrophone of 0.2 mm (0.2λ) diameter (Precision Acoustics Ltd, UK) on three different grids corresponding to the different algorithms presented in sections 3.2-3.4. The measurement grids are all centered on the focal point of the vortex beam. For each location of the hydrophone, an ultrasound burst of 10 cycles is repeated 128 times and the records are averaged to increase the SNR. For each grid, the SNR at the maximum pressure point is calculated: 45.6, 54.5 and 53.7 dB for the Lebedev quadrature, OMP method and SAM respectively. The experimental SNR is 20 dB lower than

the SNR in section 3.5. We noticed that the SNR of Lebedev quadrature is always 10 dB lower than the others methods, this fact remains true in the experiment. As we discussed in section 3.5 on spheres used in Lebedev method, the maximum acoustic signal has a lower amplitude compared to the other two methods, i.e OMP and ASM.

After these measurements on the different grids, we apply the three methods described in sections 3.2-3.4 to estimate the coefficients. The obtained beam shape coefficients completely describe the field. Eq. (2.17) can then be used to calculate a reconstruction of the field in any position. To compare direct experimental measurements of the acoustic field and the field reconstructed with the estimated beam shape coefficients by Eq. (2.17), we measured the acoustic pressure on the transverse plane (x, y) (on the ASM grid) and the vertical plane (x, z) (on a rectangular grid of dimension 7 mm $\times$20 mm ($5.6\lambda \times 16\lambda$) with steps of 0.4 mm $\times$0.3 mm ($0.3\lambda \times 0.2\lambda$)). A DFT is then used to get the measured pressure in the Fourier domain and then extract the modulus at 1.2 MHz. Fig 3.17 displays the computed and measured modulus of the pressure field at this frequency. We carried out this comparison for the focused Gaussian and focused vortex beam.

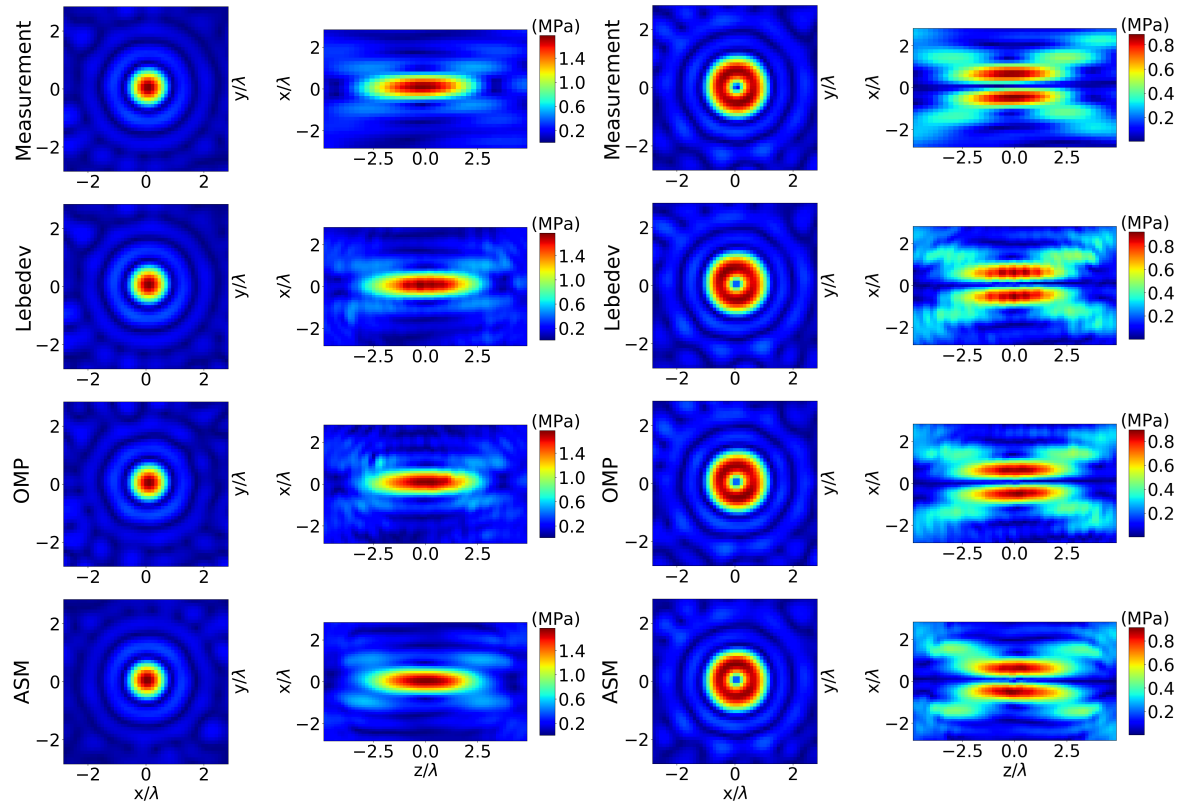

Figure 3.17: Reconstruction of the incident beam for the focused Gaussian beam (Left), and the focused vortex beam with $m' = 1$ (Right).

The reconstructed fields computed with the three different methods are in very good agreement with the direct measurements. On the lateral plane (x, y), the main lobe is perfectly recovered, and in the case of the focused vortex beam, the small anisotropy on the bright ring is accurately estimated. Compared to simulated results of the previous section, the noise is not the single source of discrepancy between A_n^m and $A_{n_{th}}^m$ and as consequence between F and F_{th}, Eq. (3.20). The secondary ring of high pressure modulus characteristic of diffraction by a truncated aperture, i.e. the array of transducers, is also efficiently estimated. The inverse filtering while very efficient does not achieve a perfect synthesis of the looked for pressure fields (see Fig. 3.17). For instance, the experimental measurements are not perfectly axisymmetric and this will have an impact on the azimuthal force. For the axial plane, (x, z), OMP and ASM methods also provide quite a good reconstruction on main and secondary lobes. The 'X-shape' and high intensity at the focus, features expected for sharply focused beam, are perfectly reproduced, while the Lebedev quadrature estimation has some spurious amplitude oscillations. These oscillations have a comparable period with the one observed on the axial force F_z (Fig.

3.12) in the numerical simulation when noise was present. We provided an explanation for this phenomenon in section 3.5. As a result, both the OMP and ASM are able to estimate the BSC and hence the acoustic pressure field in the volume of interest around the focus.
Finally, we use these obtained coefficients of the focused Gaussian beam and the vortex beam $m' = 1$ to calculate the radiation forces exerted on polystyrene spheres of radius $r = 0.1\lambda$ with Eq. (2.21, 2.22, 2.23). The results are shown on Fig. 3.18 and Fig. 3.19. The axial force obtained with Lebedev method is not presented on the Figures since it's very fluctuating like its reconstruction on (x, z) plane. As in the previous section, the relative error of the experimental forces for Gaussian beam and vortex are calculated and reported in tables below Tab.3.3, 3.4.

Relative error	Lebedev	OMP	ASM
F_ρ	0.036	0.036	0.012
F_z	0.23	0.11	0.07

Table 3.3: Relative errors of the experimental forces for three methods (Gaussian beam).

Relative error	Lebedev	OMP	ASM
F_ρ	0.027	0.057	0.034
F_ϕ	0.71	0.6	0.99
F_z	0.8	0.14	0.14

Table 3.4: Relative errors of the experimental forces for three methods (Acoustic vortex $m' = 1$).

According to Fig. 3.18, for a focused Gaussian beam and for each method the radial force is in good agreement with the theoretical one. Theoretically no azimuthal force is applied, but a weak rotational force exists in the force estimation by three methods. This dissimilarity of azimuthal force can be due to the difference between the theoretical field and the experimental field synthesised by inverse filtering, as well as the presence of the noise in the measurements. As for the axial force, the force estimated by ASM is very close to the theoretical one with a very low relative error of 0.07. However, the one calculated by OMP appears to be oscillating though in the reconstruction on plane (x, z) no oscillations are visible. Note that the trap slope is positive for both radial and axial forces. Therefore at the origin the force is null but the equilibrium is unstable. To achieve acoustical tweezers for a stiffer and denser particle

compared to water, cancellation of the pressure field at the focus is required as the case studied below.

For the focused vortex beam of charge $m' = 1$, the forces are quite similar with the ones obtained by adding noise in the numerical assessment of the three methods (see previous section). First, the computation of the radial force agrees with the theoretical force whatever the method. Secondly, the azimuthal forces computed by the experimental BSC are different from the theoretical one. These differences are caused by the value of A_n^m coefficients outside column $m = 1$. If we keep only column $m = 1$ and recalculate the azimuthal force, then, all the forces for different methods superpose with the theoretical force. This filtering makes the field intensity axisymmetric and eliminates any anisotropy in the transverse plane. However, the experimental field presents a slight anisotropy. Thus this discrepancy comes from imperfections on the field synthesis by inverse filtering and on the force estimation due to the noise. The third observation is that both OMP and ASM provide a good estimate of the axial force which has the same negative slope as the theoretical one, i.e same trap strength and stiffness. The OMP axial force has some fluctuations, but performs much better than the Lebedev method, the force obtained with ASM is smooth and close to the theory but with a shift about 0.2λ of the equilibrium position where $F_z = 0$. This shift can be caused by a slight shift 0.2λ (0.25 mm) of the focal point in the experimental measurements. As reported in the Tab. 3.4, even with this shift, the relative error is small (0.14), by cancelling the shift, the relative errors will decrease to 0.091 and 0.085 for the OMP and ASM respectively which are very similar to the numerical estimations in the Tab. 3.2 of section 3.5.

3.8 Conclusion

In this chapter, the computation of the radiation pressure on an elastic sphere exerted by acoustic tweezers is presented. The radiation force is not measured directly but from measurements of the pressure field associated with a model [see Eqs. (2.21-2.23)]. Therefore, to obtain the forces, it is necessary to estimate the BSC from experimental sampling of the pressure field. Three methods were developed: the Lebedev double layer quadrature, the OMP method, and the ASM. We have assessed the methods by simulating a focused vortex of charge $m' = 1$ with 5% noise. The results show that all these methods can recover the coefficients. The forces com-

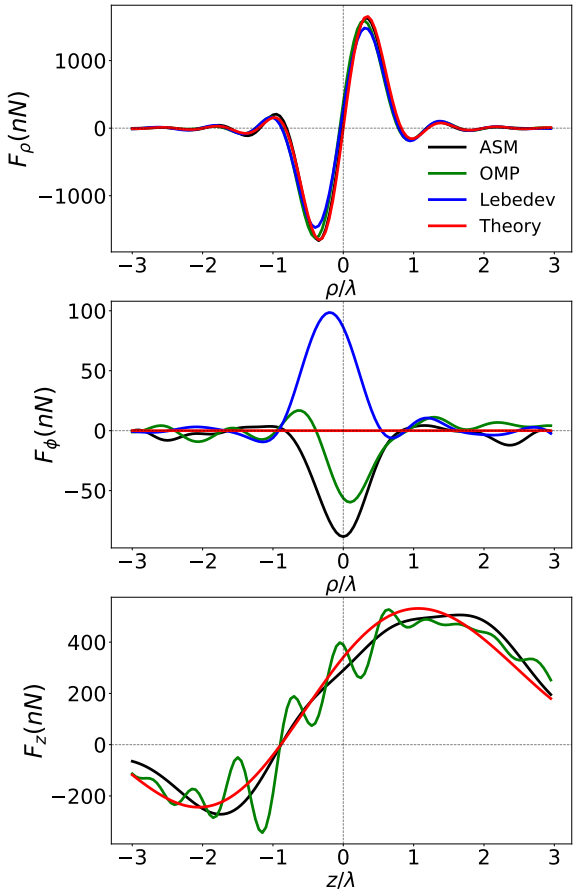

Figure 3.18: Experimental radial F_ρ, azimuthal F_ϕ and axial F_z forces exerted on an polystyrene sphere of radius $r = 0.1\lambda$ in a focused Gaussian beam with charge $m' = 0$.

puted by the different methods agree well with the theory, apart from the Lebedev quadrature for which the axial force is fluctuating.

The experimental verification of these methods is done with two kinds of beams: a focused axisymmetric non-vortex beam ($m' = 0$) and a focused vortex of charge $m' = 1$. The methods introduced previously were applied to compute the experimental BSC and radiation forces. To confirm the BSC obtained are comparable with the synthesized acoustic beams, we have measured, in addition, the incident beam pressure in plane (x, z) and (x, y). Compared with the direct measurements in plane (x, y), the reconstructions of the field by three methods are similar and almost identical. Nevertheless, for the (x, z) plane reconstruction, the field rebuilt by the Lebedev quadrature contains a lot of oscillations. Apart from that, both the OMP method and ASM accord with the experimental measurement. From the analyze of the forces, the OMP and angular spectrum method permit to predict the radial and axial forces appropriately except the azimuthal force which is sensitive to the noise outside the column $m = 1$ of

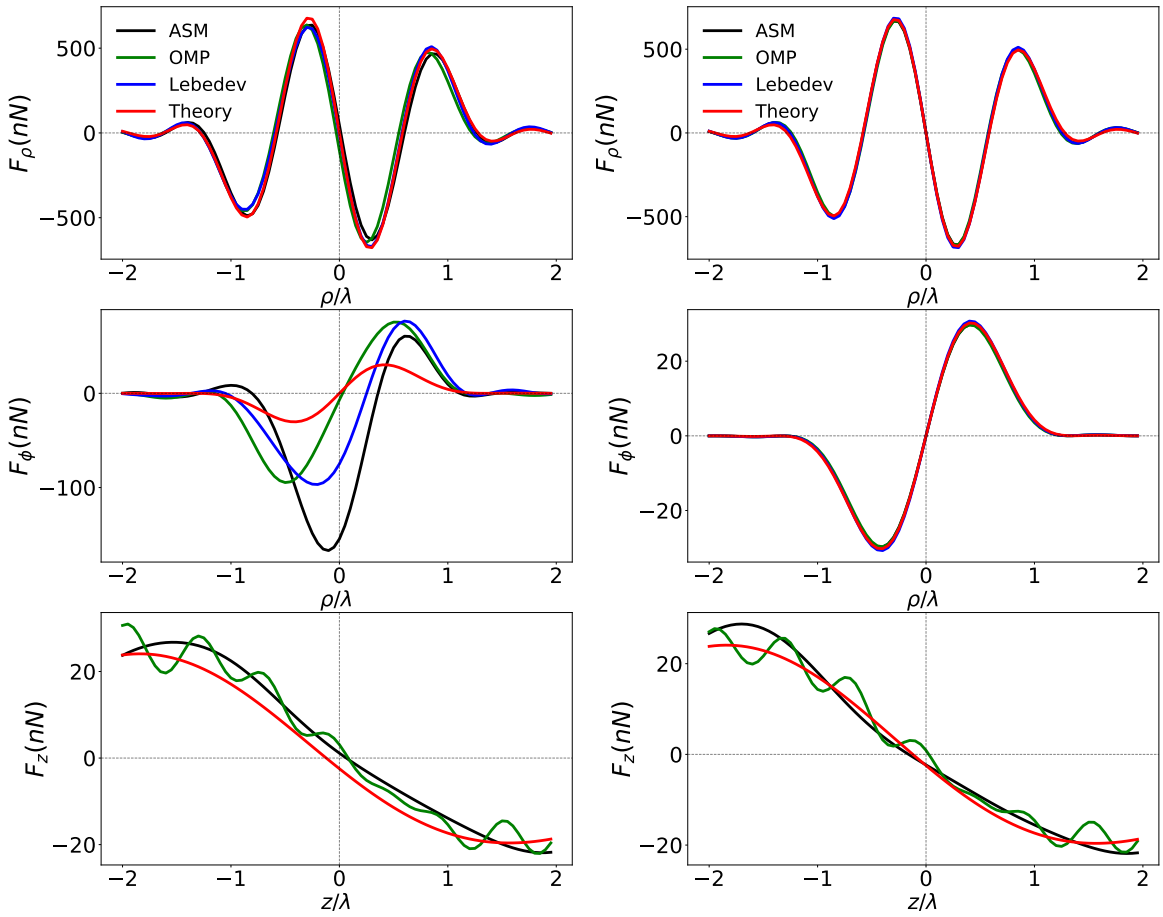

Figure 3.19: Experimental radial F_ρ, azimuthal F_ϕ, axial F_z forces exerted on an polystyrene sphere of radius $r = 0.1\lambda$ in a focused vortex beam with charge $m' = 1$, calculated by the total coefficents (Left), and only by the coefficients in column $m = 1$ (Right).

the coefficients.

Moreover, we have observed that the low signal-to-noise-ratio (SNR) of Lebedev method is responsible for the fluctuations in the axial force as well as the reconstructed field in plane (x, z). Since the radiation pressure due to a standing wave is much stronger than the one due to a progressive wave, even slight noise inducing a counterpropagating wave can lead to oscillations in axial force. Therefore, increasing the SNR in the field measurement is of importance, especially for the accuracy of axial force computation. In this chapter, the OMP and ASM were validated both in simulation and experiments to be reliable methods. With the help of these methods, we are able to anticipate the radiation forces by measuring the acoustic field.

Chapter 4

Acoustic field synthesis

4.1 Introduction

The experimental realization of acoustic tweezers is required to be able to tailor an adequate wavefield with a spatial organization allowing the trapping effect [45]. Different fields can be used to trap particles such as a focused cylindrical vortex beam [46], a spherical vortex beam [42] or a bottle beam [96]. Different solutions exist to produce these complex wave fields. Acoustic vortex synthesis systems have been developed using either multi-elements with arrays of transducers or mono-elements. The first acoustic vortex at ultrasonic frequency was produced using a source consisting of a four-panel transducer[97]. Most of the recent methods involving the formation of the acoustic vortex beam are based on transducer arrays [117, 96, 46, 118, 98], which serve as independent sources modulating the phase and amplitude individually. For mono-element devices, the vortex can be generated: using a spiral grating [119, 120]; with a ferroelectret film gluing onto a helical surface substrate [121]; by a spiraling interdigitated transducers (IDTs) printed at the surface of a piezoelectric substrate [122]; and a spiraling transducers obtained by folding a spherical acoustical vortex on a flat piezoelectric substrate [47]; using a metasurface [123] or a optoacoustic absorber surface [124]. Among all these solutions, we choose to use an array of transducers with an appropriate wave field synthesis method. With an array of transducers, multiple methods can be applied to synthesize the desired acoustic field, including time reversal [125], inverse filtering [118, 126] and integrative angular spectrum technologies [127, 128], etc. Inverse filtering is a very general technique for analyzing and synthesizing complex signals that propagate through an arbitrary linear medium.

This method allows for finding the optimal input signals to get a target wavefield. It is based on the measurement of an operator of propagation and the computation of its inverse. In this chapter, we will first recall the theoretical background of the spatio-temporal inverse filter technique. Then, we will present the experimental results obtained for different distributions of measurement points as well as different regularizations of the inverse operator of propagation. Eventually, the sensitivity of the inverse filter on these parameters is studied.

4.2 Spatio-temporal inverse filter background

The inverse filter method consists of three steps: (i) recording the propagation operator of the propagation medium which completely characterizes the medium and the geometry of the experiment; (ii) calculating the inversion of the propagation operator, which is a sensitive step since the direct inversion is not possible; (iii) computing the optimal input for the transducer array.

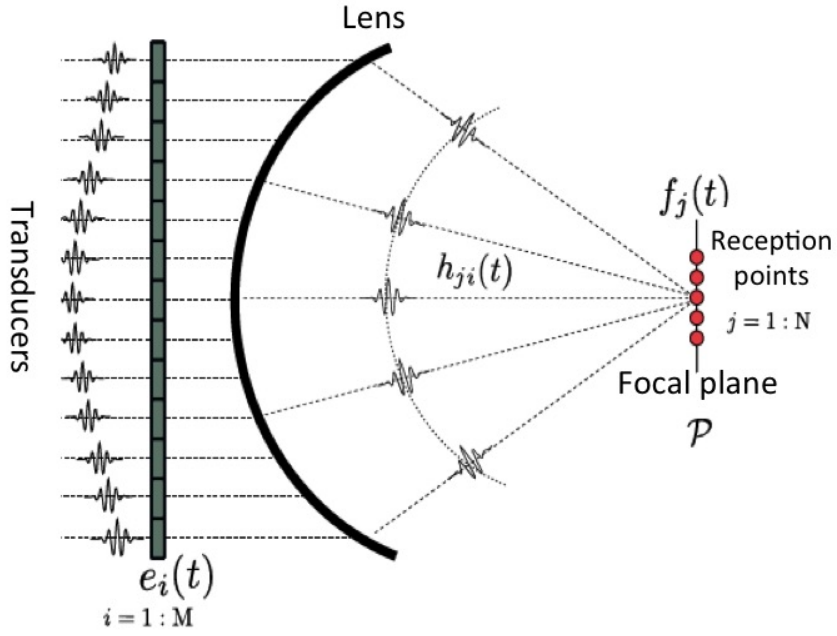

Figure 4.1: Principle of the spatio-temporal inverse filter method. For a set of M transducers, a control plane P of N points is scanned by the hydrophone. All information related to the physical system is contained in the impulse response $h_{ji}(t)$.

To acquire the propagation operator, first, the geometry of the experiment is chosen. The salient features of the setup are shown in Fig. 4.1: the source is a concave array of $M = 127$

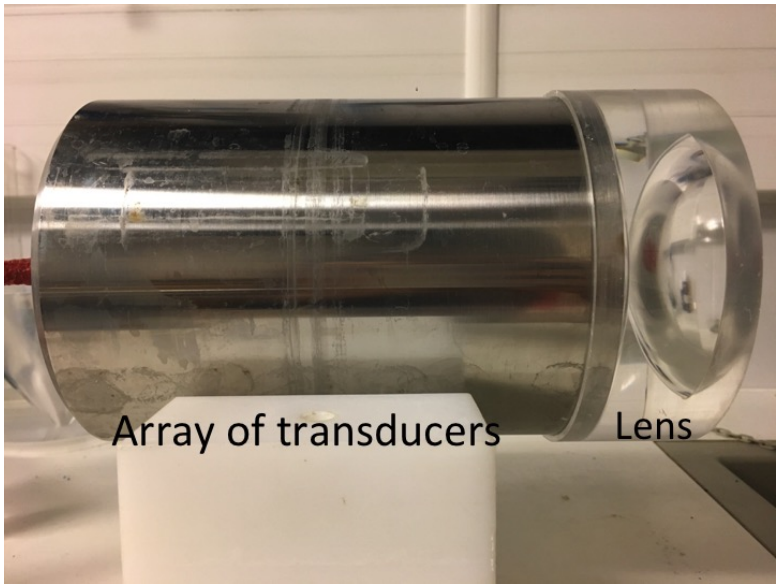

Figure 4.2: Bi-concave lens with transducer array.

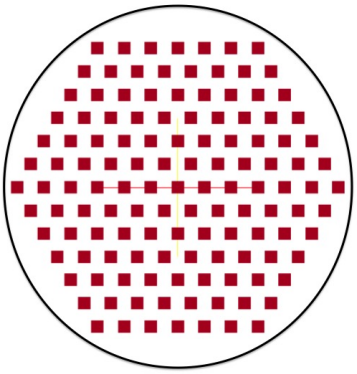

Figure 4.3: Positions of the 127 transducers.

piezoelectric transducers (central frequency around 1.15 MHz) with a focal distance equal to 45 cm. A bi-concave lens in PMMA [45] is added to the array of transducers in order to decrease the focal distance to about 6 cm (Fig. 4.2). The positions of the transducers are shown in Fig. 4.3. The surface of each transducer is a hexagon of $62.82\,\mathrm{mm}^2$, and the total aperture of the transducer array is 50 mm. Then, we consider N control points whose positions are distributed in the volume of the medium. The distributions depend on the target field. One of the objectives in this chapter is to study the influence of the control point distribution on the wave field synthesis. At each control point, the pressure field is measured. Let $f_j(t)$ be the signal received at the jth control point ($1 \leqslant j \leqslant N$) and $e_i(t)$ ($1 \leqslant i \leqslant M$), the input signal on the array of transducers. The impulse response between transducer i and control point j is denoted $h_{ji}(t)$. It is obtained by means of a pulse whose center frequency is chosen as a function of the bandwidth of the piezoelectric transducers (here centered around 1.2 MHz). The impulse response includes all the propagation effects through the medium under investigation as well as the acousto-electric responses of the transducers and hydrophone. Hence, the signal received on the jth control point, which was emitted by the ith transducer can be written:

$$f_j(t) = \sum_{i=1}^{M} h_{ji}(t) * e_i(t), \tag{4.1}$$

where the symbol '*' denotes the convolution product. The Fourier transform of this equation gives:

$$F_j(\omega) = \sum_{i=1}^{M} H_{ji}(\omega) E_i(\omega). \tag{4.2}$$

Eq. (4.2) can be viewed as a matrix/vector product:

$$\underline{F}(\omega) = \underline{\underline{H}}(\omega)\underline{E}(\omega). \tag{4.3}$$

Where $\underline{\underline{H}}$ is the frequency response of the system (size: $N \times M$), which describes the propagation of signals from the array of transducers to the control points and thus is called the propagation operator. The vectors $\underline{E}(\omega)$ (length: N) and $\underline{F}(\omega)$ (length: M) contain the spectra of the transmitted and received signals respectively.

We aim to find the optimal signals to send ($\underline{E}$) by the array of transducers to generate the target field $\underline{F}$ on the control points after propagation. A naive approach consists in inverting

directly the Eq. (4.3). However, the matrix $\underline{\underline{H}}$ is not square and cannot be inverted directly. Instead, the pseudo inverse is computed with a singular value decomposition (SVD). The SVD allows adding a step of regularization through the choice of a cut-off in the singular values. First, the matrix $\underline{\underline{H}}$ is written as the product of three matrices:

$$\underline{\underline{H}} = \underline{\underline{U}}\,\underline{\underline{S}}\,\underline{\underline{V}}^{\dagger}. \tag{4.4}$$

where $\underline{\underline{U}}$ is a unitary matrix (dimensions: $N \times N$), $\underline{\underline{S}}$ a diagonal matrix (dimensions: $N \times M$) whose coefficients are the singular values (positive or null) and $\underline{\underline{V}}^{\dagger}$ is the conjugate transpose of matrix $\underline{\underline{V}}$ (dimensions: $M \times M$) which is also a unitary matrix. With these notations, the pseudo inverse of matrix $\underline{\underline{H}}$ is:

$$\underline{\underline{H}}^{-1} = \underline{\underline{V}}\,\underline{\underline{S}}^{-1}\underline{\underline{U}}^{\dagger}. \tag{4.5}$$

In this equation, the matrix $\underline{\underline{S}}^{-1}$ is diagonal, and its components $1/\lambda_i$ are simply the inverse of the components λ_i of $\underline{\underline{S}}$. The propagation operator is obtained by the measurement of the impulse responses. Therefore it contains not only the physical information but also some noise. It should be noticed that small errors in $\underline{\underline{H}}(\omega)$ (and so in $\underline{\underline{S}}$) can produce large errors in $\underline{\underline{H}}^{-1}(\omega)$ (because of $\underline{\underline{S}}^{-1}$). Indeed, some of these eigenvalues can be very small, thus sensitive to noise. After the inversion, $1/\lambda_i$ tends to infinity for small λ_i. To get rid of these unexpected errors, a cut-off is applied to the singular value decomposition: components corresponding to the smallest eigenvalues are replaced by zero in $\underline{\underline{S}}^{-1}$ and gives a regularized inverse propagation operator $\hat{\underline{\underline{H}}}^{-1}$ defined by:

$$\hat{\underline{\underline{H}}}^{-1} = \underline{\underline{V}}\,\hat{\underline{\underline{S}}}^{-1}\underline{\underline{U}}^{\dagger} = \underline{\underline{V}} \begin{bmatrix} \frac{1}{\lambda_1} & 0 & & \cdots & & 0 \\ 0 & \ddots & & & & \\ & & \frac{1}{\lambda_{Ne}} & \ddots & & \vdots \\ \vdots & & \ddots & 0 & & \\ & & & \ddots & 0 & \\ 0 & & \cdots & & 0 & 0 \end{bmatrix} \underline{\underline{U}}^{\dagger}. \tag{4.6}$$

With the regularized inverse propagation operator $\hat{\underline{\underline{H}}}^{-1}(\omega)$, it is straightforward to get the

emission vector to synthesize the target field $\underline{F}(\omega)$:

$$\underline{E}(\omega) = \underline{\underline{\hat{H}}}^{-1}(\omega)\underline{F}(\omega). \tag{4.7}$$

In the next section, this method is applied experimentally to synthesize different fields: a Gaussian beam, a focused vortex beam and a spherical vortex beam with different distributions of control points. A special emphasis is also placed on the choice of the cut-off value. Indeed, if the cut-off is too high, some physical singular values will be neglected. On the contrary, if the cut-off is too low, some noise can contaminate the inverse operator. Therefore, it is strongly dependent on the quality of experimental measurement. One can determine the optimal cut-off value by trying different values.

4.3 Experimental synthesis of acoustic fields

In this section, different types of acoustic fields are synthesized using the spatio-temporal inverse filter method, as presented in the previous section. The distribution of control points, as well as the distribution of transducers in the inverse filter technique are important factors that will influence the efficiency of the method. Only one array of transducers is available, and the PMMA lens is originally made to optimize its geometry for the synthesis of these kinds of sharply focused target acoustic fields. In the following is described the attempts to carry out an optimization of the control points distribution. Three distributions of the control points were used and compared.

4.3.1 Synthesis of acoustic fields with Lebedev points distribution

Lebedev grids have already been introduced in chapter 3 as a method of quadrature. The Lebedev points are defined on a unit sphere (x_i, y_i, z_i) derived by Sobolev [111]. As we explained in chapter 3, Lebedev quadrature has optimal efficiency, i.e. the number of points required is the smallest, and the point spacing is roughly constant and well adapted to the finite size of a hydrophone. Knowing that the number of points is fixed by the maximum polynomial order used to expand the field and yields, in our case, 974 points distributed on a sphere, we assessed the efficiency for a sphere sampled with 974 points. A calibrated needle hydrophone of 1 mm

diameter was used to measure the signal at each control point with 16 averages to increase the signal-to-noise ratio (SNR). The sphere radius is 20 mm. As a consequence, the interval between neighbouring points is about 2.2 mm on average, twice the hydrophone size (Fig. 4.4).

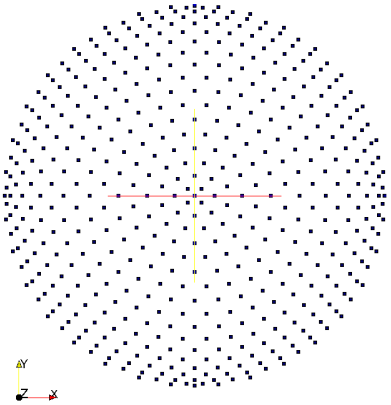

Figure 4.4: Distribution of control points on a sphere of radius 20 mm with Lebedev distribution.

The measurement on these control points allows us to measure the impulse responses $h_{ij}(t)$, and after a Fourier transform, the propagation operator $\underline{\underline{H}}(\omega)$. We denote the first distribution by $\underline{\underline{\hat{H}}}_1(\omega)$. The transducers bandwidth limits the frequencies available for the field synthesis. Therefore, the first step consists of selecting the bandwidth after a Fourier transform of the impulse responses, as shown in Fig. 4.5. The sampling frequency is 25 MHz and the number of points for the Fourier transform is 1024 so that the frequency sampling interval is 24.4 kHz. The spectrum maximum is around 1.2 MHz. As depicted in Fig. 4.5, about 60 sampling frequencies are sufficient to describe the transfer function from 0.5 to 2 MHz. Thus, the other frequency components are set to zero. The remaining steps of the inverse filter method are carried out on this limited set of frequencies. To obtain the inverse propagation operator matrix $\underline{\underline{H}}^{-1}(\omega)$ the singular values are computed, as shown in Fig. 4.6. From the figure we find that in this distribution most of the singular values reach their maximum at 1.2 MHz as expected and spread on a dynamic of about 20 dB. There is almost no noise in the eigenvalues. The dark line represents the cut-off threshold, and removes the smallest singular values that have a flat behavior.

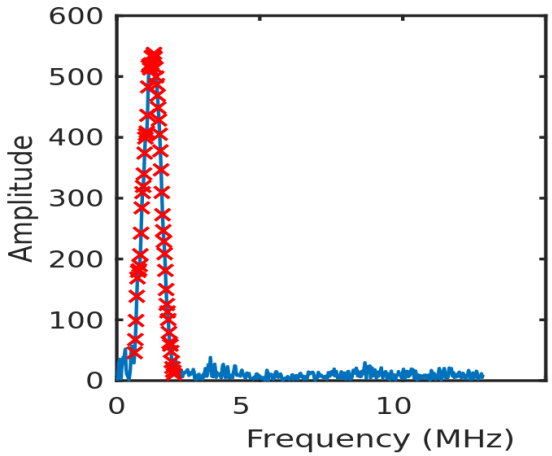

Figure 4.5: Signal bandwidth selection.

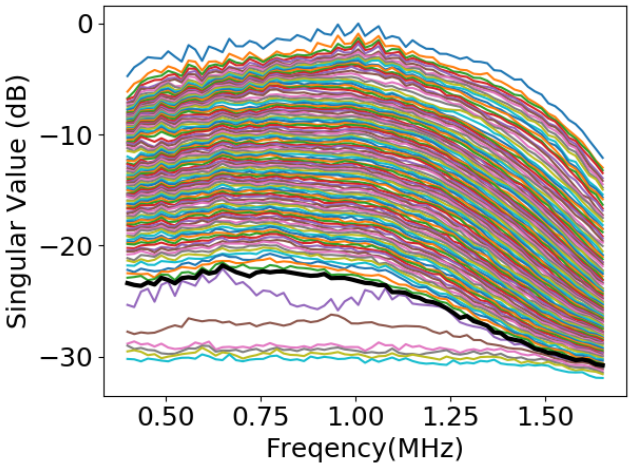

Figure 4.6: Singular values of the propagation operator $\underline{\underline{H}}_1$.

Once the regularized pseudo-inverse matrix $\hat{\underline{\underline{H}}}_1^{-1}(\omega)$ is obtained, the emission vector $\underline{E}_1(\omega)$ can be computed with Eq. (4.7) on a chosen target field $\underline{F}_1(\omega)$. As for the matrix $\underline{\underline{H}}(\omega)$, index 1 is related to the set of control points selected.

A first target field $\underline{F}_1^{fv}(\omega)$ is a vortex of topological charge $m' = 1$ focused with an angle $\alpha_0 = 42.5°$. The BSC coefficients are given by Eq. (2.50). These BSC coefficients are a function of ω. It remains to define the time behavior of the target pressure field. A quasi-monochromatic signal of frequency $f = 1.2\,\text{MHz}$ with a Gaussian envelope (Fig. 4.7) is used in all the following experiments. The emission vector $\underline{E}_1^{fv}(\omega)$ is calculated at each frequency component in the selected bandwidth. Then $\underline{E}_1^{fv}(t)$ is computed with an inverse Fourier transform, and can be transmitted by the transducer array. The emitted acoustic field is scanned on a transverse plane

(x, y) at the focal distance and an axial plane (x, z) centered on the focus. For the plane (x, y), 500 points in polar coordinates sampling a disk of radius r =2.5 mm are used (20 intervals for the polar angle and 25 for the radial distance). For the axial plane (x, z), a set of 2800 points on a cartesian grid are used to sample a rectangle, 40 points on the x-axis and 70 on the z-axis. The sides lengths are 7 mm and 20 mm respectively. Considering that the mesh is much finer for the scans than for the measurement of the impulse responses, we have changed the hydrophone with 1 mm diameter to a new one with 0.2 mm diameter. This smaller hydrophone is used in all scans in this work.

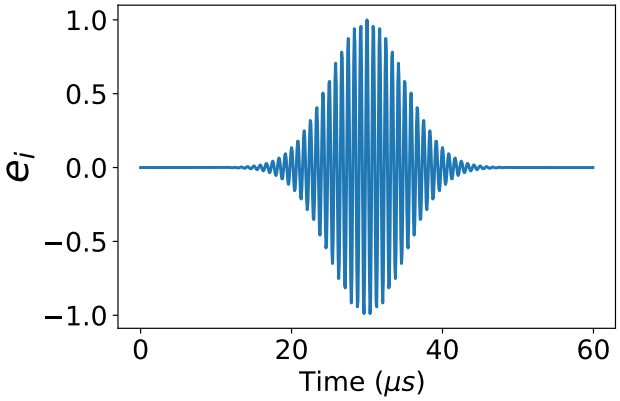

Figure 4.7: Quasi-monochromatic signal of frequency $f = 1.2$ MHz.

As presented in Fig. 4.8, the pressure field measured in plane (x, y) on the left side has the same form as the theoretical one on the right side but the ring is slightly larger. For the axial plane (x, z), Fig. 4.9, the similarity between synthesized and target fields is degraded. Obviously, the pressure field is not entirely symmetric and well-focused. The reason for this less good result can be due to the choice of control points that are used to measure the propagation operator. The sphere has a large radius, and some of the points are too far away from the focal position. Thus the measured signal can be very tiny and result in a low SNR. Therefore, this distribution of control points doesn't work out well enough for our application. Moreover, the points are distributed on a spherical surface, i.e. not in the same transverse plane. As our wave is progressive, the phase of the targeted field is energetically sensitive to errors in the speed of sound. Therefore, we changed to a new distribution in the focal plane in the next section.

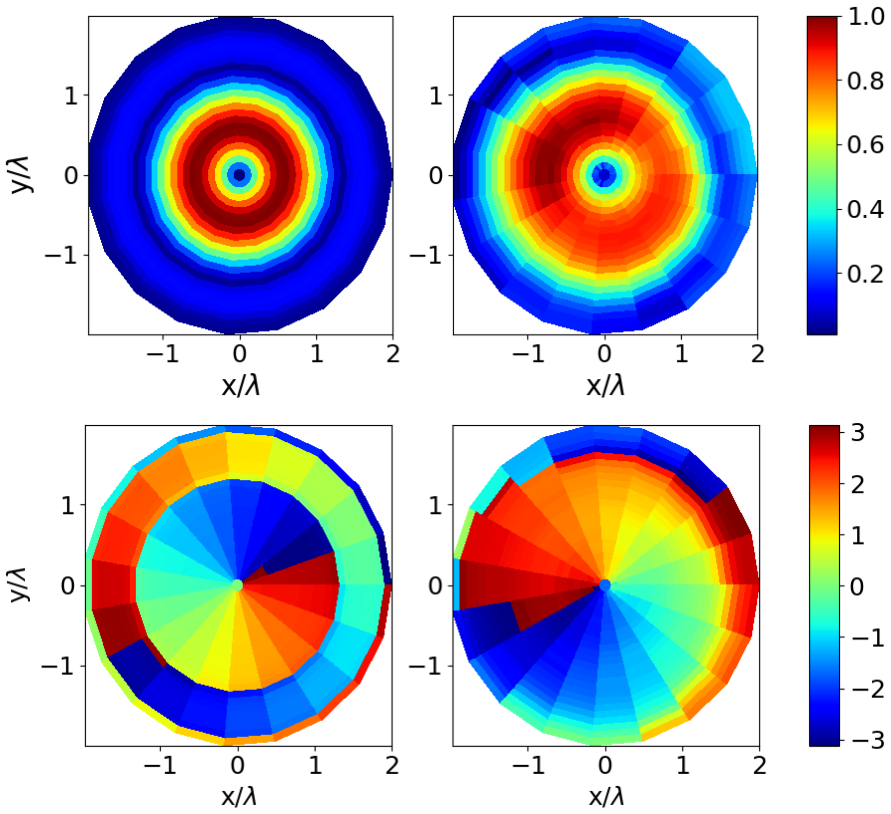

Figure 4.8: Modulus (top) and phase (bottom) of the complex pressure field in plane (x, y) for a focused vortex of charge $m' = 1$; (Left) Target acoustic field; (Right) Measurements (propagation operator: $\underline{\underline{H}}_1$).

4.3.2 Synthesis of acoustic fields with a point distribution located on a disc

The second distribution of control points assessed is a disc of radius 7 mm with 581 points distributed regularly in polar coordinates with 30 intervals on the radial axis and 20 intervals on the polar angle. The disc is located in the focal plane, it is parallel to the array of transducers , and it is centered on the focal point. Compared to the first Lebedev mesh, this distribution is spread on a much smaller surface, and the number of points is increased. Moreover, the points interval on each circle is not constant and decreases with the radius. This results in a more dense grid around the focus, as shown in Fig. 4.10.

Three kinds of acoustic beams are synthesized for this distribution: a Gaussian beam (*i.e.* a focused vortex of charge $m' = 0$) denoted $\underline{F}_2^{fg}(\omega)$, a focused vortex beam of charge $m' = 1$, $\underline{F}_2^{fv}(\omega)$ and a focused spherical vortex beam of charge $m' = 1$, $l = 8$, $\underline{F}_1^{sv}(\omega)$. The BSC for the Gaussian and focused vortex beams are computed with Eq. (2.50). The BSC for the spherical

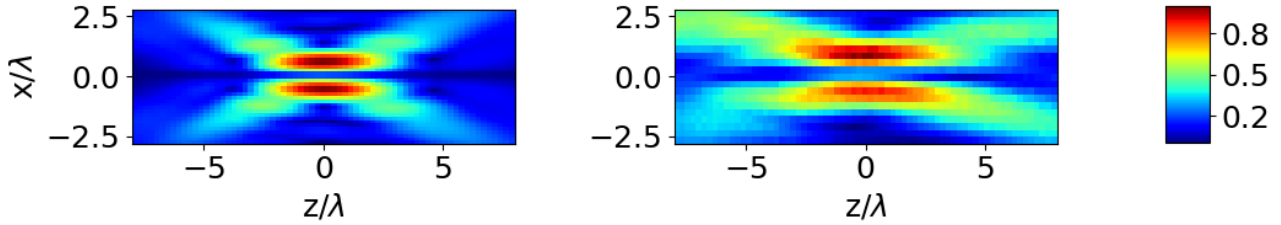

Figure 4.9: Modulus of the complex pressure field in plane (x, z) for a focused vortex of charge $m' = 1$; (Left) Target acoustic field; (Right) Measurements (propagation operator: $\underline{\underline{H}}_1$).

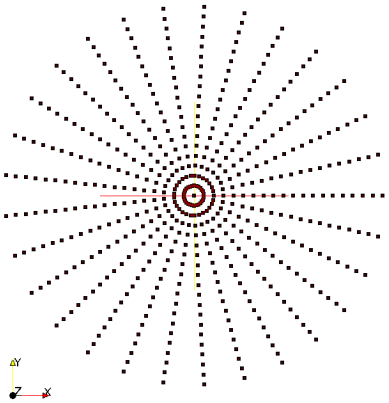

Figure 4.10: Distribution of the control points on a disc of radius 7 mm with a regular distribution on the radial direction and polar angle.

vortex are here given by Eq. (2.51). For these three target fields, the focusing is made with a maximum angle of 42.5° as in the previous section. The same procedure is carried out to calculate the regularized pseudo-inverse matrix $\hat{\underline{\underline{H}}}_2^{-1}(\omega)$, the emission vectors $\underline{E}_2^{fg}(\omega)$, $\underline{E}_2^{fv}(\omega)$ and $\underline{E}_2^{sv}(\omega)$ for all frequencies in the bandwidth and lastly the emission vectors in the time domain.

The three emission vectors are emitted successively with the array of transducers. The acoustic fields in plane (x, y) are measured in a square located at the focal plane and centered at the focus. The side length is 7 mm. The mesh samples the axes x and y with $50 \times 50 = 2500$ points and hence an interval of 0.14 mm.

The modulus of theoretical and experimental fields are presented in Fig. 4.11(a) for $\omega/(2\pi) =$ 1.2 MHz. The top row presents the target fields $\underline{F}_2^{fg}(\omega)$, $\underline{F}_2^{fv}(\omega)$ and $\underline{F}_2^{sv}(\omega)$. The bottom row are the measurements. The experimental and target fields are in good agreement in the case of the Gaussian and focused vortex beams. For the spherical vortex, the measured high-intensity ring is not so uniform with a size slightly smaller than expected. Another discrepancy is visible inside this high-intensity ring, and the field is not perfectly canceled. These similarities and

differences are also present in the phase of the fields, shown in Fig. 4.11(b). The most salient errors are at the center of the spherical vortex where a small phase disc in the theoretical field is not at all reproduced in the experiment.

In the plane (x, z), modulus of the wavefield is presented in Fig. 4.12, target fields are on the left column while the measurements are on the right. Again the agreement is very good for the Gaussian and focused vortex beams. The spherical vortex synthesis is rather good, and the field intensity seems to flow around an obstacle located at the focus. This creates high-intensity gradients in the axial direction in order to get a strong and stiff axial trap. Nevertheless, the experimental synthesis is not perfect, and differences appear mostly behind the focus.

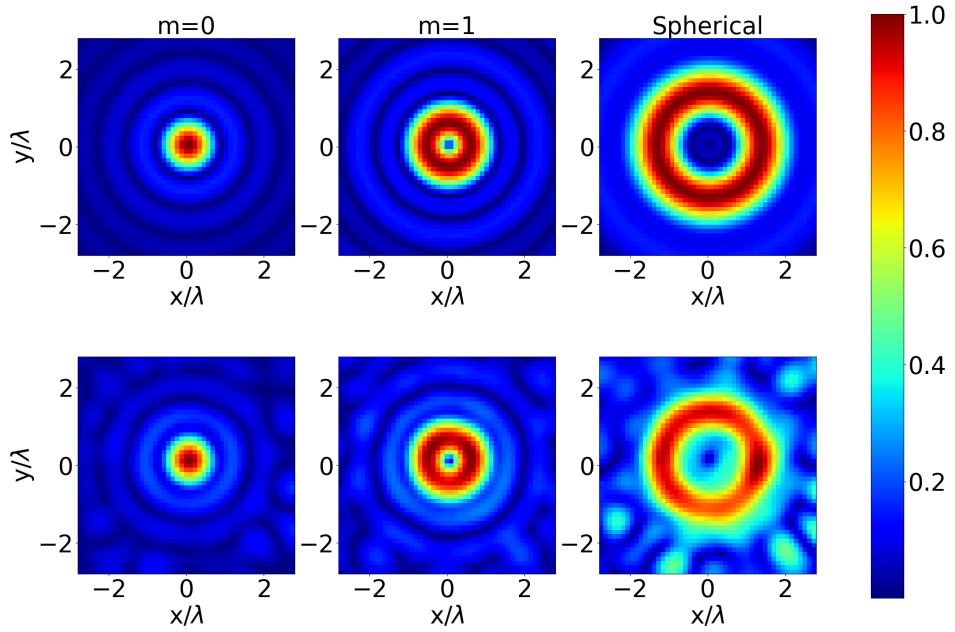

(a) Modulus of the complex pressure field

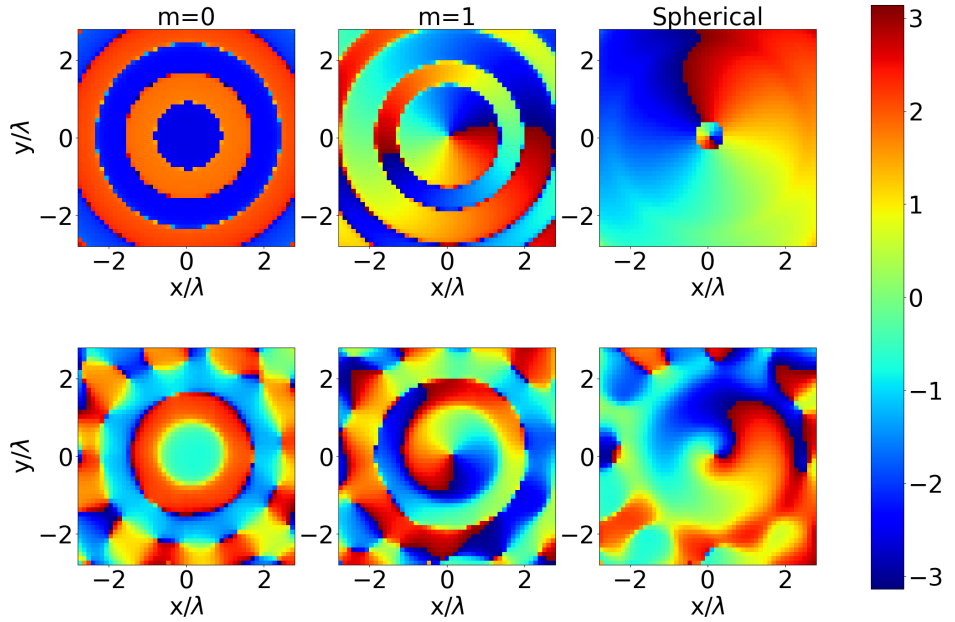

(b) Phases of the complex pressure field

Figure 4.11: Modulus (normalized) and phases of the complex pressure field in plane (x, y) for different acoustic beams: Gaussian ($m' = 0$) and focused vortex ($m' = 1$), spherical vortex with $m' = 1$ and $l = 8$. (Top) Theoretical acoustic field; (Bottom) experimental measurements.

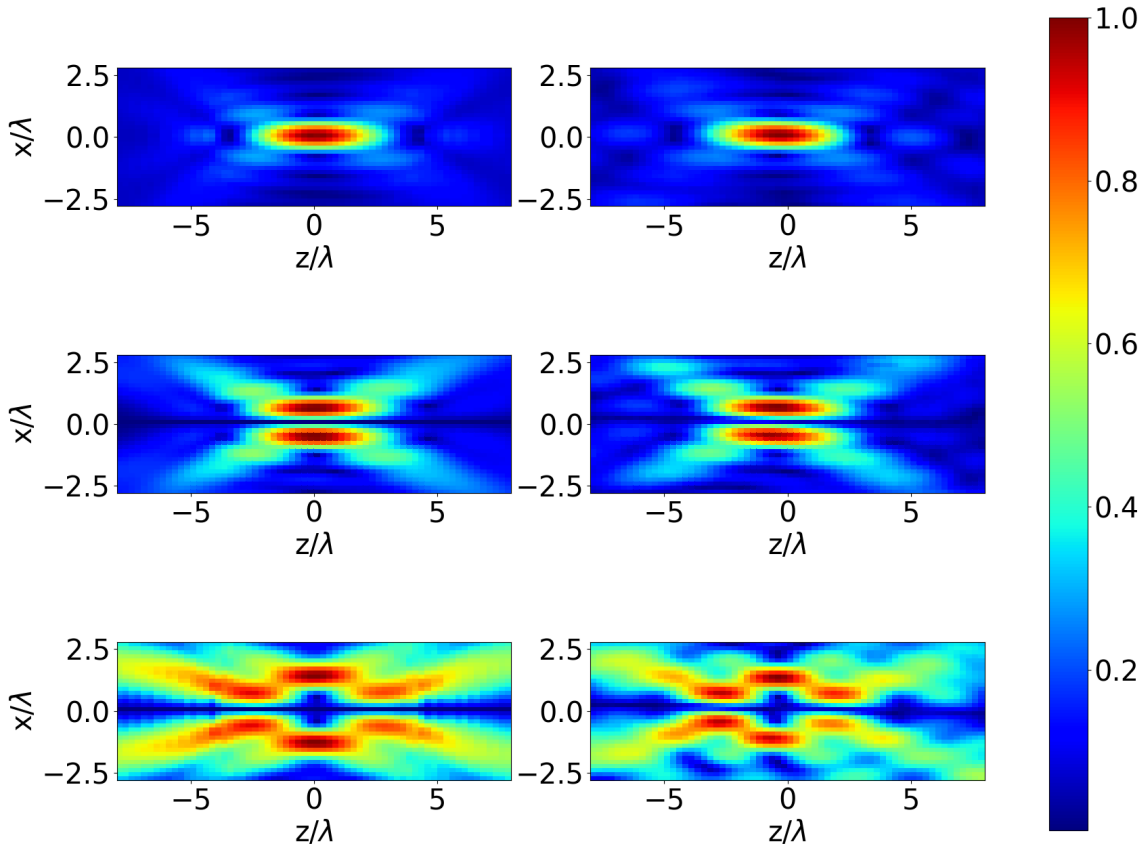

Figure 4.12: Modulus of the complex pressure field in plane (x, z) for different acoustic beams (from top to bottom): Gaussian ($m' = 0$) and focused vortex ($m' = 1$), spherical vortex with $m' = 1$ and $l = 8$. (Left) Theoretical acoustic field; (Right) experimental measurements.

The previous comparisons are qualitative and do not ensure that the radiation forces generated by these waves have the expected characteristics. As described in chapter 3, the BSC can be computed from experimental scans in the (x, y) plane with the angular spectrum method. The BSC obtained for a Gaussian beam, and a focused vortex beam are shown in Fig. 4.13. According to the figure, the experimental BSC represent a similar distribution in column $m = 0$ and $m = 1$ for the Gaussian beam and focused vortex beam respectively, but with some noise outside the column. The comparison of modulus and phase in the core column between the experimental and theoretical BSC are shown in Fig. 4.14. The experimental modulus is close to the theoretical one, especially at the position where the amplitude of BSC is large. Meanwhile, the phase of the focused vortex is also in good agreement with the theory until order $n = 10$.

However, the phase of the Gaussian beam compared to the cylindrical beam is less in agreement with the theory. Knowing the BSC and selecting a target sphere, Eqs. (2.21, 2.22, 2.23) yields the radiation force components. For the comparisons, a polystyrene sphere of radius $a = 0.1\lambda$ is used for the Gaussian and focused vortex beams and a larger $a = 0.45\lambda$ polyethylene sphere for the spherical vortex beam. This choice may seem peculiar. On the one hand, $a = 0.1\lambda$ ensures that the scattering regime corresponds to a rather small sphere where no resonances occur. On the other hand, spherical vortex is designed to optimize the axial force and the selectivity of the tweezers. Since focusing sharpness is limited by diffraction at about one wavelength, these fields are designed for spheres with a diameter close to this limit. However, for this size, resonances occur. We will see in section 5 that a three-dimensional trap can be obtained with our experimental set-up for a very limited choice of material and sphere size. This radiation force is then written in cylindrical coordinates: F_ρ, F_ϕ, F_z. Note that there is one adjustable parameter. Since we don't know *a priori* the antenna gain of our experimental system made of the array and the PMMA lens, we have to fix p_a in Eq. (2.17). To determine p_a, we compute the field in the plane (x, y) with Eq. (2.17), using $p_a = 1$ and the analytical BSC. Thus the maximum located on the intensity ring is determined without p_a. The calibrated pressure measured for the corresponding synthesized field gives the experimental maximum pressure , and thus defines the adjustable parameter p_a. This parameter is estimated for each synthesized field since the antenna gain depends on the chosen target field.

Fig. 4.16 and Fig. 4.17 present the comparisons of the force obtained with the analytical BSC (Eq. (2.50)) and the BSC computed from experimental scans for the Gaussian and focused vortex beams respectively. The estimated radial force F_ρ superimposes almost perfectly with the theoretical forces. Note that a stable equilibrium trap occurs when the force has a negative slope only. Hence, the Gaussian beam does not achieve the tweezers for a polystyrene bead that is denser and stiffer than the surrounding water. The azimuthal forces F_ϕ however, due to the noise outside the column, are different from the theoretical forces (Fig.4.13). The axial, F_z, experimental and theoretical forces are close in both cases. Nevertheless, the equilibrium position of the focused vortex beam is slightly shifted.

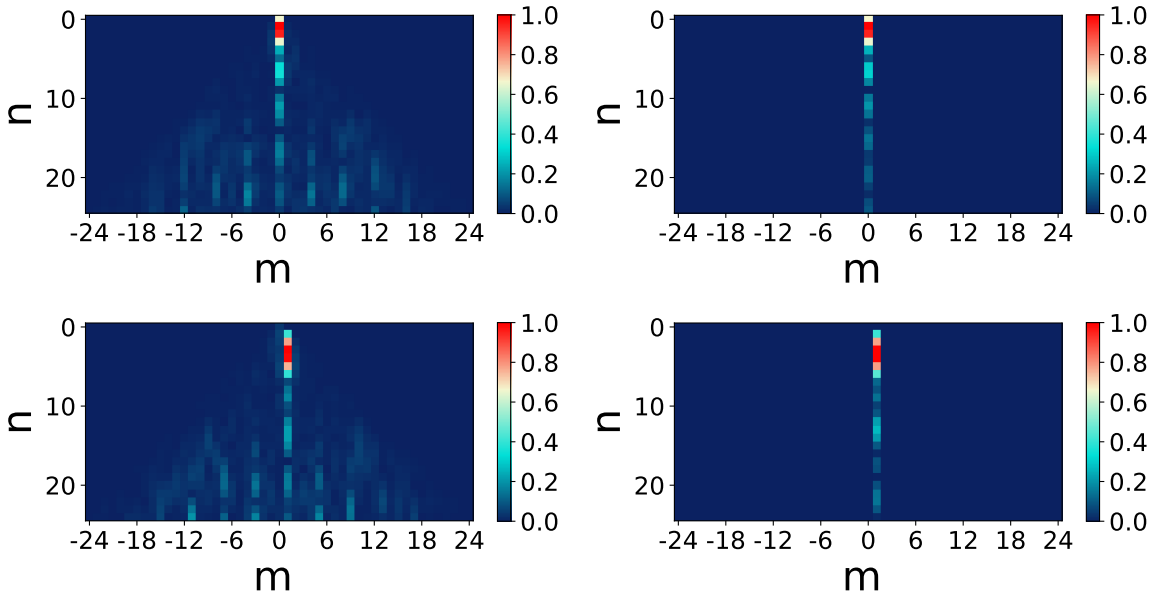

Figure 4.13: (Left) Normalized BSC obtained by the experimental measurement of the acoustic field using the angular spectrum method for a Gaussian beam with topological charge $m' = 0$ (Top), and a focused vortex beam with topological charge $m' = 1$ (Bottom); (Right) Theoretical BSC.

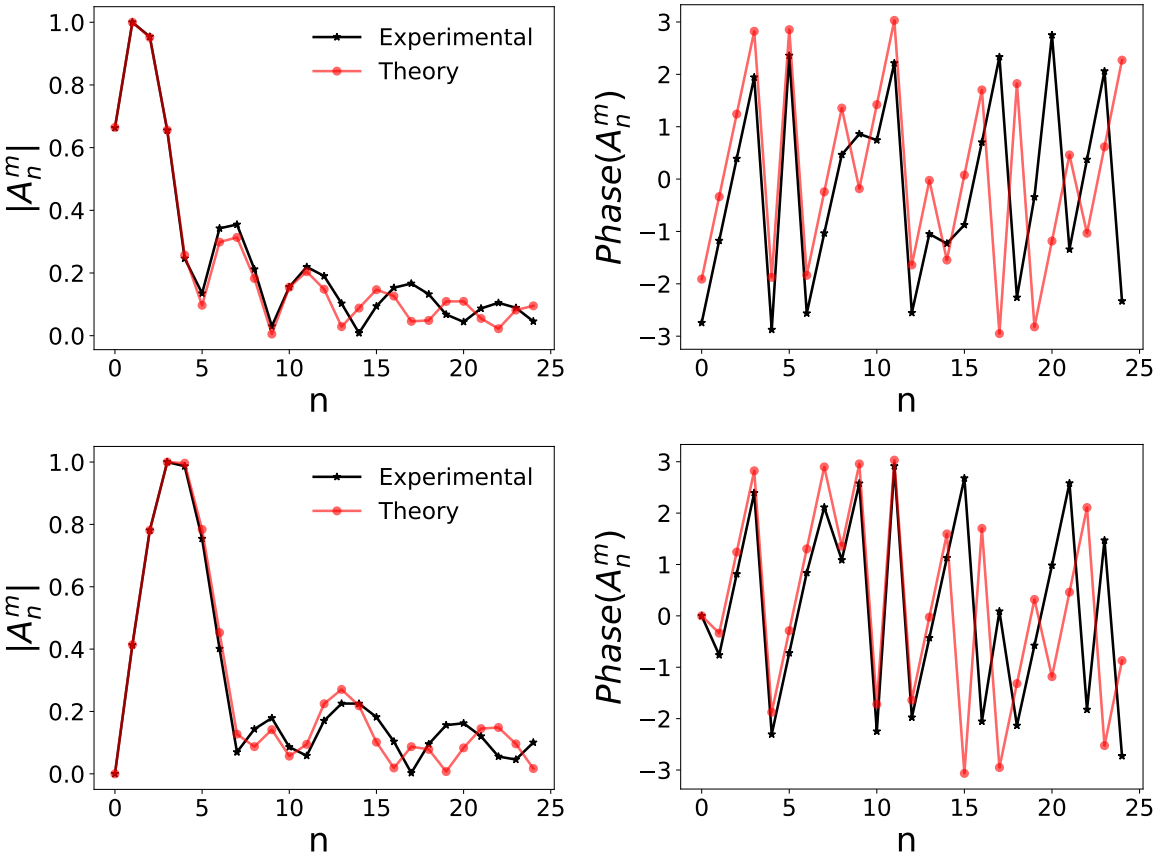

Figure 4.14: (Top) Normalized BSC in column $m = 0$ for a Gaussian beam with topological charge $m' = 0$ (Bottom), and BSC in column $m = 1$ for a focused vortex beam with topological charge $m' = 1$.

In the case of the spherical vortex beam (Fig. 4.15), the BSC in column $m = 1$ has notable differences from the theoretical ones. The maximum amplitude of the BSC shifts from $n = 8$ to $n = 9$, and the phase is also shifted. The radiation force is shown in Fig. 4.18. The radial force F_ρ of the synthetized field is rather faithful to the targeted field and a stiff radial trap is predicted. On the contrary, the axial forces F_z show large differences, mainly behind the focus as observed in Fig. 4.12. These errors are important enough to destroy the axial trap. Indeed, even if the axial force has a negative slope, it remains near zero and hence a bead located behind the focus is pushed away by the beam. The comparison between the experimental force estimations and the theoretical forces confirms that the distribution of 581 points on a disc at z= 0 allows us to retrieve the Gaussian beam and focused vortex beam well. However, it is not optimal for a spherical vortex beam with a bigger high-intensity ring. Compared to the first distribution, the second one operates much better for the focused vortex, although for

a spherical vortex the result is not satisfying yet. Nevertheless, this result indicates that by distributing the points in the focal plane and at the same time, increasing the number of points, we can ameliorate the inverse propagation operator. This inspired us to refine the mesh again and concentrate more on the region of the high-intensity ring of the vortex. In the following section, another distribution will be analyzed.

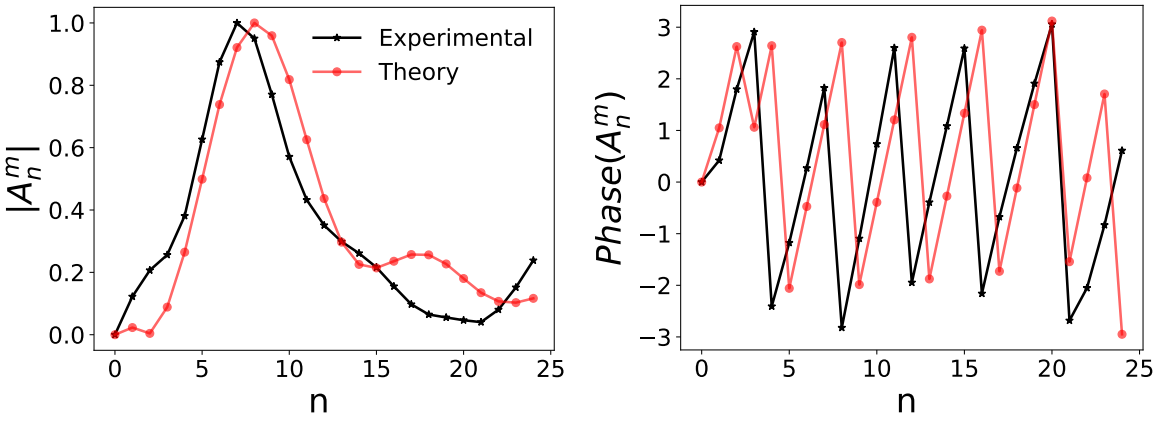

Figure 4.15: Normalized BSC in column $m = 1$ for a spherical vortex beam with topological charge $m' = 1$.

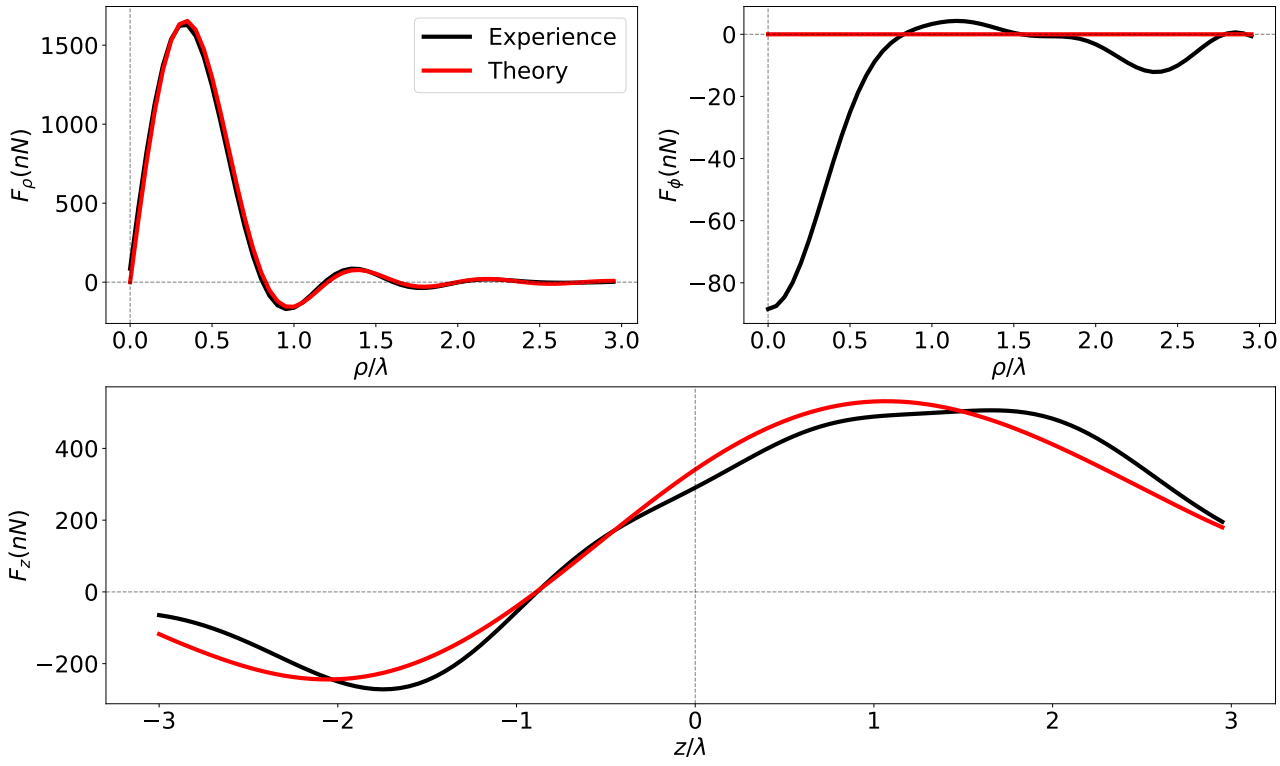

Figure 4.16: Radiation force exerted on a polystyrene sphere of radius $a = 0.1\lambda$ by a Gaussian beam of topological charge $m' = 0$.

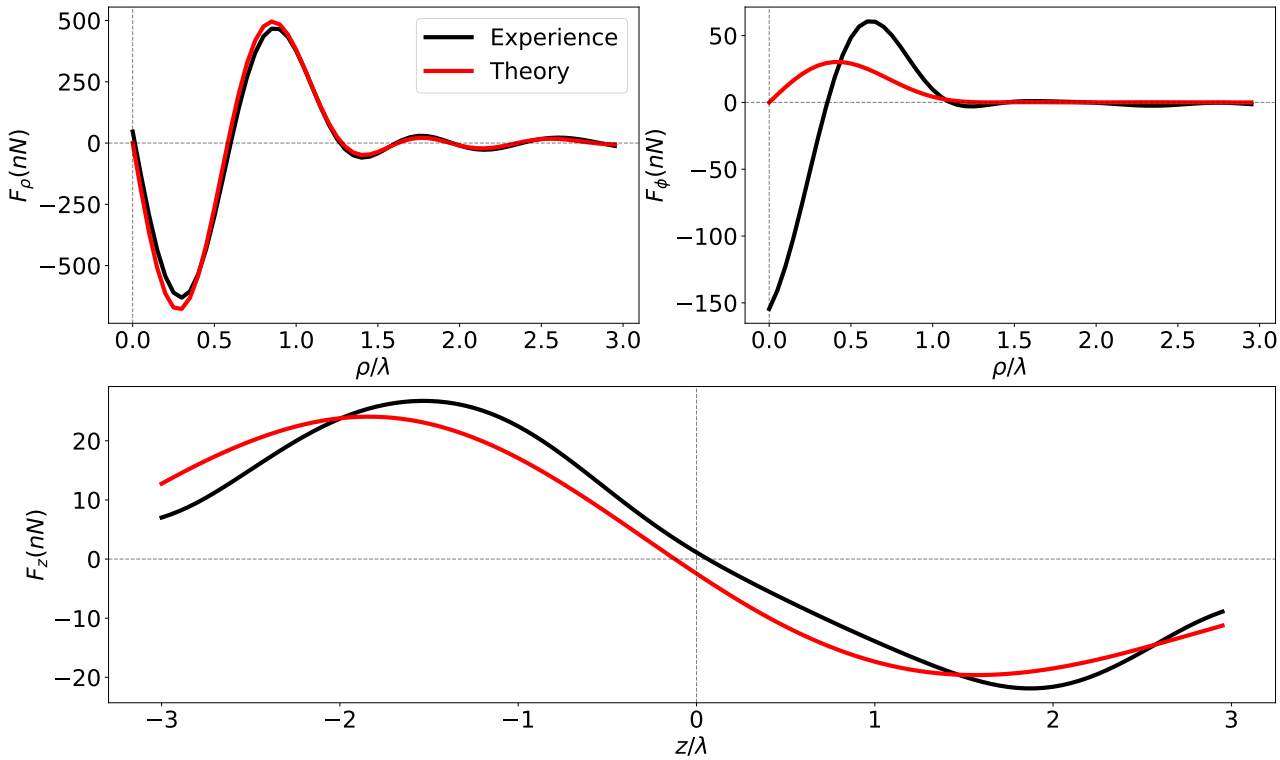

Figure 4.17: Radiation force exerted on a polystyrene sphere of radius $a = 0.1\lambda$ by a focused vortex beam of topological charge $m' = 1$.

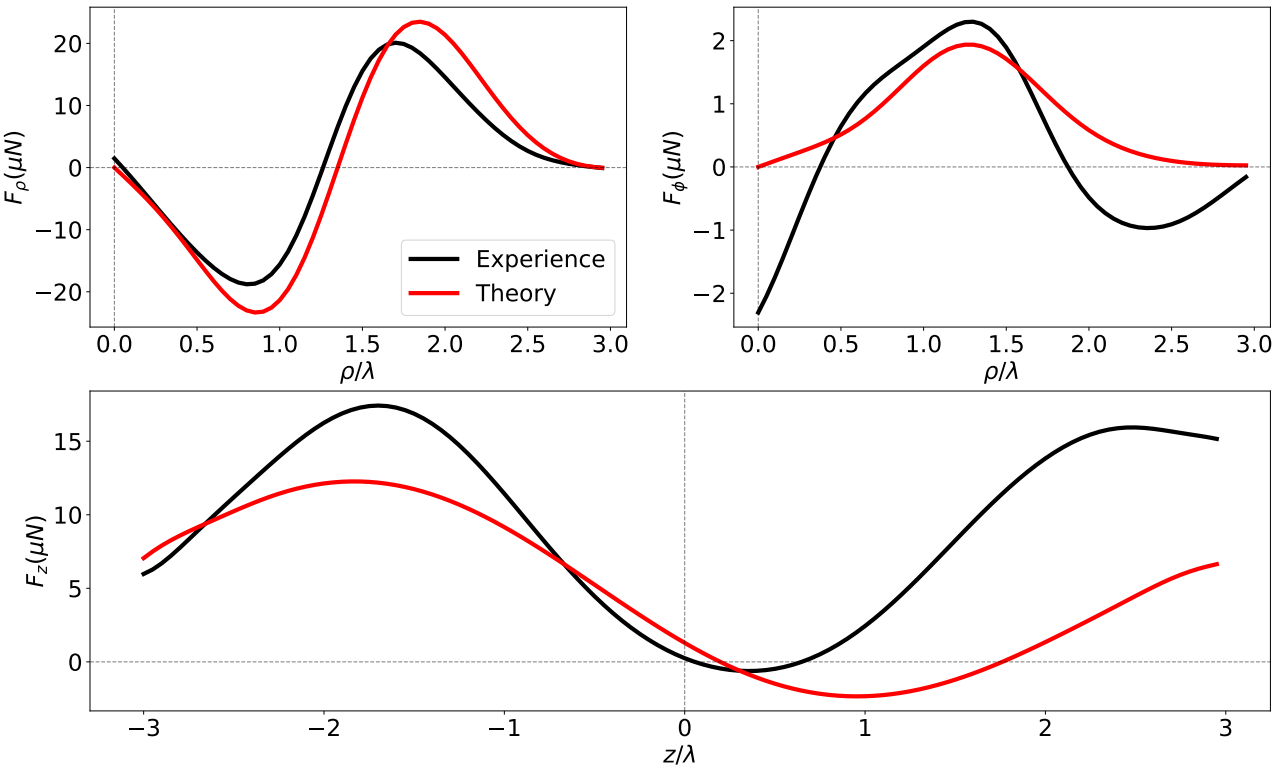

Figure 4.18: Radiation force exerted on a polyethylene sphere of radius $a = 0.45\lambda$ by a focused spherical vortex beam of topological charge $m' = 1$ and radial degree $l = 8$.

4.3.3 Synthesis of acoustic fields with a point distribution located on a square

In order to improve the quality of the synthesis for the spherical vortex beam, we employ another type of mesh in the focal plane (x, y). 2500 control points are distributed on a cartesian grid sampling a square disk of side length 6 mm. The principal interval in this mesh is 0.14 mm. Moreover, we refine the mesh at the center to retrieve the small circle of phase. Thus, the interval at the center is 0.1 mm, as shown in Fig. 4.19. The modulus (left column) and phase (right column) of the theoretical field of a spherical vortex beam in the new regular mesh (on the bottom) and the previous mesh (on the top), are shown in Fig. 4.20. Compared to the previous distribution, this one is much more refined in the center and focus sharply on the first high-intensity ring.

Considering that the mesh is much finer, the hydrophone used here is the smallest one with a diameter of 0.2 mm.

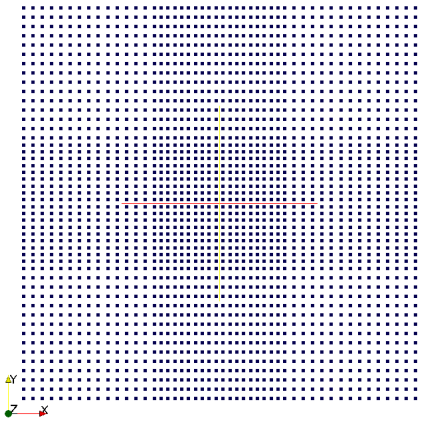

Figure 4.19: Distribution of control points on a disk of length 6 mm with 50×50 points.

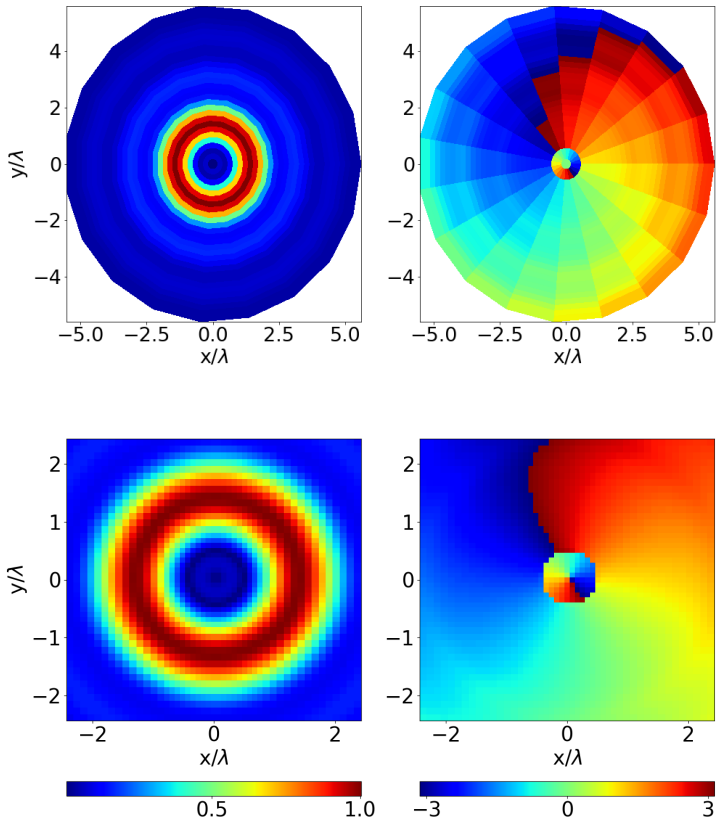

Figure 4.20: Modulus (normalized) and phases of the complex pressure field on plane (x, y) for a spherical vortex beam with $m' = 1$, $l = 8$ and $\alpha_0 = 42.5°$ sampled in different control meshes: (Top) mesh used in section 4.3.2; (Bottom) mesh used in this section.

Two types of acoustical beams are synthesized with this distribution: a focused vortex beam and a spherical vortex beam. These fields are scanned in planes (x, y) and (x, z), and their modulus and phases are plotted in the following figures.

For a spherical vortex $m' = 1$, $l = 8$ and $\alpha_0 = 49°$, (Fig. 4.22 and Fig. 4.23), we find that the high-intensity ring is well recovered with good homogeneity of amplitude. Inside the ring, the field is at zero amplitude , the same as the theoretical one. Even though the variation of phase inside the small circle does not appear in the measurement field, the global variation of the phase is in good agreement with the theoretical one. The modulus in plane (x, z) is similar to the theory as expected. The radiation forces estimated with the measurement are given in Fig. 4.24. Compared to Fig. 4.18 in the previous section, we find a better agreement with the theoretical forces, especially for the axial force F_z which confirms that the spherical vortex is well synthesized and this kind of control point distribution works out for the desired spherical vortex. Since the synthesis was now faithful to the target fields, the angle has been increased from $\alpha_0 = 42.5°$ to $\alpha_0 = 49°$ in order to stiffen the trap and increase the radiation force exerted. With this modification, the amplitude of the radiation force is one order of magnitude larger here than in the previous section.

The results for a focused vortex of topological charge $m' = 1$ and $\alpha_0 = 49°$ are shown in Fig. 4.25. Both the modulus and phase correspond well with the theoretical field. The BSC of the experimental spherical vortex are given in Fig. 4.21. Compared to the BSC obtained in the previous section Fig. 4.15, the result is improved. Both the modulus and phase agree well with the theoretical BSC. Nonetheless, as we calculate the radiation forces in Fig. 4.26, we notice that the axial force does not agree as well as for the previous distribution (Fig. 4.17) and the decay of the equilibrium position becomes larger. So, for a focused vortex of topological charge $m' = 1$, this kind of fine mesh has no advantage compared to the previous one. And if we compare the number of points, in this distribution 2500 points are used which is 4 times larger than the previous distribution. Furthermore, in the experimental measurement, acquisition time for each point takes around 20 s. The 2500 points mesh costs 10 hours more for the measurement, which is not efficient for a simple focused vortex. Therefore, for the Gaussian and focused vortex beam with a small high-intensity region, the second distribution in a 7 mm disc of 581 points is optimal. Whereas for a spherical vortex with a larger intensity ring, the 2500 points mesh is better.

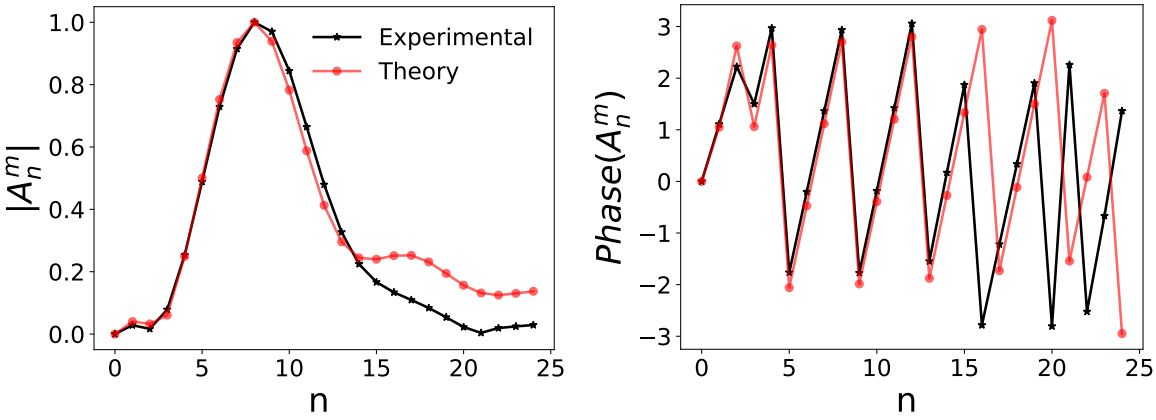

Figure 4.21: Normalized BSC in column $m = 1$ for a spherical vortex beam with topological charge $m' = 1$ and l =8.

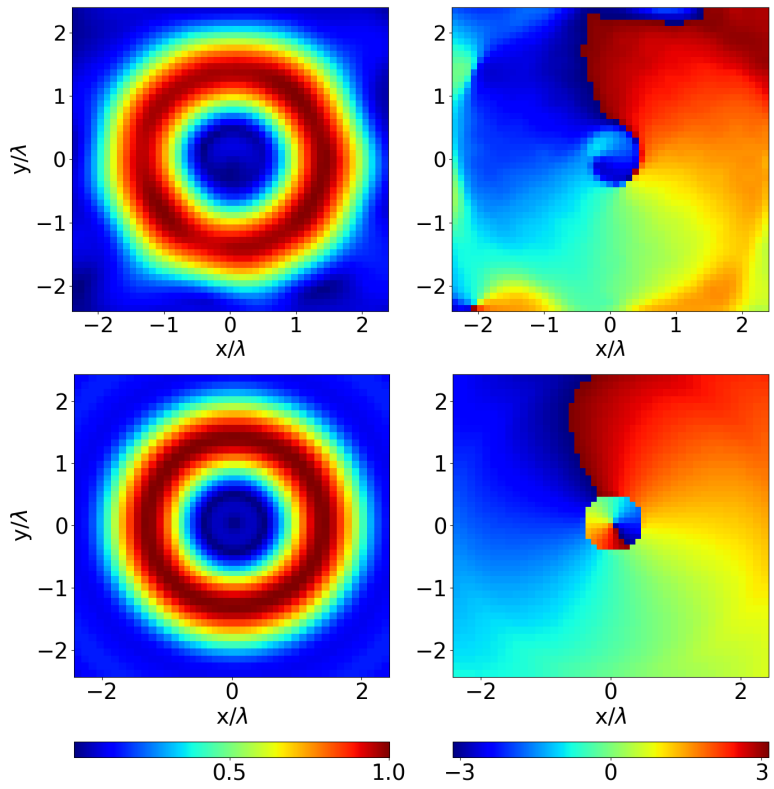

Figure 4.22: Modulus (normalized) and phases of the complex pressure field in plane (x, y) for a spherical vortex beam with $m' = 1$, $l = 8$ and $\alpha_0 = 49°$: (Top) experimental measurements; (Bottom) theoretical pressure field.

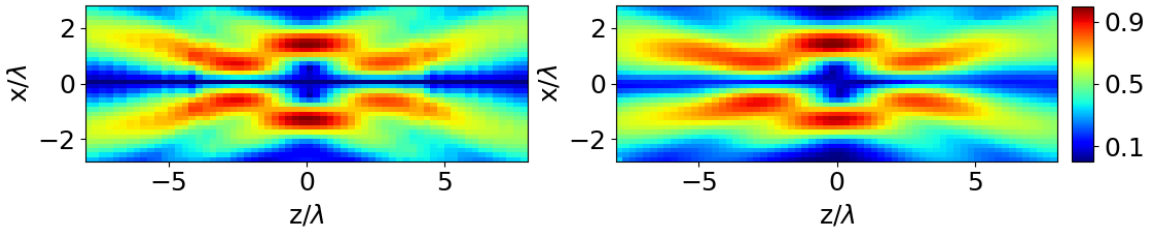

Figure 4.23: Modulus (normalized) of the complex pressure field in plane (x, z) for a spherical vortex beam with $m' = 1$, $l = 8$ and $\alpha_0 = 49°$: (Left) theoretical pressure field; (Right) experimental measurements.

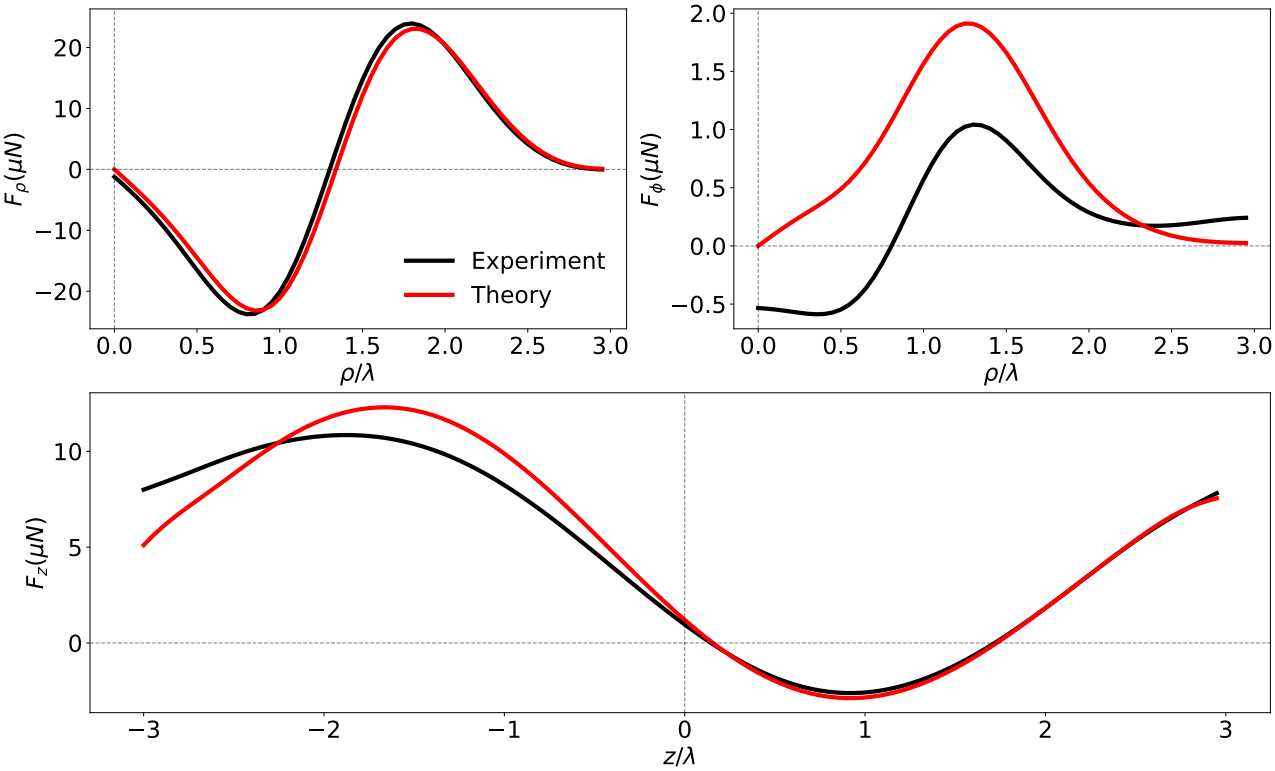

Figure 4.24: Radiation force exerted on a polyethylene sphere of radius $r = 0.45\lambda$ by a spherical vortex beam with $m' = 1$, $l = 8$ and $\alpha_0 = 49°$.

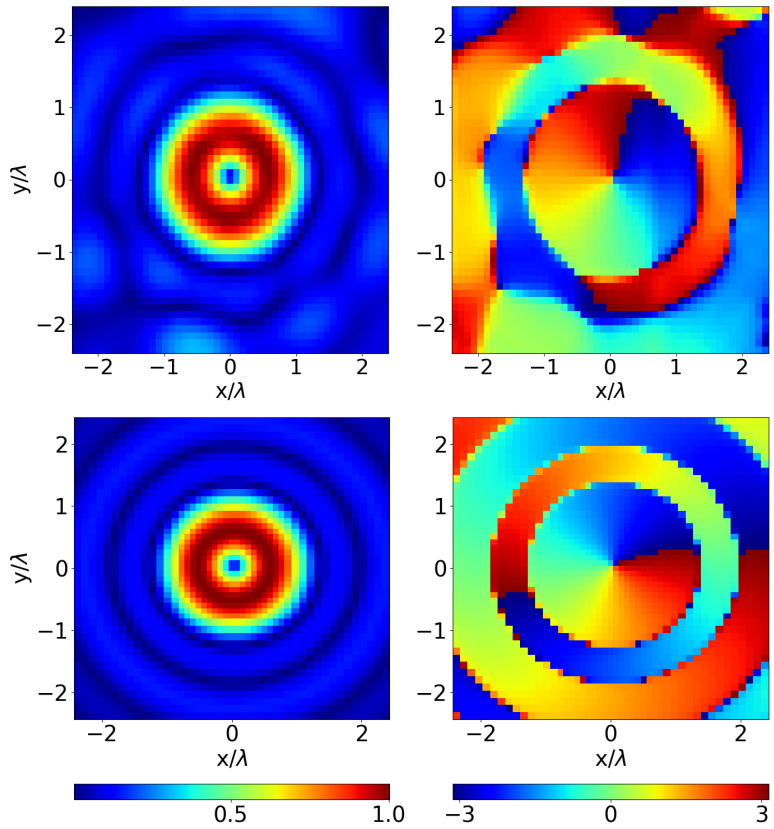

Figure 4.25: Modulus (normalized) and phases of the complex pressure field in plane (x, y) for a focused vortex beam of topological charge $m' = 1$ and $\alpha_0 = 49°$: (Top) experimental measurements; (Bottom) theoretical pressure field.

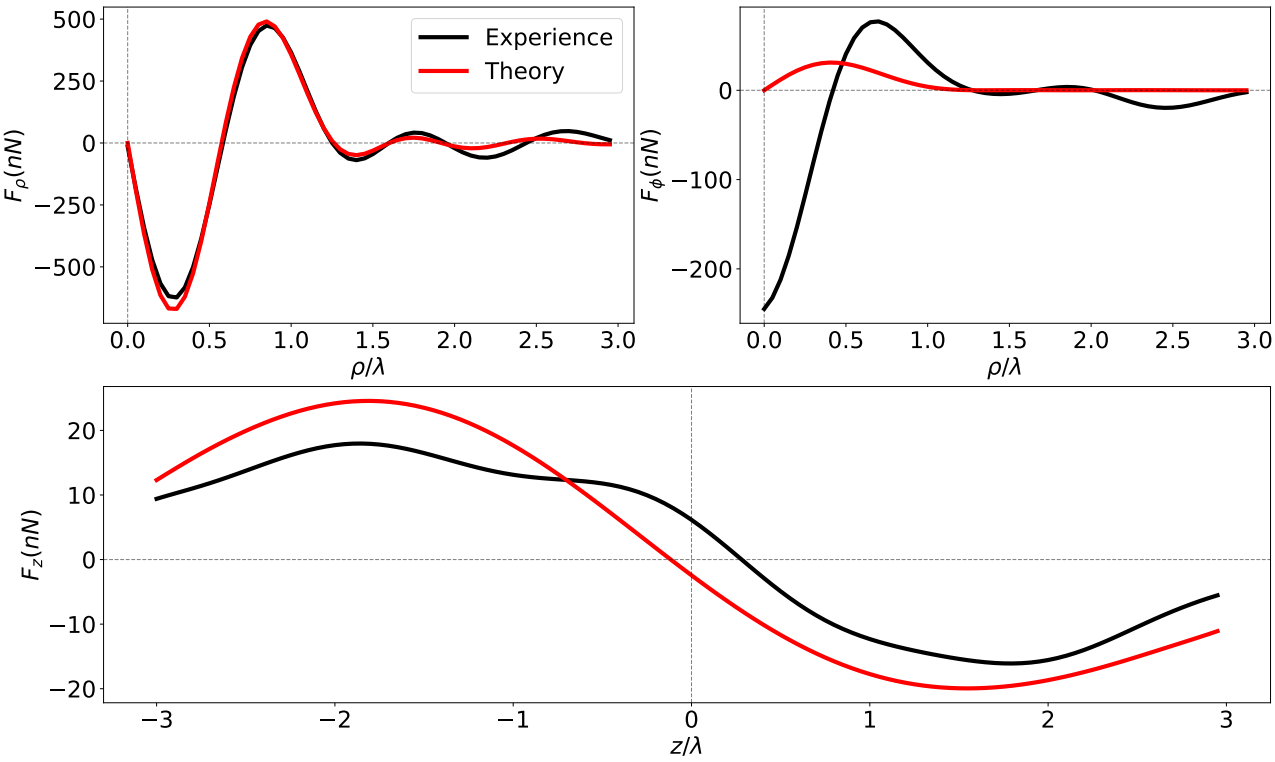

Figure 4.26: Radiation force exerted on a polystyrene sphere of radius $r = 0.1\lambda$ by a focused vortex beam of topological charge $m' = 1$ and $\alpha_0 = 49°$.

4.3.4 Comparison of the three distributions

In the previous section, we have recorded experimentally the three propagation operators ($\underline{\underline{H}}_1$, $\underline{\underline{H}}_2$, $\underline{\underline{H}}_3$) corresponding to the three control point mesh assessed. Then we computed their regularized pseudo-inverse ($\hat{\underline{\underline{H}}}_1^{-1}$, $\hat{\underline{\underline{H}}}_2^{-1}$, $\hat{\underline{\underline{H}}}_3^{-1}$). For all these distributions, a focused vortex beam was synthesized by the inverse filter technique. The experimental measurement of the acoustical fields synthesized showed some differences between the three distributions. In this section, we try to find where these differences come from.

Firstly, a focused vortex beam $\underline{f}^{fv}(t)$, is synthesized by the three different emission vectors ($\underline{e}_1^{fv}(t)$, $\underline{e}_2^{fv}(t)$, $\underline{e}_3^{fv}(t)$) calculated by each distribution. We begin by a comparison of these vectors. In Fig. 4.27, the set of electric emitted signals normalized to 1 as a function of time is presented. From the figure, we find that the distribution of emitted signals is different between the three; the transducers which have high emission amplitude are not the same ones. To have a more accurate comparison, we then plot the modulus and phase of each transducer at frequency 1.2 MHz in Fig. 4.28. We find no similarity between the three. Even the $\underline{E}_2^{fv}(\omega)$ and

$\underline{E}_3^{fv}(\omega)$ for which the experimental measurement in plane (x, y) is in good agreement with the theoretical field. Therefore, to synthesize a given field we can have different solutions for the transducer array.

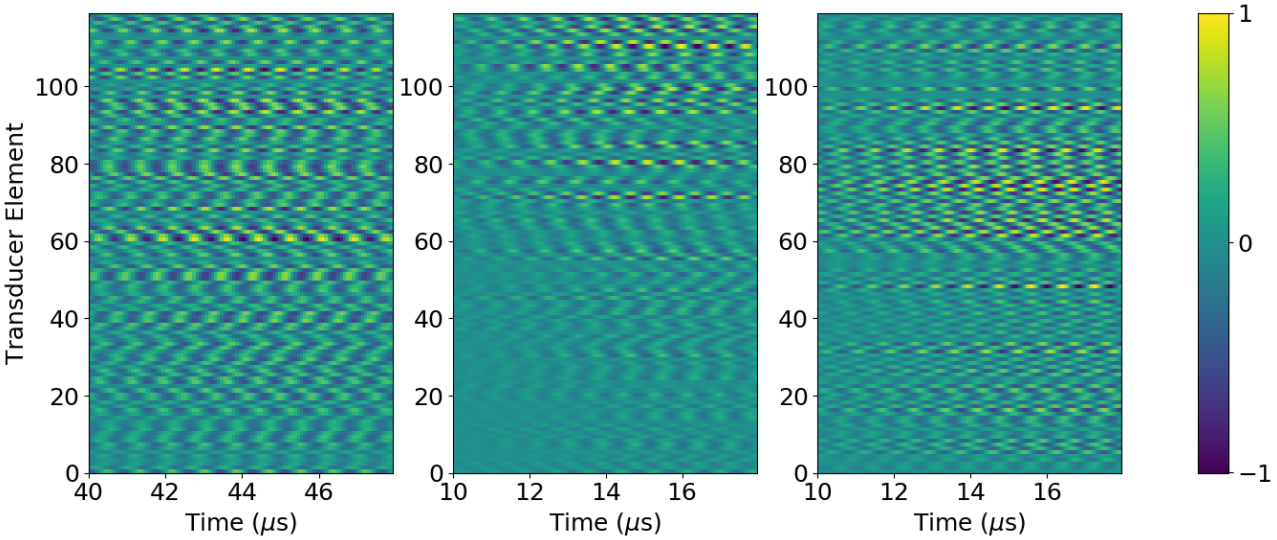

Figure 4.27: Emission vectors for a focused vortex beam calculated by three different distributions of control points ($\underline{e}_1^{fv}(t)$, $\underline{e}_2^{fv}(t)$, $\underline{e}_3^{fv}(t)$).

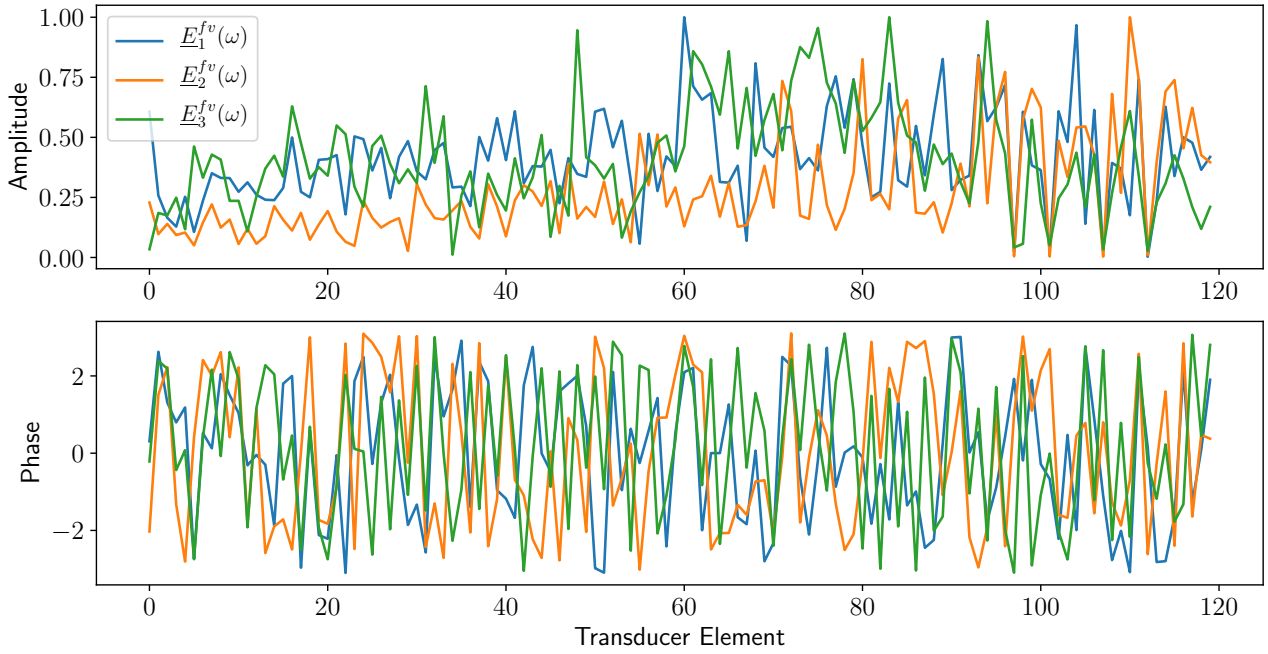

Figure 4.28: Amplitude and phase of the signals emitted by the array of transducers.

Since the record of the propagation operator is done in almost the same experimental conditions, two major factors can lead to these differences: the distribution of control points,

and the threshold regularization, i.e the cut-off value, while using the SVD method to get the pseudo-inverse matrix. So in the next parts, we will analyze these two factors.

The normalized singular values of three distributions ($\underline{SV}_1(\omega)$, $\underline{SV}_2(\omega)$, $\underline{SV}_3(\omega)$) are presented in the figure below (Fig. 4.29). On the top row from left to right, all the singular values of the three distributions are plotted as a function of frequency. On the bottom, the singular values at frequencies 0.5 MHz, 1.2 MHz and 2 MHz are presented after sorting them in amplitude order.

For all measurements, the dynamic range is about -66 dB. The oscilloscope we used has a resolution of 8 bits which can encode an analog input into 256 different levels ($2^8 = 256$). While calculating the singular values, the absolute value is taken into account which requires only 7 bits of resolution. For each record, 16 averages were taken in order to improve the SNR which adds $\sqrt{16} = 4$ bits of resolution to the dynamic range. Thus the total resolution is 11 bits which leads to a dynamic range of -66 dB (a factor 2 is equal to 6 dB).

In the first distribution (Lebedev) the singular values $\underline{SV}_1(\omega)$, as depicted in Fig. 4.29, remain above -30 dB, well above the dynamic range. They have almost no noise and the singular values decrease almost monotonically. On the whole bandwidth there is no grouping of singular values with similar and weak amplitude. As the distance between grid points in this distribution is the largest, the signal recorded is not likely to be similar from one to another, the column vectors of the matrix are uncorrelated, and hence the matrix is full rank. Note that due to the presence of noise, the matrix is always full rank whatever the dimension, i.e the number of points in the distribution. However, singular values grouping at noise level or if the SNR is too high at the dynamic range level signifies that the mesh is fine enough to perform oversampling. This feature is expected for inverse problems that are usually ill-posed and the solution is regularization as seen above.

In the second distribution, the weakest singular values reach the dynamic range level of about -66 dB. At low frequencies and high frequencies where the signal amplitude is smaller due to the finite bandwidth of the transducer array and the frequency content of the signal emitted. The bandwidth selected is larger than in the previous distribution. Again, the singular values are not contaminated by noise as above. However,the mesh grid performs oversampling for frequencies below 0.8 MHz since a group of crowded weak singular values appears. The sampling rate is relative to the wavelength. This behavior disappears at higher frequencies

where the undersampling is reached, and the matrix would be of full rank even in noiseless condition. So we can conclude that at 1.2 MHz, this mesh grid is not fine enough to sample all the physically feasible pressure fields.

In the third distribution, the hydrophone was changed from 1 mm to 0.2 mm. Since the sensitivity is proportional to the sensor surface, a −28 dB decrease of the SNR is expected. Oversampling at low frequencies leads to some of the singular values grouping together at about −43 dB. The SNR level is now above the theoretical dynamic range and reduces it from −66 dB to −43 dB. It is noticed that the undersampling now reaches at around 1.3 MHz which is above our frequency of interest. It ensures that optimal conditions are met to synthesize all target pressure fields.

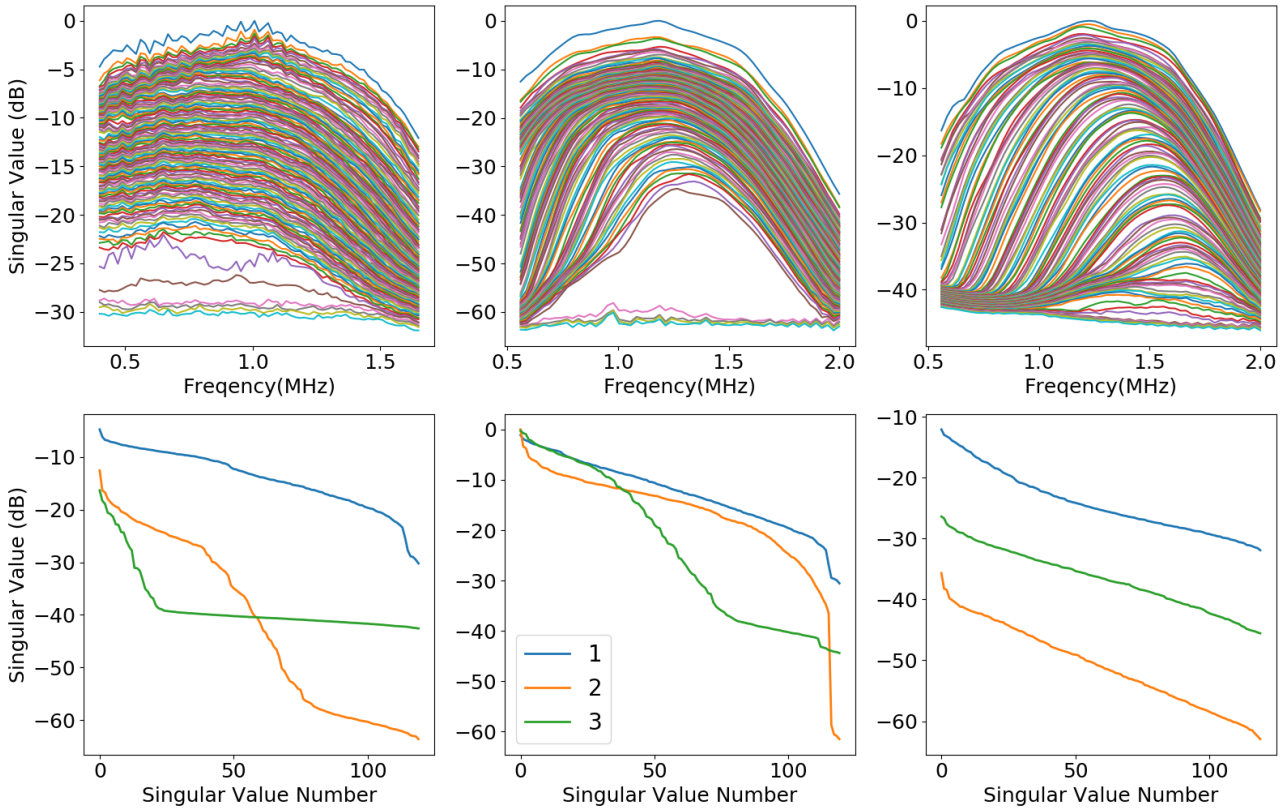

Figure 4.29: Singular Values : (Top) all the singular values for the three distributions (1. Lebedev; 2. (θ, r) disc; 3. Square mesh); (Bottom) singular values at 0.5 MHz, 1.2 MHz and 2 MHz (from left to right).

Influence of the SVD regularization

The cut-off value used in the regularization step may affect the final result. This regularization step is required for the over-determined linear system often encountered in the inverse

problems. We analyzed above that only $\underline{\underline{H}}_3(\omega)$ is both overdetermined and with a dynamic range fixed by the SNR. So we take the example of $\underline{SV}_3(\omega)$to analyze the influence of the cut-off value. Figure 4.30 shows the different cut-off values we have tried and their influences on the field synthesis. On top of the figure, the theoretical field is presented. Then by successively increasing the number of singular values taken into account, three different estimates of the pseudo-inverse matrix $\hat{\underline{\underline{H}}}_3^{-1}(\omega)$ are calculated. This leads to three different emission vectors $\underline{E}_3^{sv1}(\omega)$, $\underline{E}_3^{sv2}(\omega)$ and $\underline{E}_3^{sv3}(\omega)$ for the same target field, $\underline{F}_3^{sv}(\omega)$.

To get the experimental pressure field we use a different method. A propagation operator $\underline{\underline{H}}_4(\omega)$, with 3600 control points distributed evenly through a square of 14 mm×14 mm ($11.6\lambda \times 11.6\lambda$) at the focal plane was recorded. For any emission vector $\underline{E}(\omega)$ the pressure field scanned on these 3600 points is given, at angular frequency ω, by $\underline{\underline{H}}_4(\omega)\underline{E}(\omega)$.

With this method we obtain the synthesized field in the focal plane. As illustrated in Fig. 4.30, the more singular values we take the more information on the field we retain. Taking only the first 30 singular values, the high-intensity red ring and the phase inside the ring are well retrieved. Meanwhile, the blue ring illustrated in the theoretical field outside the red ring disappears in this case. As we cut off at the 30^{th} singular value we eliminate the necessary information in the inverse matrix to retrieve the blue ring. Then by doubling the number of singular values, the blue ring appears and the amplitude and phase compared to the previous one is much closer to the desired field. This improvement indicates that the information to synthesize the field is more complete in this regularization. In the last test, all the singular values were used in the inversion. Both the red and blue ring is similar to the theoretical one. While outside, some noise appears in the field amplitude and phase. This phenomena demonstrates that in the $\underline{SV}_3(\omega)$ the noise is very limited, and only impacts the outside of the main intensity ring. From the regularization procedure above we find that, even in the case with more noise, the cut-off value doesn't have a great influence on the final synthesis of the field.

The emission vectors ($\underline{E}_3^{sv1}(\omega)$, $\underline{E}_3^{sv2}(\omega)$, $\underline{E}_3^{sv3}(\omega)$) computed by the inverse matrix with different cut-off values (cut-off at the 30^{th}, 60^{th} and 120^{th} value respectively) are depicted in Fig. 4.32. For the emission vector $\underline{E}_3^{sv1}(\omega)$ the largest amplitudes are at the center of the transducer array from the 30^{th} to 90^{th} transducers. Then by increasing the number of singular values, $\underline{E}_3^{sv2}(\omega)$, the emission intensity becomes more evenly distributed. Eventually, taking all

the singular values $\underline{E}_3^{sv3}(\omega)$, the emission distribution becomes less uniform. The amplitudes and phases of the emission vectors are represented in Fig. 4.33. As interpreted previously, the amplitudes between the three don't show many similarities. In spite of that, the phases are very close which gives a reason for the similarity of the wavefield in Fig. 4.30. Regarding its influence on the radiation force as depicted in Fig. 4.31, the radial and axial forces exerted by the spherical vortex with different cut-off values are similar and close to the theoretical force. The radial force with cut-off value at 30^{th} has a larger amplitude than the others owing to the higher amplitude of the emission vector shown in Fig. 4.32. Besides, its azimuthal force, compared to those with higher cut-off values has a more significant difference from the theoretical one. However, as the magnitude of F_ϕ is small this difference is not noteworthy. We also observe that the forces exerted by vortex with cut-off value at the 60^{th} almost superimpose with the 120^{th}. Consequently, the regularization of the cut-off value in the inverse filter technique doesn't have a crucial influence on the field synthesis quality.

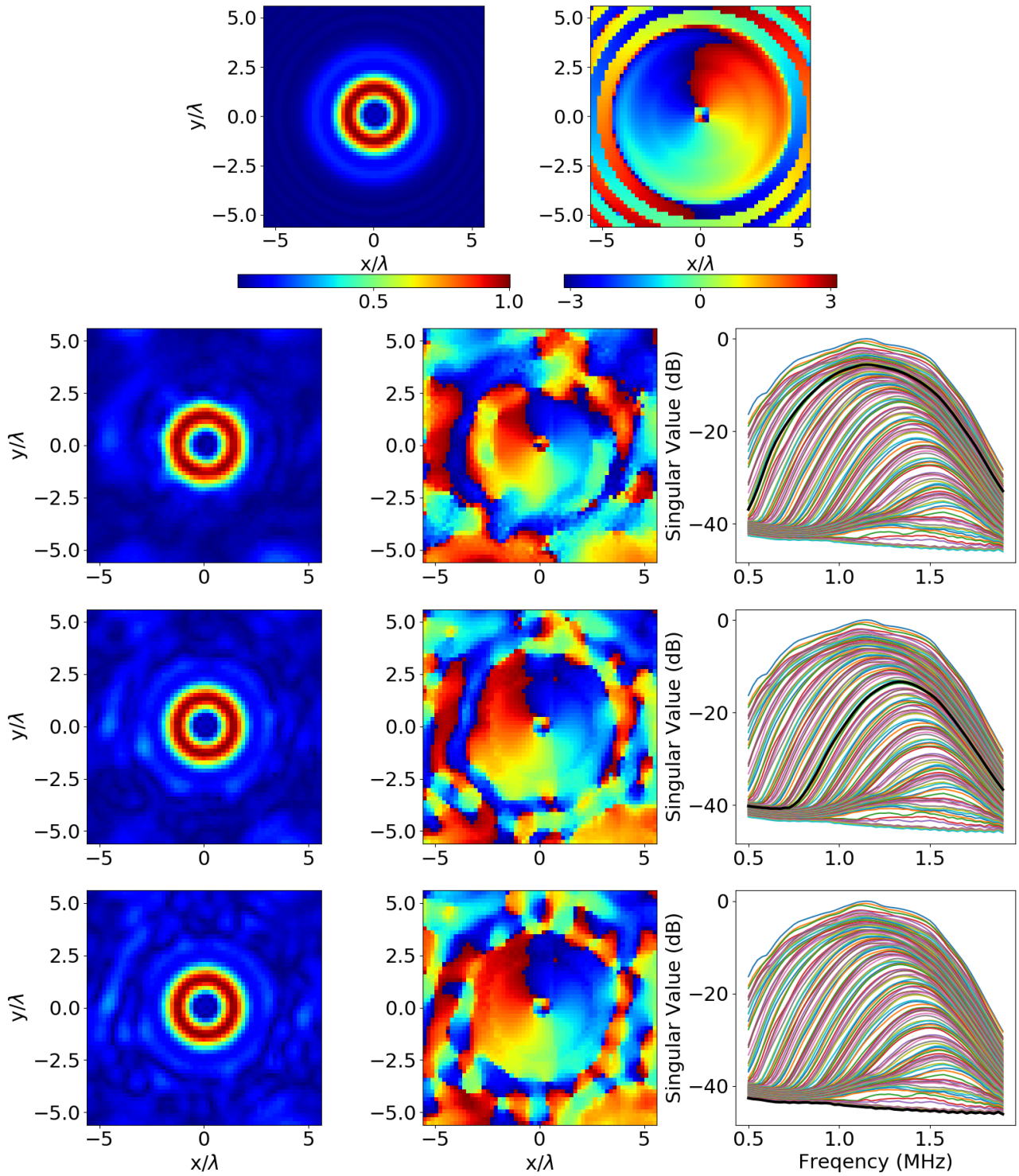

Figure 4.30: Influence of singular values : (Top) the theoretical modulus and phase of pressure field; (Bottom) modulus and phase obtained by taking different cut-off thresholds for the singular values.

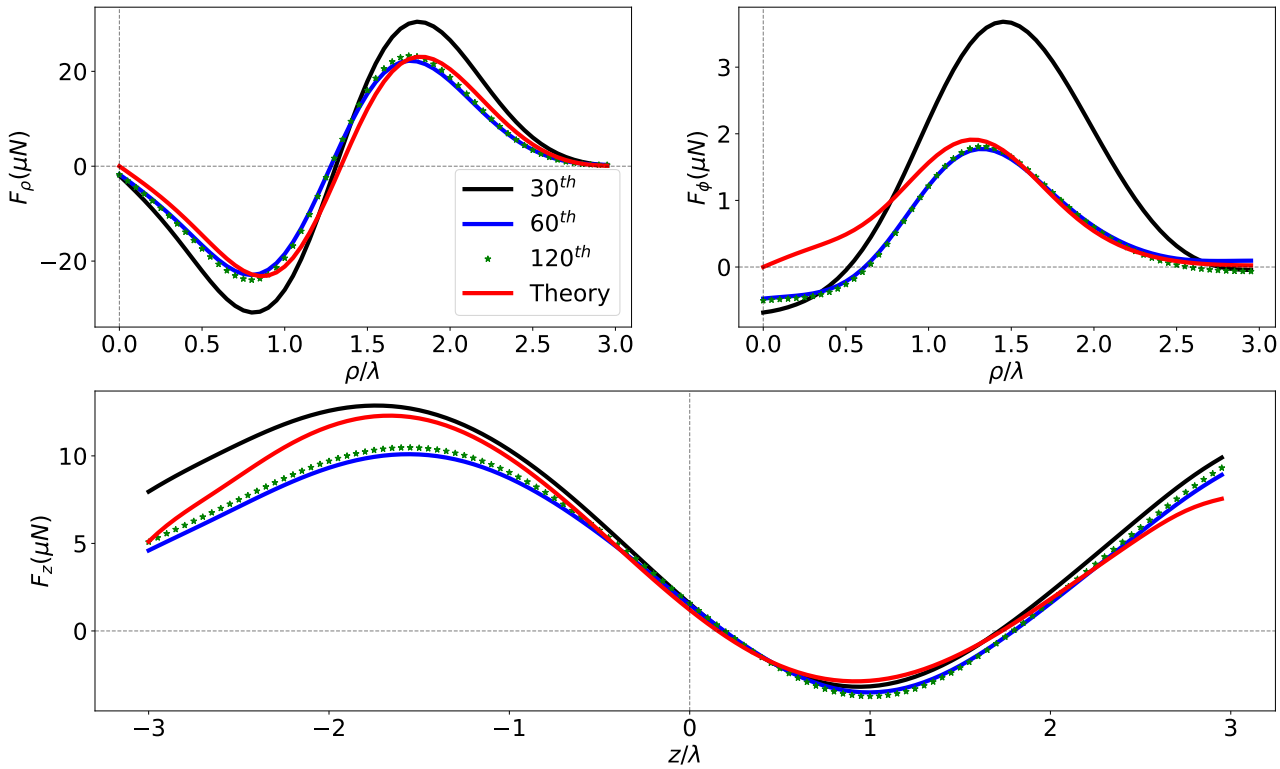

Figure 4.31: Radiation force exerted on a polyethylene sphere of radius a = 0.45λ by spherical vortex synthesized by applying different cut-off values (cut-off at the 30^{th}, 60^{th}, 120^{th} value).

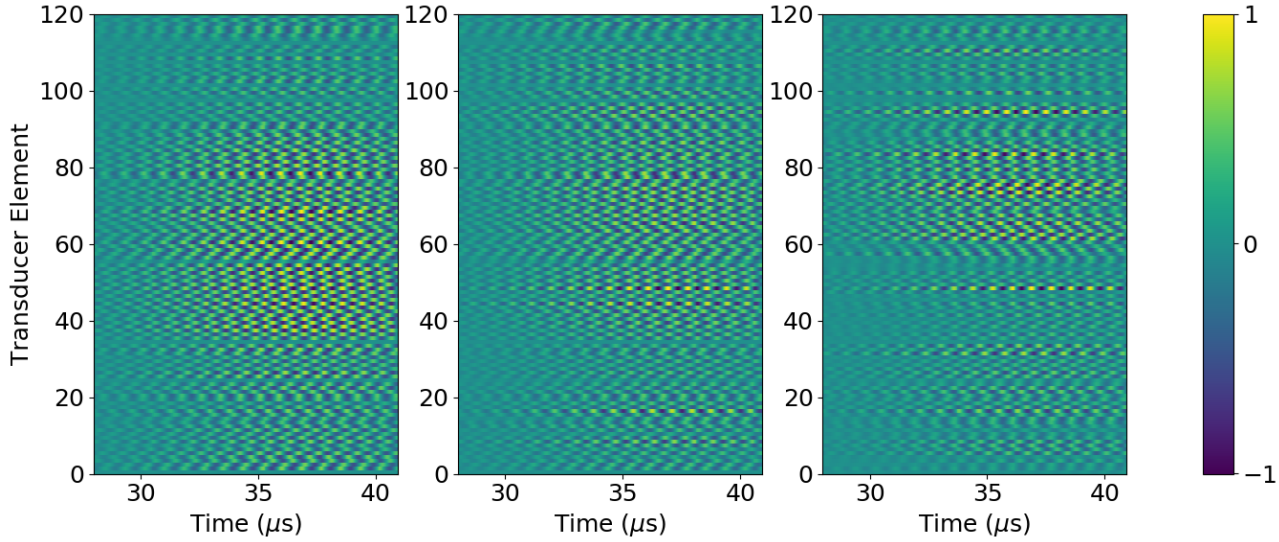

Figure 4.32: The emission vectors ($\underline{E}_3^{sv1}(\omega)$, $\underline{E}_3^{sv2}(\omega)$, $\underline{E}_3^{sv3}(\omega)$) computed by the inverse matrix with different cut-off values (cut-off at the 30^{th}, 60^{th}, 120^{th} value).

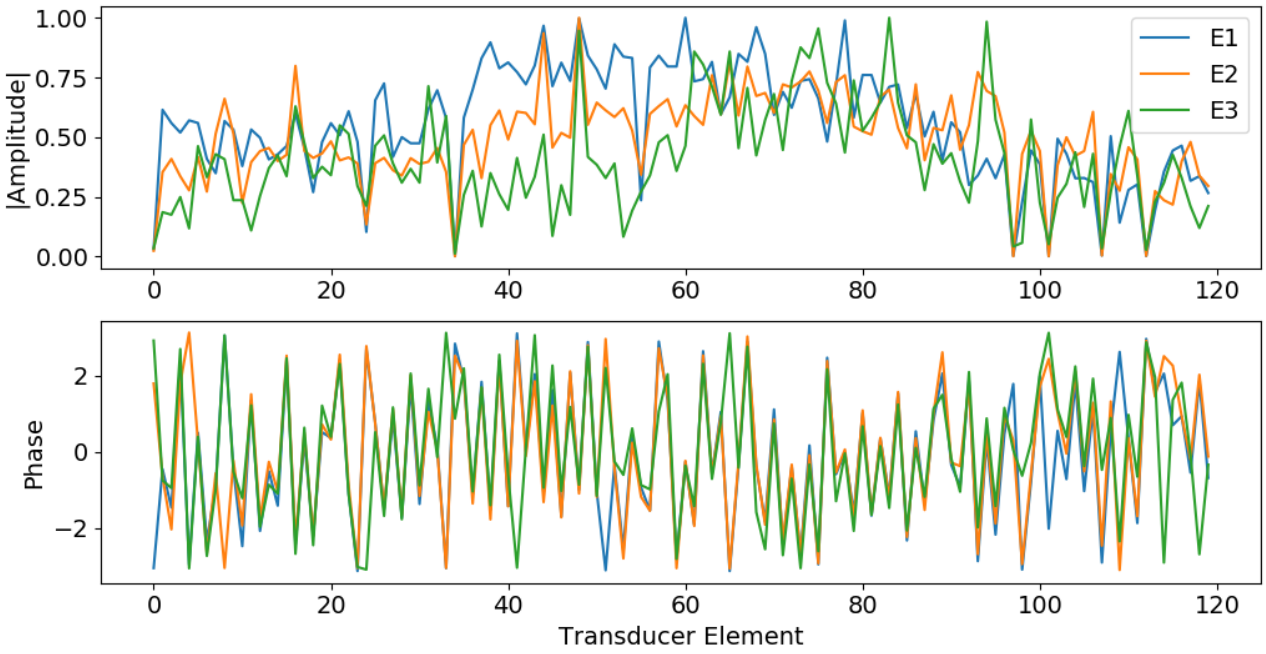

Figure 4.33: Influence of singular values cut-off threshold on the amplitude and phase of the emission vectors ($\underline{E}_3^{sv1}(\omega)$, $\underline{E}_3^{sv2}(\omega)$, $\underline{E}_3^{sv3}(\omega)$).

Influence of the propagation operator

Knowing that the regularization of singular values doesn't have a remarkable impact on the field synthesis, the reason for the difference in the scanned field is, therefore, hidden in the propagation operator $\underline{\underline{H}}(\omega)$ itself. To investigate this we apply first the propagation operator $\underline{\underline{H}}_4(\omega)$ to the different emission vectors. Second, the operator $\underline{\underline{H}}_2(\omega)$ will be used to confirm the role played by the image space of each matrix.

Projection of the emission vector in the image space of the matrix $\underline{\underline{H}}_4(\omega)$

Firstly, we compare the pressure fields obtained in the focal plane in the same conditions for the emission vectors $\underline{E}_1^{fv}(\omega)$, $\underline{E}_2^{fv}(\omega)$ and $\underline{E}_3^{fv}(\omega)$ obtained for a focused vortex of charge $m' = 1$. As described above (Eq. (4.3)), the pressure field can be directly determined by multiplying the emission vector with the matrix $\underline{\underline{H}}_4(\omega)$. The results are shown in Fig. 4.34, modulus on the left column and phase on the right. The target field is displayed on the last row.

The pressure field $\underline{\underline{H}}_4(\omega)\underline{E}_1^{fv}(\omega)$ at the top of the figure describes a ring of non-uniform amplitude with a shift towards y-axis.

The pressure field $\underline{\underline{H}}_4(\omega)\underline{E}_2^{fv}(\omega)$ is much closer to the target pattern but shifted along the x-axis. The main intensity ring is still non-uniform; the second intensity ring, in blue, is non-uniform as well. Intensity spots regularly spaced on a circle of larger radius are a salient feature that was already visible on the scan in Fig. 4.11(a). The control point distribution used to compute $\underline{E}_2^{fv}(\omega)$ (Fig. 4.10), is evenly distributed on polar coordinates (θ,r). When r increases, the distance between two points located at the same radius increase as well. This leads to an undersampling responsible, probably through aliasing, for the generation of topological charge components of opposite sign and hence a cosine modulation on the azimuth.

The pressure field $\underline{\underline{H}}_4(\omega)\underline{E}_3^{fv}(\omega)$, as illustrated in the figure, is well centered and the amplitude and phase are in good match with the theoretical pattern up to the third ring. Farther away, the field becomes random. Since $\underline{E}_3^{fv}(\omega)$ is calculated with a matrix $\underline{\underline{H}}_3^{-1}(\omega)$ and a target field $\underline{F}_3^{fv}(\omega)$ defined on a square mesh of size $7\,\mathrm{mm}\times7\,\mathrm{mm}$ ($5.8\lambda \times 5.8\lambda$) the field was not constrained outside the third ring and hence it is not surprising that discrepancies occur.

The synthesis of spherical vortices is now investigated. As the use of the first emission vector ($\underline{E}_1^{sv}$) gives poor results for the focused vortex, only the second and third emission vectors are considered: $\underline{E}_2^{sv}$ and $\underline{E}_3^{sv}$. The corresponding pressure fields are shown in Fig. 4.35. The pressure field obtained with $\underline{\underline{H}}_4(\omega)\underline{E}_2^{sv}$ on top of the figure shows an inhomogeneous intensity ring with a non-zero amplitude region inside. It is consistent with the experimental result presented in Fig. 4.11(a). As for the focused vortex synthesis some high-intensity noise appears at the edge of the field. Meanwhile, the field is also slightly shifted towards the x-axis. On the contrary, the pressure field $\underline{\underline{H}}_4(\omega)\underline{E}_3^{sv}$, as expected, has almost the same pattern as the theoretical one.

Projection of the emission vector in the image space of the matrix $\underline{\underline{H}}_2(\omega)$

The same analysis is done to visualize the pressure field in the control plane of the second distribution. As depicted in Fig. 4.36, the $\underline{\underline{H}}_2(\omega)$ is applied to the emission vectors (top row: $\underline{E}_2^{sv}$; middle row: $\underline{E}_3^{sv}$, bottom: target field). The pressure field $\underline{\underline{H}}_2(\omega)\underline{E}_2^{sv}$ has a perfect homogeneous ring centered at the origin of the mesh with zero amplitude inside. This contrasts with Figs. 4.35 and 4.11(a) where the noise outside the high-intensity ring disappears. While looking at the pressure field $\underline{\underline{H}}_2(\omega)\underline{E}_3^{sv}$ the high-intensity ring is shifted towards x-axis in a negative direction. This is the opposite of $\underline{\underline{H}}_4(\omega)\underline{E}_2^{sv}$ and confirms that the two experimentally

determined lens focal points, that are used as origin, are slightly shifted in the two experiments. However, as observed previously, the highest intensity ring as well as secondary lobe are uniform. The fact that discrepancies are visible in the experimental scan or in the linear mapping operated by $\underline{\underline{H}}_4(\omega)$, i.e $\underline{\underline{H}}_4(\omega)\underline{E}_2^{sv}$, but not in the linear mapping operated by $\underline{\underline{H}}_2(\omega)$ confirms the undersampling or, in other words, the too small dimension of the image subspace of $\underline{\underline{H}}_2(\omega)$. The number of rows of $\underline{\underline{H}}_2(\omega)$, the image space dimension, is too small to distinguish the two emission vectors. To synthesize a spherical vortex the propagation operator $\underline{\underline{H}}_2(\omega)$ is not adequate. The control points are not enough. Thus, some of the necessary information to retrieve the field is left out at the beginning of the measurement.

With the estimations of the focused and spherical vortex field it is clear that, apart from the noise outside of the second ring, the pressure field achieved by $\underline{\underline{H}}_4(\omega)\underline{E}_2^{sv}$ and $\underline{\underline{H}}_4(\omega)\underline{E}_3^{sv}$ are both in good agreement with the theoretical one. However, the two experimental measurements have a different origin points, and therefore result in a slight shift along the x-axis. This translation of the field can be responsible for the differences between $\underline{E}_2^{sv}$ and $\underline{E}_3^{sv}$, as observed in Fig. 4.27 and that was left unexplained.

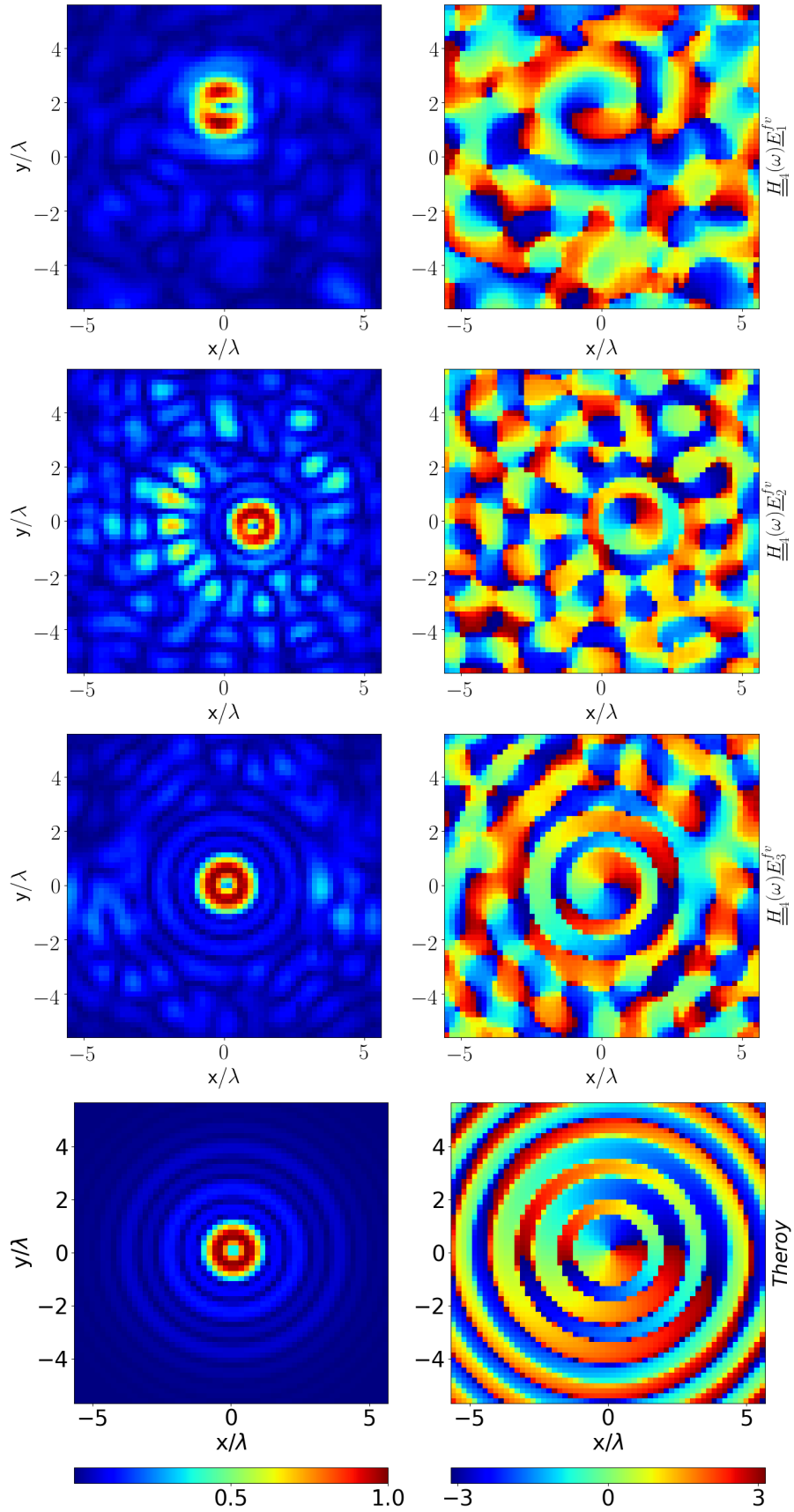

Figure 4.34: Modulus and phase of the complex pressure field in plane xy for a focused vortex of $m' = 1$.

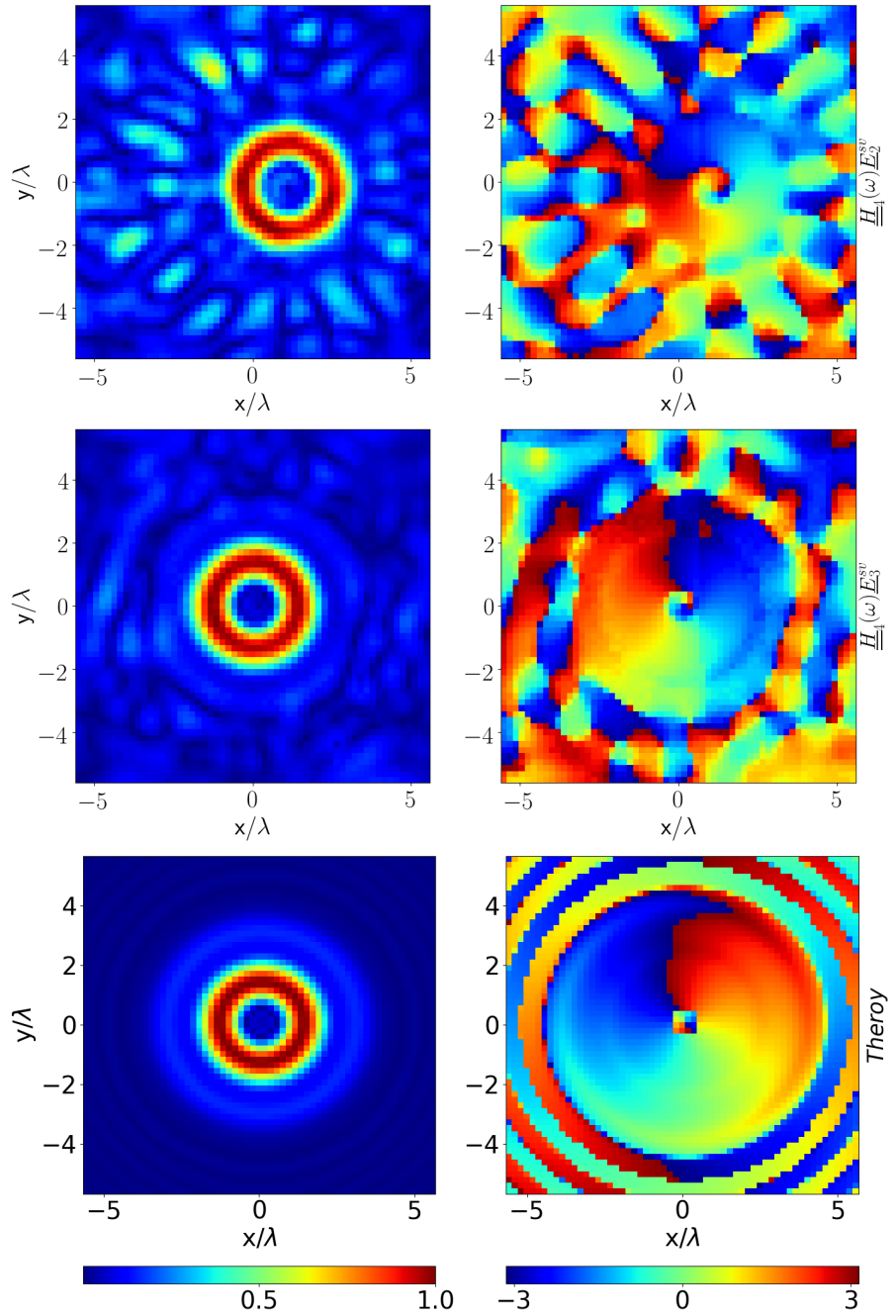

Figure 4.35: Modulus and phase of the complex pressure field in plane xy for a spherical vortex of $m' = 1$.

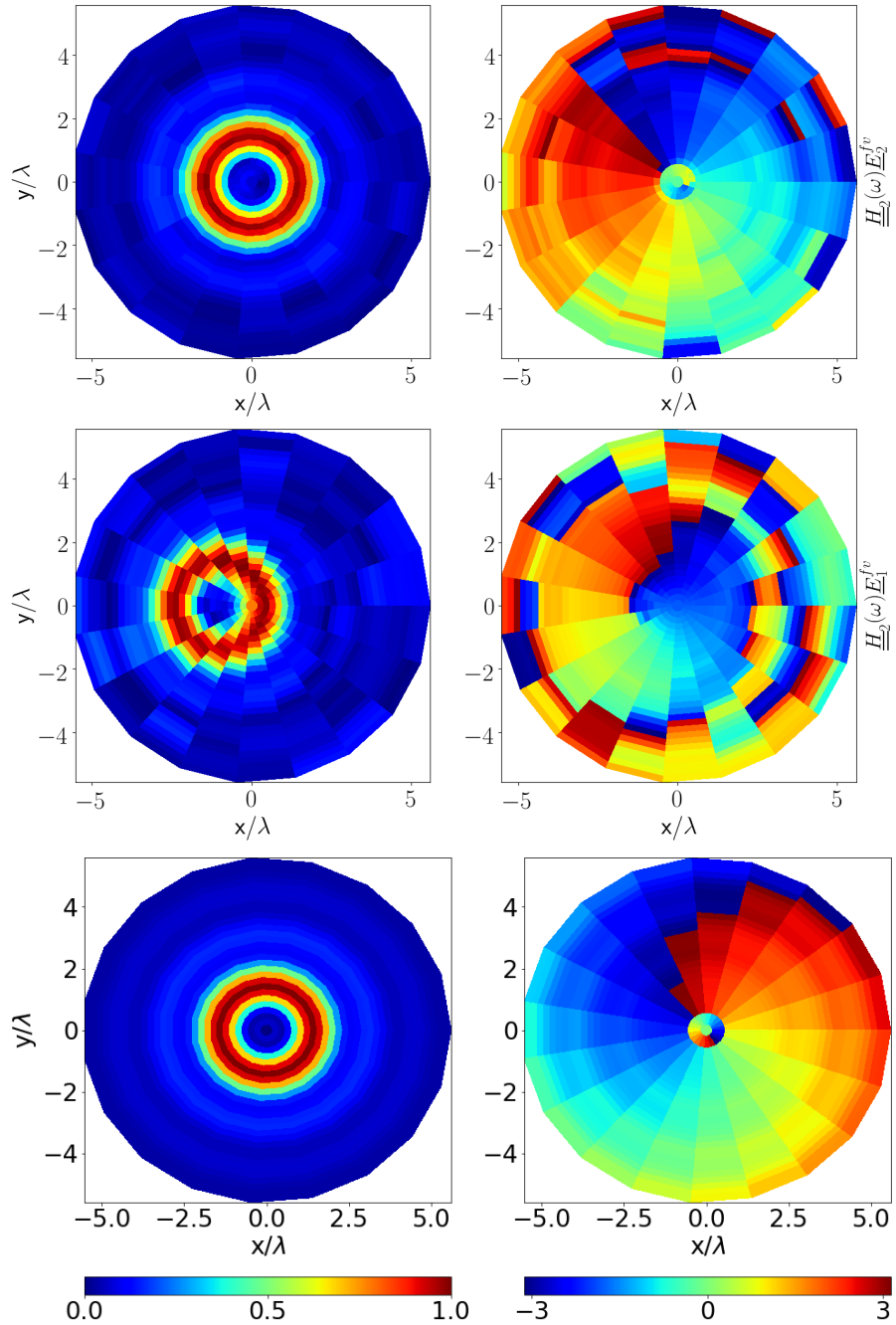

Figure 4.36: Modulus and phase of the complex pressure field in plane xy for a spherical vortex of $m' = 1$.

4.4 Conclusion

In this chapter we have successfully synthesized two kinds of vortex beams: a focused vortex and a spherical vortex. The spherical vortex, compared to the focused vortex beam, forms a more significant intensity gradient in the axial direction which allows a stronger axial trap. Its capability of trapping larger spheres leads us, for the first time, to synthesis this kind of wave field. To retrieve these fields, the inverse filtering method was employed. In this method, the distribution of the control points is crucial for the field synthesis. Therefore, three distributions of control points were used: a sphere of radius 20 mm with 974 Lebedev points, a disc of radius 7 mm in the focal plane with 581 points and a square of width 6 mm in the focal plane with 2500 points. The results were compared qualitatively by measuring the synthesized wave field experimentally and quantitatively by computing the BSC and radiation force using the method introduced in chapter 3.

In our analysis, we have found that the key to achieve the desired wave field is to construct a suitable mesh. The mesh of control points should be fine enough to allow recording all the necessary information of the target field in the propagation operator. The criterion of whether the distribution is adequate or not lies in the singular values. As we have analyzed in section 4.3.4, if the control point distribution is satisfactory, the corresponding singular values will have a group of values at the noise level, which signifies the oversampling.

To optimize the emission vectors, the influence of the cut-off value was also assessed in this chapter. The small singular values are supposed to be sensitive in the pseudo inverse step and should be set to zero. However, by taking different cut-off values and comparing the resulting fields and radiation forces, we noticed that the cut-off value does not have a noticeable impact on the field synthesis. The differences are not significant and mainly appear in the field outside the high-intensity ring. Therefore, the most important factor that determines the field synthesis quality is the distribution of control points.

Chapter 5

Trapping and manipulation of elastic spheres by acoustic vortex

5.1 Introduction

In the previous chapter, we have synthesized experimentally two types of acoustic vortex: focused vortex beam and spherical vortex beam, by the inverse filter method. These vortex beams are used in this chapter to trap and manipulate elastic spheres. The focused and spherical vortex beams are introduced roughly in chapter 2. However, for a spherical vortex, some of the parameters should be chosen cautiously to achieve trapping for larger spheres. So in the first section, we introduce a tailored spherical vortex with optimum trap capability for a given target. Then, as a preparation of experiments, the analysis of its ability for trapping sphere with different sizes and materials are made. Besides, in order to exert larger forces, some modifications of the emission vectors, obtained by inverse filtering, are applied. In the last section, the experimental setup of the manipulation and the result of sphere trapping by focused and spherical vortex beams are illustrated.

5.2 Acoustical trap by a spherical vortex

5.2.1 Spherical vortex

A spherical vortex, as its name, describes a vortex beam with the pressure field of spherical pattern at the central beam core. Its capability for trapping depends highly on the beam shape, for example, the radius of the intensity ring. As presented in chapter 2, for a spherical vortex, the shape of the vortex is determined mainly by three factors: the aperture angle α_0, the topological charge m', and the degree l of the associated Legendre polynomial $\tilde{P}_l^{m'}(x)$ in Eq. (2.51). Among these factors, the aperture angle α_0 is limited by the lens that is used experimentally to focus the field, and the maximum angle allowed by our lens is 49°. To achieve the desired forces acting on an elastic sphere, the optimal topological charge m' and the degree l should be chosen. The degree l of the associated Legendre polynomial $\tilde{P}_l^{m'}(x)$, as explained earlier in chapter 2, is chosen to have an amplitude that varies smoothly in the range of $\theta_0 = [\pi - \alpha_0 : \pi]$ (the source aperture) and gently drops near zero at $\pi - \alpha_0$ to avoid strong secondary lobes in the radiated field. As depicted in Fig. 5.1 the topological charge m' is fixed at 1, $\tilde{P}_l^{m'}(x)$ with $(x = \cos(\theta))$ as a function of α_0 is plotted for different degree l. According to the figure, the degree $l = 8$ is the most adapted while $m' = 1$.

As far as the topological charge m' is concerned, in Fig. 5.2, the amplitude of the pressure field with $m' = 1$, $m' = 2$, $m' = 3$ in plane (x, y) and (x, z) are represented. In plane (x, y), the high-intensity ring keeps almost the same shape. Meanwhile, the pressure gradient in plane (x, z) varies a lot from $m' = 1$ to $m' = 3$. When $m' = 1$, the high intensity has a 'candy' form, the zero amplitude region is like a spherical 'candy' wrapped up by high pressure field. By increasing m' to 2, the zero amplitude region remains a spherical shape at the center, whereas, the high pressure packing of the zero region begins to open at the two sides. For $m' = 3$, the zero region turns totally into a cylindrical shape. To analyze the impacts of the beam shape on the radiation forces, in Fig. 5.3, the radiation forces exerted on a polyethylene sphere of radius $a = 0.45\lambda$ for different topological charges are depicted. The radial and azimuthal forces are similar between the three, from $m' = 1$ to $m' = 3$. Only the amplitude of the forces decreases as a result of the decrease of intensity at the pressure field. In terms of the axial forces, notable differences come up. For $m' = 3$, the sphere sustains a tiny constant forward force. No trap

is formed in this vortex due to the lack of pressure gradient at the center of the vortex in the axial direction, which is shown in Fig. 5.2. Regarding the axial forces with $m' = 1$ and $m' = 2$, both cases create a trap for the sphere. However, the axial forces with $m' = 1$ are two times larger than $m' = 2$ owing to the beam shape, which gives rise to a greater pressure gradient. Therefore, to generate a spherical vortex with a good capability for trapping the target sphere, the topological charge $m' = 1$ and radial degree $l = 8$ are the most suitable.

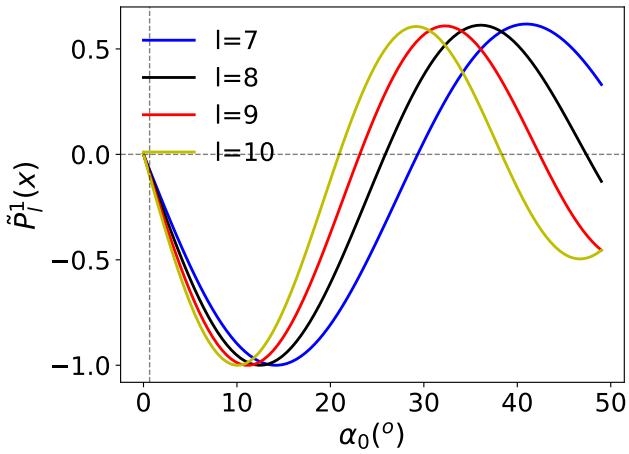

Figure 5.1: Normalized associated Legendre polynomial$\tilde{P}_l^{m'}(x)$ as a function of α_0.

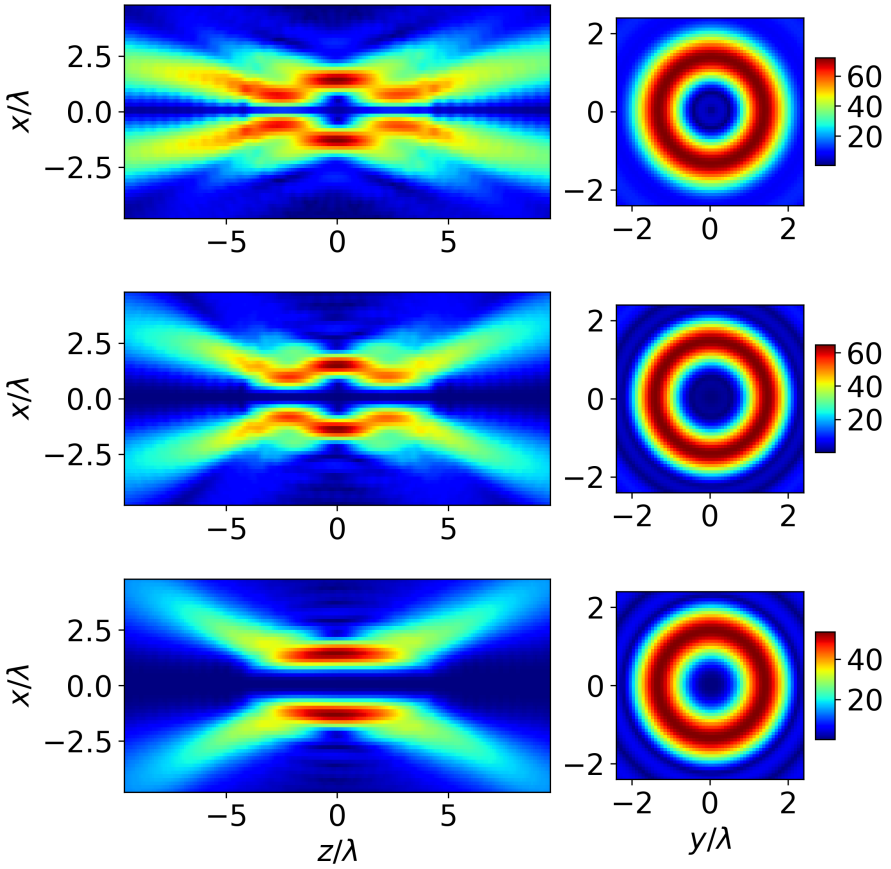

Figure 5.2: Modulus of the pressure field in plane (x, y) and (x, z) with different topological charges: $m' = 1$, $m' = 2$, $m' = 3$ (from top to bottom).

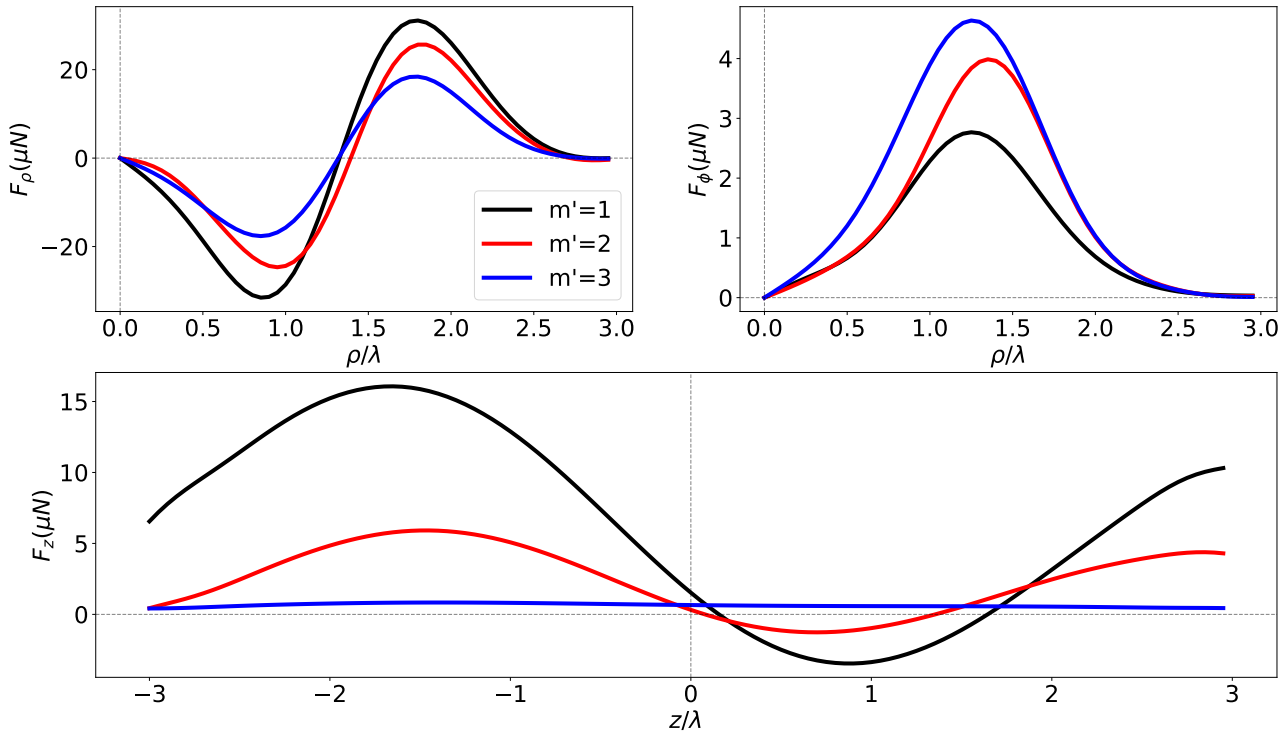

Figure 5.3: Radial F_ρ, azimuthal F_ϕ, axial F_z forces exerted on an polyethylene sphere of radius $a = 0.45\lambda$ by a spherical vortex beam with topological charge $m' = 1$, $m' = 2$, $m' = 3$.

The BSC in column $m = 1$ of a spherical vortex with topological charge $m' = 1$, radial degree $l = 8$ and a focused vortex with the same topological charge and an aperture angle α_0 are shown in Fig. 5.4. By tailoring the vortex with the associated Legendre polynomial $\tilde{P}_l^{m'}$ with radial degree $l = 8$, the location of the maximum modulus of BSC of the spherical vortex differs from the focused vortex. The modulus of BSC peaks at $n = 8$, which is equal to the radial degree l. Looking at the right of Fig. 5.4, the influence of the aperture angle is depicted. The width at half maximum decreases while increasing the aperture angle α_0. Therefore, choosing the radial degree $l = 8$ and aperture angle $\alpha_0 = 49^o$ for the spherical vortex concentrates the energy of BSC at $n = 8$, which, as shown in Fig. 5.3, gives rise to a more constant force to trap the sphere.

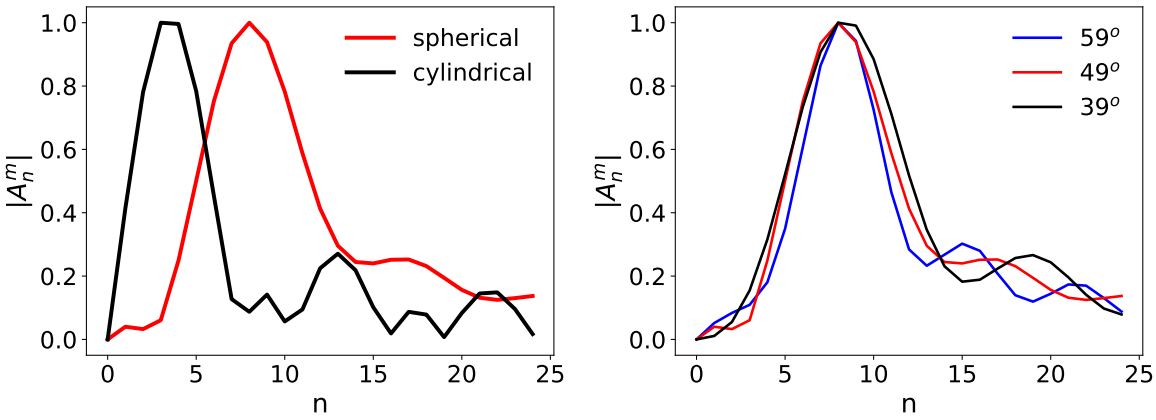

Figure 5.4: Normalized modulus of BSC of a spherical vortex with topological charge $m' = 1$, radical degree $l = 8$, aperture angle $\alpha_0 = 49°$, and a focused vortex with same topological charge and aperture angle (Left); normalized modulus of BSC of a spherical vortex with topological charge $m' = 1$ and radical degree $l = 8$, and aperture angle $\alpha_0 = 59°, 49°, 39°$ (Right).

Trapping capability of a spherical vortex through different spheres

The previous section has shown that a spherical vortex tailored with topological charge $m' = 1$ and radial degree $l = 8$ is adequate to trap a polyethylene sphere of radius $a = 0.45\lambda$ (Fig. 5.3). However, according to our estimation of the axial forces for a polyethylene sphere of different radii, the trapping capability of the spherical vortex, especially the axial trap, is not constant. As depicted in Fig. 5.5, among the polyethylene spheres of radii $a = 0.4\lambda$, $a = 0.45\lambda$ and $a = 0.48\lambda$, the radial trap always exists. Nevertheless, only the sphere with $r = 0.45\lambda$ can be trapped axially.

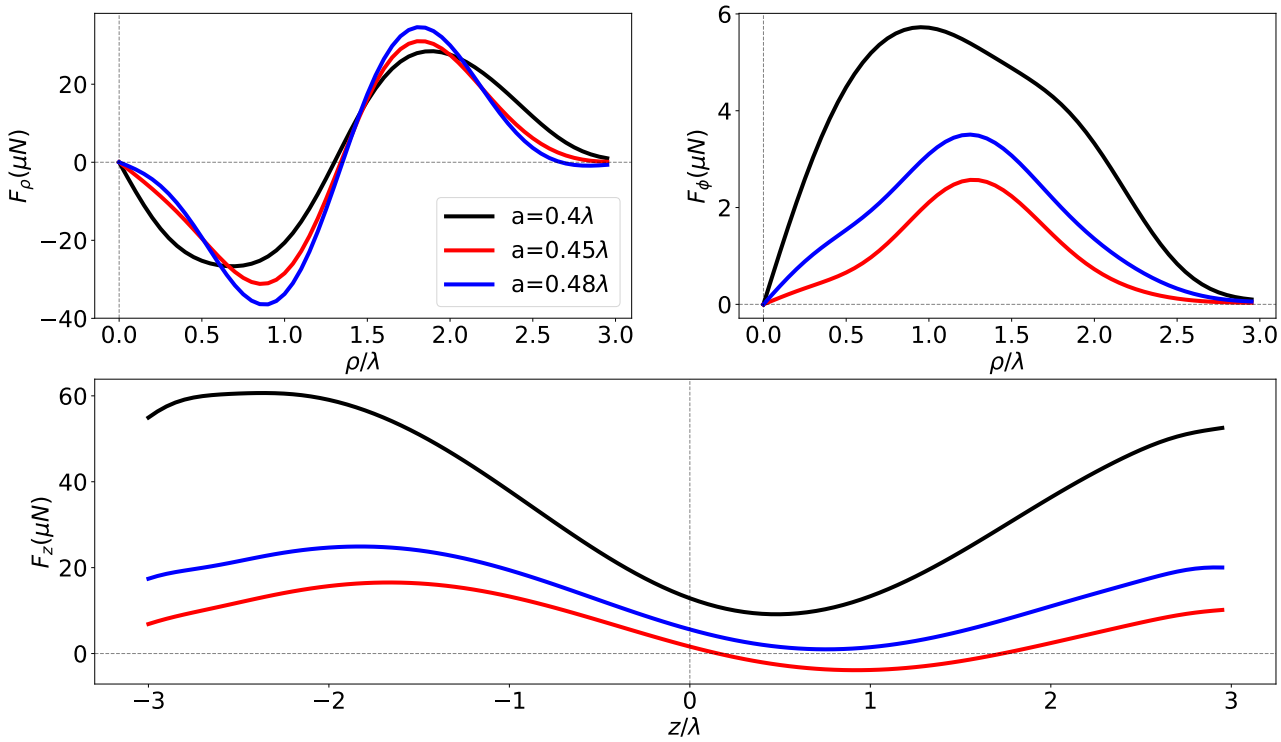

Figure 5.5: Radial F_ρ, azimuthal F_ϕ, axial F_z forces exerted on a polyethylene sphere of radii $a = 0.4\lambda$, $a = 0.45\lambda$, $a = 0.48\lambda$ by a spherical vortex beam.

Therefore, to succeed in trapping the particles experimentally, it is important to test the range of sizes and materials that can be trapped, especially in the axial direction of a spherical vortex. The negative force in the axial direction is the key to trap the particles. Thus, the determination of the suitable range of polyethylene sphere sizes requires only to compute the axial force at a position where the negative force is most likely to appear. According to Fig. 5.5, for instance, at $z = 0.9\lambda$ the axial force is negative with a maximum amplitude for a polyethylene sphere of $a = 0.45\lambda$. In Fig. 5.6, the axial force at $z = 0.9\lambda$ as a function of sphere radius is represented. As illustrated in the figure, from $a = 0.2\lambda$, the resonances begin to appear in the axial force and thereafter regions for which the axial force is negative alternates with regions where the force is positive. From the figure, the zone where $F_z < 0$ represents the range of sphere radius that can be trapped. Only the spheres with radii between (0.42λ and 0.47λ) or (0.5λ and 0.54λ), (0.59λ and 0.64λ) have a negative force and therefore can be trapped by the spherical vortex. This result agrees with the force estimation in Fig.5.5, since the spheres of radii $r = 0.4\lambda$ and $r = 0.48\lambda$ are at the resonances of the axial force, it is impossible to trap them axially.

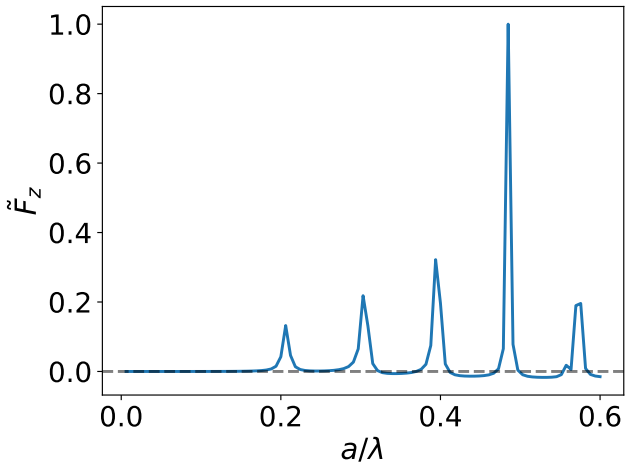

Figure 5.6: Normalized axial forces $\tilde{F}_z$ exerted on a polyethylene sphere positioned at $z = 0.9\lambda$ as a function of sphere radius by a spherical vortex.

These resonances of the force come from the resonances of the scattering coefficients R_n. As the axial force is calculated by Eq. (2.23) ($F_z = -2\frac{\langle V \rangle}{k_0^2} \sum_{n=0}^{\infty} \sum_{|m|<n} \Im(G_n^m A_n^{m*} A_{n+1}^m C_n)$.), where C_n is a function of the scattering coefficients ($C_n = R_n^* + R_{n+1} + 2R_n^* R_{n+1}$). In Fig. 5.7, the modulus of C_n is plotted for a polyethylene sphere as a function of radius. Comparing Fig. 5.6 and Fig. 5.7, the resonances in C_n locate at the same positions as the resonances observed in the axial forces. The figure also illustrates that for $a < 0.6\lambda$, the coefficients C_n with $n > 6$ can be neglected since from $n = 6$ the amplitudes become weak. As the force is a sum on degree n, we define here $\hat{f}_z^n$ as the force in degree n:

$$\hat{f}_z^n = -\Im(G_n^m A_n^{m*} A_{n+1}^m C_n). \tag{5.1}$$

The contribution of $\hat{f}_z^n$ to the negative force at each degree n can be computed by Eq. (5.1). In Fig. 5.8, the $\hat{f}_z^n$ until degree $n = 6$ are depicted. Taking the trapping region between 0.42λ and 0.47λ as an example, according to the figure, $\hat{f}_z^n$ with negative amplitudes that contribute to the final negative force are at degrees $n = 2$, $n = 3$ and $n = 4$.

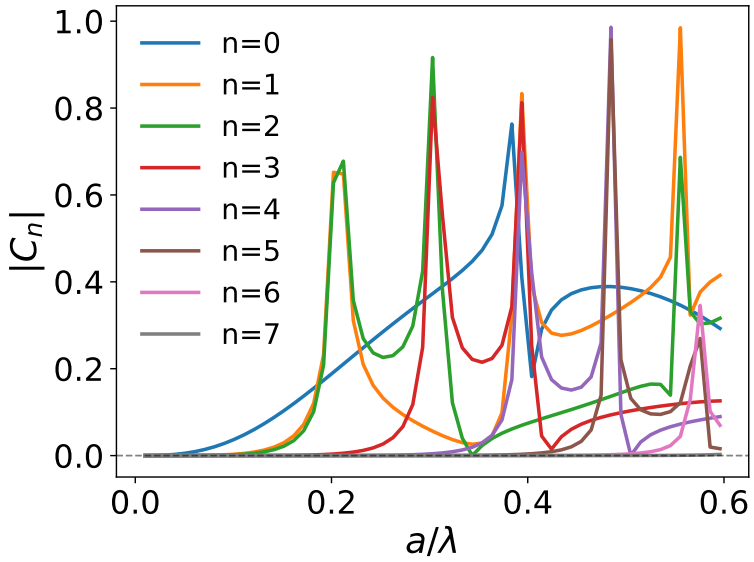

Figure 5.7: Modulus of C_n as a function of sphere radius for a polyethylene sphere.

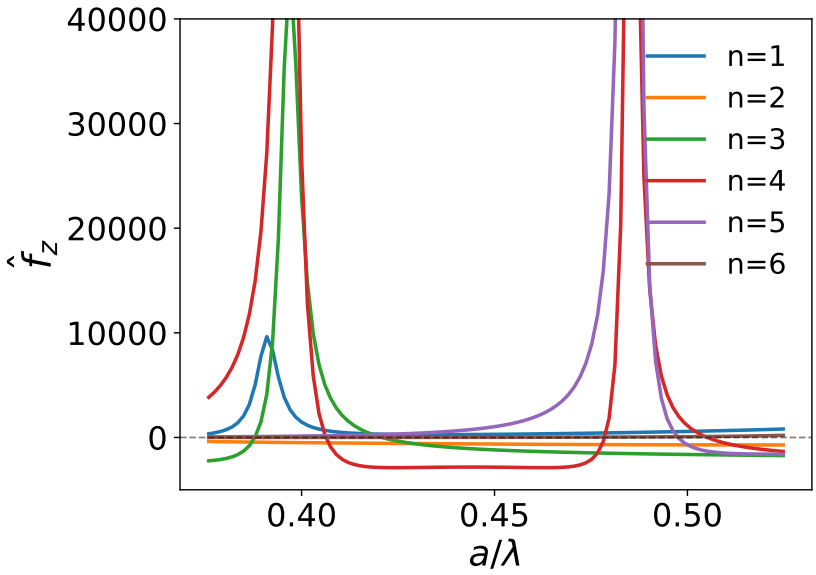

Figure 5.8: $\hat{f}_z^n$ as a function of sphere radius for different degrees until $n = 6$ for a polyethylene sphere.

In order to find the relation between the coefficients C_n and its contribution to the negative force, the coefficients C_n of polyethylene sphere at degree $n = 2$, $n = 3$ and $n = 4$ are depicted in Fig. 5.9. In the figure, the region within which the negative force appears is highlighted by two gray dashed curves. In the trapping region, the modulus of C_n as well as the phase are constant and located between two resonances. The phase inside the trapping region is approximately $\frac{\pi}{2}$. As the axial force is the imaginary part of the product of $A_n^{m*} A_{n+1}^m$ and C_n

with an opposite sign (-1) in front, thus to obtain a negative force requires the sum of phase to be inferior to π. In Fig. 5.10, the modulus and phase of $A_n^{m*}A_{n+1}^m$ are plotted. Even though the maximum of the modulus is at $n = 8$, the corresponding phase is however at $\frac{\pi}{2}$ (the gray dashed line represents the position where the phase is $\pi/2$), with the phase of C_n at $\frac{\pi}{2}$ simultaneously, which results in a sum of phase equal to π and does not contribute to the axial restoring force at all and will, on the contrary, push away the sphere. Meanwhile, at degree $n = 2$, $n = 3$ and $n = 4$, the phases are the smallest and give rise to a positive real part which finally contributes to the negative restoring forces.

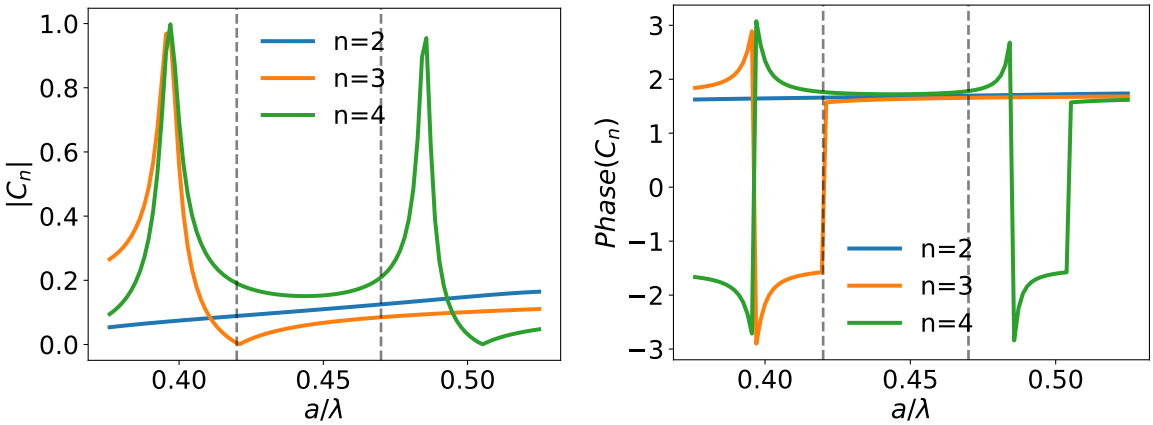

Figure 5.9: Modulus and phase of C_n as a function of radius at degrees $n = 2$, $n = 3$, $n = 4$ for a polyethylene sphere.

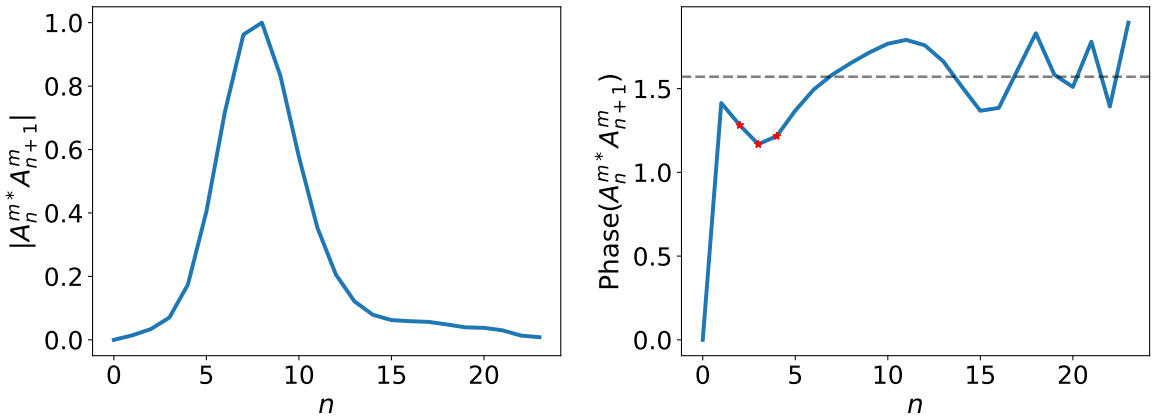

Figure 5.10: Modulus and phase of $A_n^{m*}A_{n+1}^m$ as a function of degree n.

The trap capability of the spherical vortex on a polystyrene sphere can be examined in the same way. The axial force exerted on a polystyrene sphere at position $z = 0.9\lambda$ as a function of the polystyrene sphere radius is computed and shown in Fig. 5.11. According to the figure,

the negative force appears at some of the radii but the amplitude is very weak. For one of the regions between $a = 0.46\lambda$ and 0.49λ, the $\hat{f}_z^n$ are plotted in Fig. 5.11. The $\hat{f}_z^n$ contributing to the negative force are at degrees $n = 2$, $n = 3$, $n = 4$. Then we plot the coefficients C_n as shown in Fig. 5.12. Similar to the polyethylene sphere, inside the trapping zone, the modulus and phase of C_n are constant. The phases at degree $n = 2$, and $n = 3$ are close to $\frac{\pi}{2}$ while at degree $n = 4$, the phase is larger and is equal to $\frac{2\pi}{3}$. As the sum of C_n phase and $A_n^{m*}A_{n+1}^m$ phase at $n = 4$ is close but less than π this results in a small negative force. Moreover, since the function sin (the imaginary part) decreases linearly around π, a decrease of phase thus results in a proportional increase of the modulus of the negative force.

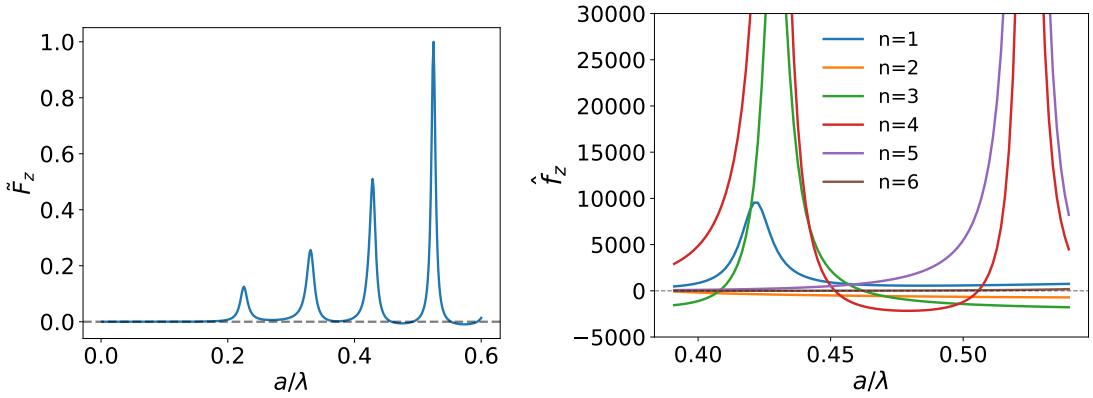

Figure 5.11: Normalized axial $\tilde{F}_z$ forces exerted on an polystyrene sphere positioned at $z = 0.9\lambda$ as a function of sphere radius (Left); $\hat{f}_z^n$ as a function of sphere radius for different degrees until $n = 6$ (Right).

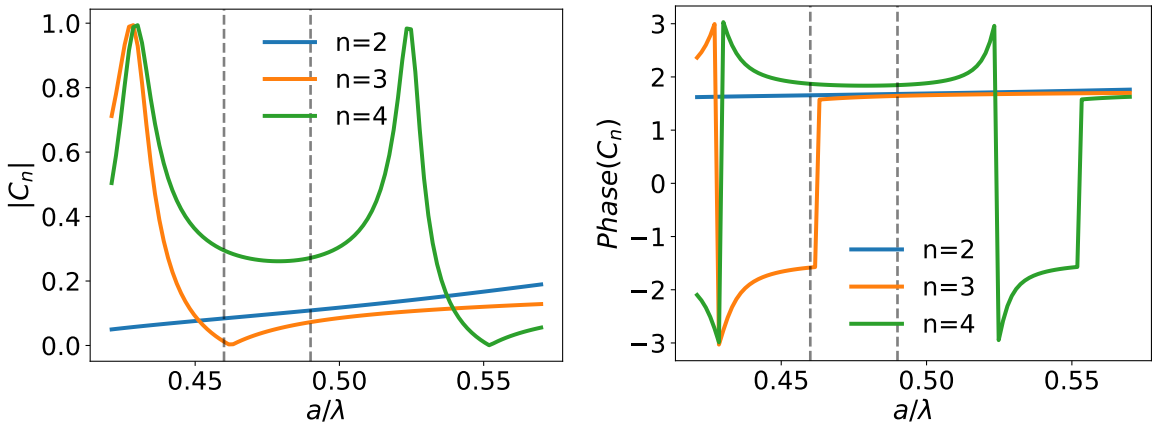

Figure 5.12: Modulus and phase of C_n as a function of sphere radius at degrees $n = 2$, $n = 3$, $n = 4$ for a polystyrene sphere.

As the scattering coefficients C_n of a polystyrene sphere depends only on its physical prop-

erties, the only way to trap a polystyrene sphere is to adjust the BSC of the spherical vortex beam to give rise to the negative force. The BSC of a spherical vortex, as demonstrated in the previous section, can be modified by changing the aperture angle α_0, the radial degree l, or topological charge m'. Taking the radial degree l as an example, in Fig. 5.13, the modulus and phase of $A_n^{m*}A_{n+1}^m$ with different radial degrees are shown. The gray dashed lines highlight the radial degrees of interest. Looking at the phases of each radial degree, the $l = 8$ gives rise to a phase significantly below $\pi/2$ in the region of interest and hence potentially to a large negative force. However, the modulus of the $A_n^{m*}A_{n+1}^m$, at the same degree n, decrease when l increases and this trend is in favor of the smallest l. Therefore the impact of changing the radial degree l on the negative force is not obvious. In Fig. 5.14, $\hat{f}_z^n$ as a function of polystyrene sphere radius with different radial degrees l in the BSC are shown. From the figure, only the BSC with radial degree $l = 8$ lead to the most significant negative force. In spite of the fact that the modulus of $A_n^{m*}A_{n+1}^m$ with $l = 8$ is smaller than those with $l = 6$, and $l = 7$, it has a smaller phase at the same time. Its advantage in phase makes it capable of creating a negative force. Thus comparing to the modulus, the phase is more crucial for the force computation in both C_n and $A_n^{m*}A_{n+1}^m$.

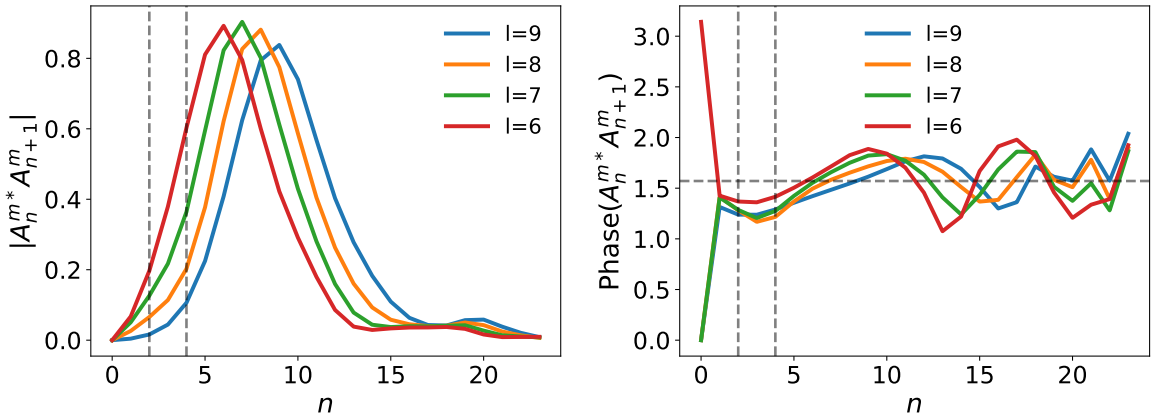

Figure 5.13: Modulus and phase of $A_n^{m*}A_{n+1}^m$ as a function of degree n for different radial degrees l.

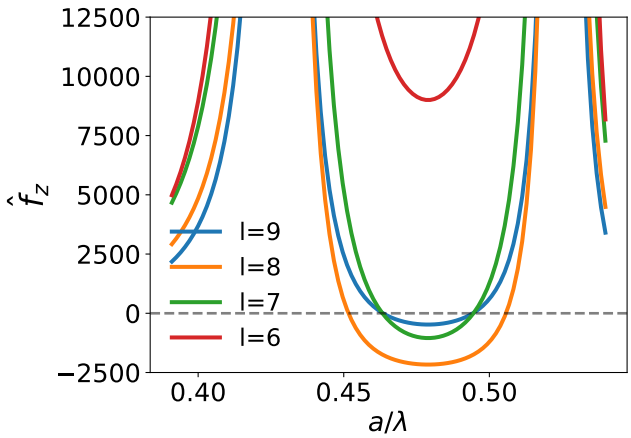

Figure 5.14: $\hat{f}_z^n$ at degree $n = 4$ as a function of sphere radius for different radial degrees l.

Another way to modify the BSC is to change the aperture angle α_0. In the previous analysis, the forces are calculated at $z = 0.9\lambda$ where the amplitude of negative axial force is maximal. This position can be changed as the aperture angle α_0 varies. Fig. 5.15 depicts the axial forces exerted on a polystyrene sphere by a spherical vortex with different aperture angles. The negative restoring force peaks at an axial position that depends on the aperture angle. For $\alpha_0 = 39^o$ and $\alpha_0 = 49^o$, at $z = 0.8\lambda$, the axial force reaches its minimum. Meanwhile, for $\alpha_0 = 59^o$ and $\alpha_0 = 69^o$, the minimums are at $z = 1.5\lambda$ and $z = 1.45\lambda$ respectively. We aim to compare and maximize the amplitude of the negative axial force. Thus the product of BSC $(A_n^{m*} A_{n+1}^m)$ for each aperture angle is computed in the corresponding position and is illustrated in Fig. 5.16. This indicates that the axial negative force can be strengthened by increasing the aperture angle. Increasing the aperture angle is, therefore, a method to get a polystyrene sphere trapped by a spherical vortex.

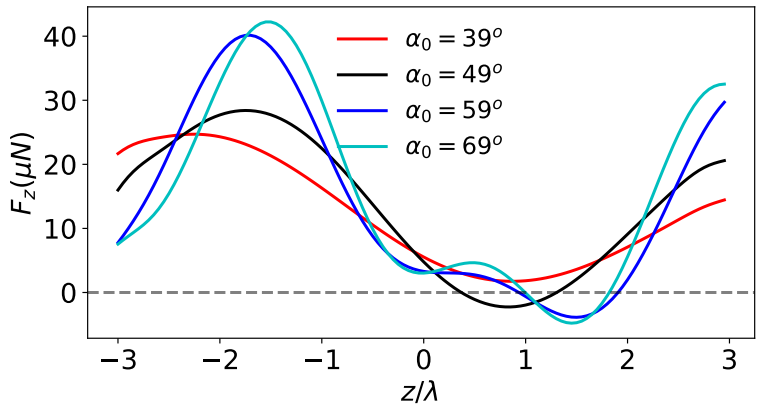

Figure 5.15: Axial forces exerted by a spherical vortex with different aperture angles on a polystyrene sphere of radius $a = 0.48\lambda$.

From the Fig. 5.16, we notice that the increase of α_0 from 49° to 59° and 69° gives rise to a modulation of the product $A_n^{m*}A_{n+1}^m$ at the degrees highlighted by the gray dashed curves. The phase with $\alpha_0 = 59°$ stays the same as $\alpha_0 = 49°$. However, when the aperture angle reaches 69°, the phase decreases comparing to 49° and 59°. This smaller value in phase can eventually results in a higher negative force as shown in Fig. 5.17.

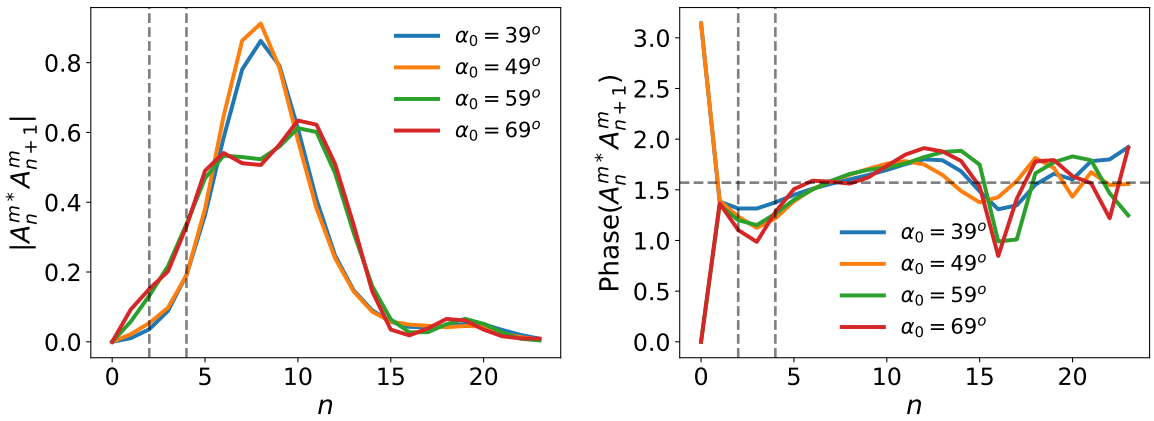

Figure 5.16: Modulus and phase of $A_n^{m*}A_{n+1}^m$ as a function of degree n for different aperture angles α_0.

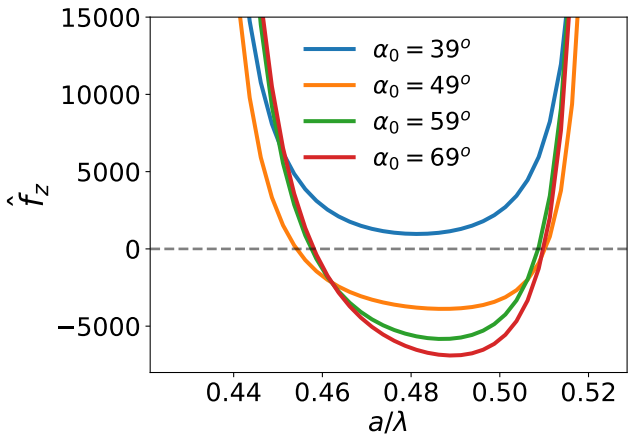

Figure 5.17: Sum of $\hat{f}_z^n$ as a function of sphere radius from degree $n = 2$ to $n = 4$ for a polyethylene sphere

In conclusion, the trapping ability of a spherical vortex is strongly dependent on the resonances and hence on the scattering coefficient. The axial trap can be achieved between two resonance peaks. Meanwhile, the BSC have significant effects on the amplitude of the negative force. To get the axial trap, we can either choose the suitable sphere material for a given vortex beam or adjust the BSC of the spherical vortex. As demonstrated previously, the polyethylene sphere with radii between 0.42λ and 0.47λ is a good target for a spherical vortex with topological charge $m' = 1$ and radial degree $l = 8$. Therefore, in the following experiments, the polyethylene sphere with corresponding sizes will be used.

5.2.2 Experimental synthesis of a spherical vortex

In chapter 4, we have demonstrated the method to synthesize a spherical vortex using the inverse filtering method. By knowing the desired acoustic field, and the pseudo-inverse of the propagation matrix, the emission signals of each transducer can be calculated. A focused spherical vortex with topological charge $m' = 1$ and radial degree $l = 8$, as selected in the previous section, is synthesized by inverse filtering. Its pressure field measured experimentally is depicted in Fig. 5.18 and Fig. 5.19. On the right column of Fig. 5.18, the emission vectors $\underline{e}^{sv}(t)$ calculated by Eq. (4.7) are presented in the top row. According to the figure, the energy is mainly distributed on the first 20 transducers and the other transducers have barely no contribution to the pressure field. Some modification of the emission vector $\underline{e}^{sv}(t)$ should be made, in order to make optimal use of all the transducers and, at the same time,

increase the intensity of the high-intensity ring. This will allow to exert larger radiation forces, especially for the axial force. First, for each transducer element, the signals are normalized $e_i^{sv}(t_j)/\max_i(\max_j(e_i^{sv}(t_j)))$, where i is the index of the transducer elements (from 1 to 127) and j is the index of the time sample. Then we multiply each signal by a new amplitude factor equal to $\left(\max_j(e_i^{sv}(t_j))/\max_i\left(\max_j(e_i^{sv}(t_j))\right)\right)^{\beta}$ with β equal to 0.5 or 0.25. As shown in Fig. 5.18, by applying these modifications, the number of signals with significant amplitude increases. Meanwhile, the pressure field obtained is also changed. The high-intensity rings keep the same pattern. While inside the rings, the intensity is no longer at zero amplitude and the phases have also changed. We calculate the pressure fields in the plane $z = 0$, on the axis $y = 0$ as displayed in Fig. 5.20. The amplitude of the modified field with $\beta = 0.25$ has increased almost by a factor 2 by comparing to the original emission. Moreover, the differences between the pressure field measurements in plane (x, z) are also clearly visible. With the original $\underline{e}^{sv}(t)$, the pressure field (on top) is quite close to the theoretical field (at the bottom). However, the two modified fields in plane (x, z), remain no longer the spherical pattern centered at the focal range.

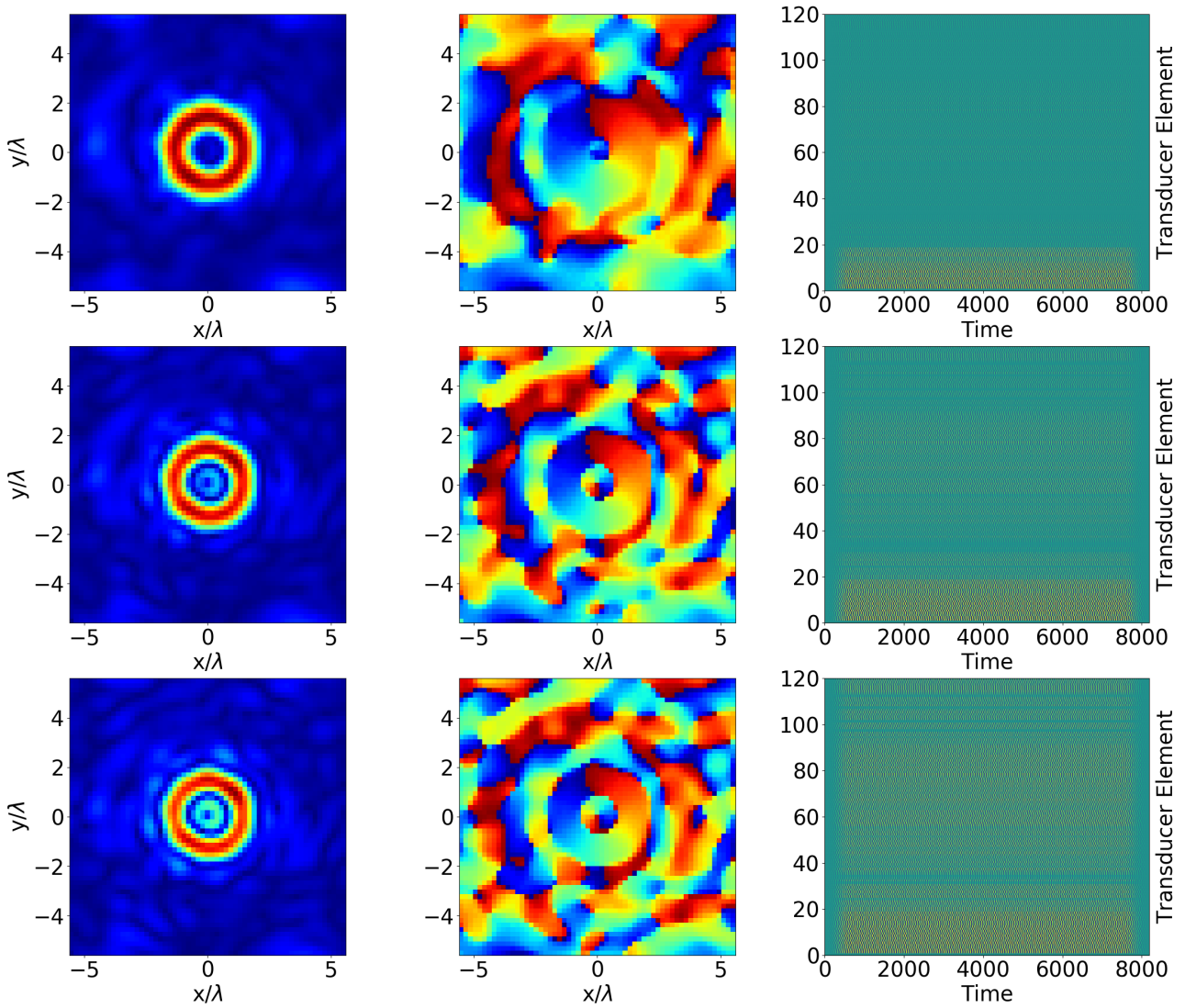

Figure 5.18: Experimental measurements of modulus (Left) and phase (Middle) of the complex pressure field in plane (x, y) for a spherical vortex beam with $l = 8$, $\alpha_0 = 49°$ obtained by different emission vectors (Right).

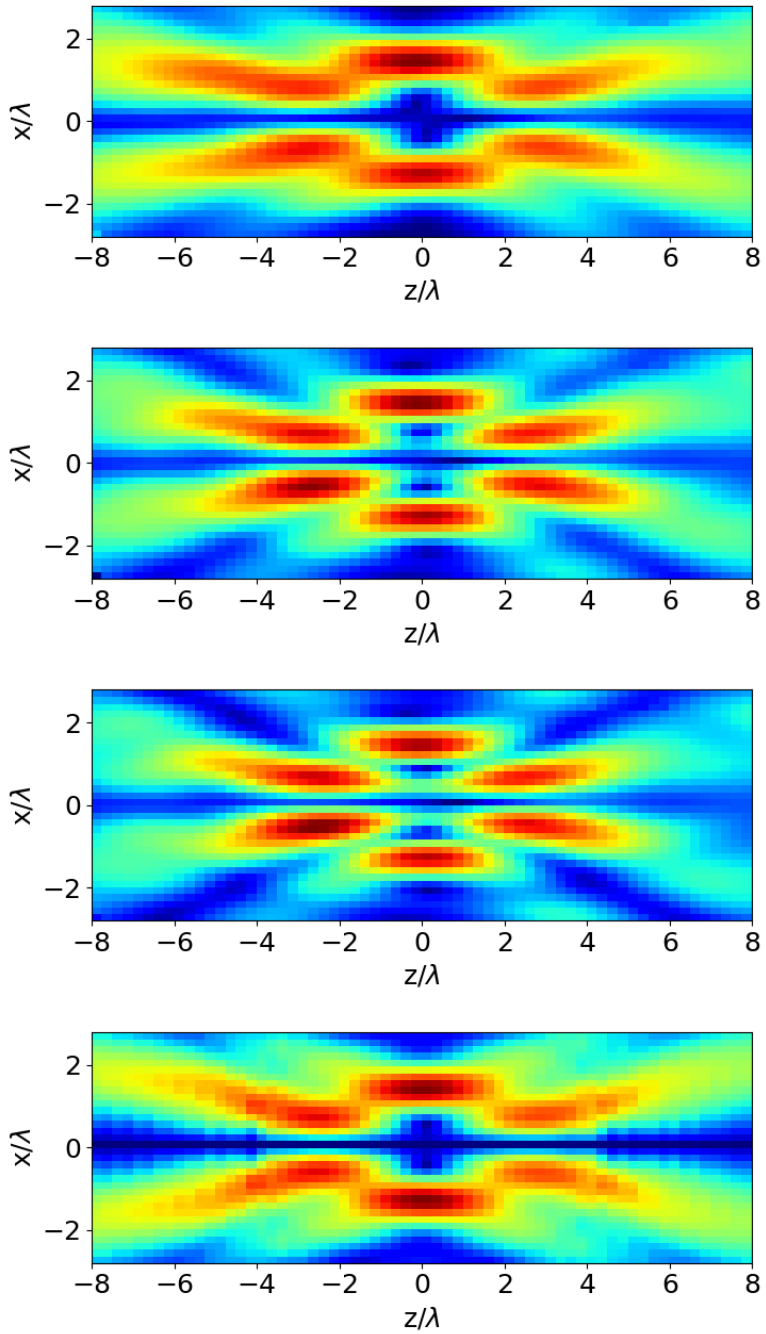

Figure 5.19: Modulus of the complex pressure field in plane (x, z) for a spherical vortex beam with $l = 8$, $\alpha_0 = 49°$ obtained by different emission vectors (from top to bottom): Original, $\beta = 0.5$, $\beta = 0.25$, theoretical.

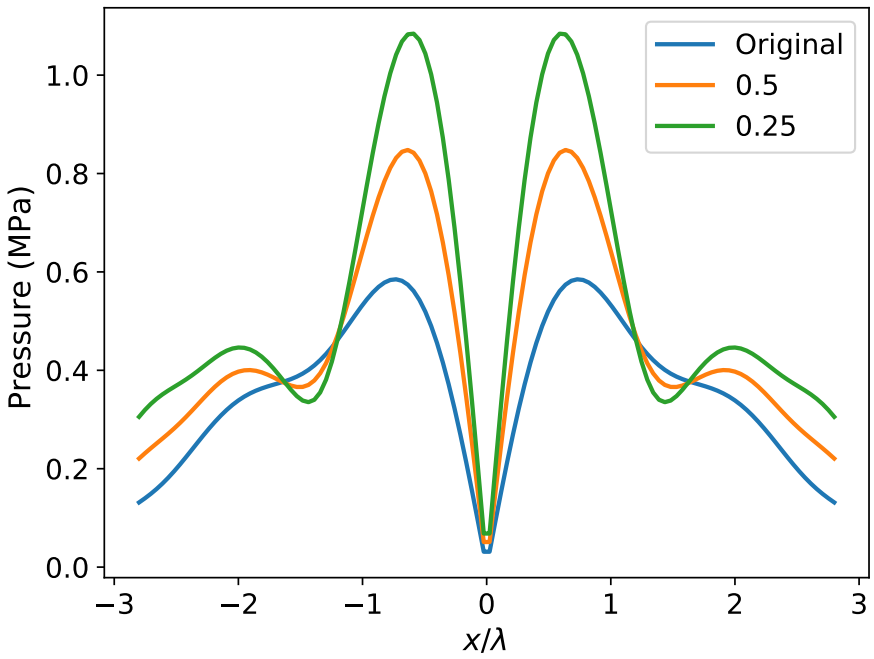

Figure 5.20: Pressure fields along axis x at focal distance $z = 0$.

In order to evaluate the impact of these modifications on the radiation forces, we use the angular spectrum method (ASM) demonstrated previously (Chap.3) to estimate the radiation forces. As depicted in Fig. 5.21, by modifying the vector $\underline{E}^{sv}$ from the origin up to $\beta = 0.125$, the amplitude of the radial force increases and the trap in radial direction remains always. For the axial force, when $z < 0$, the force is positive and increases notably with the decrease of the coefficient β. The maximum positive force with $\beta = 0.125$ is four times larger than the original one. However, when the sphere is located behind the focus ($z > 0$), the maximum amplitude of the restoring force increases until $\beta = 0.25$ and then decreases. Thus, according to the trapping performance illustrated by the radiation forces, the exponent $\beta = 0.25$ is optimum.

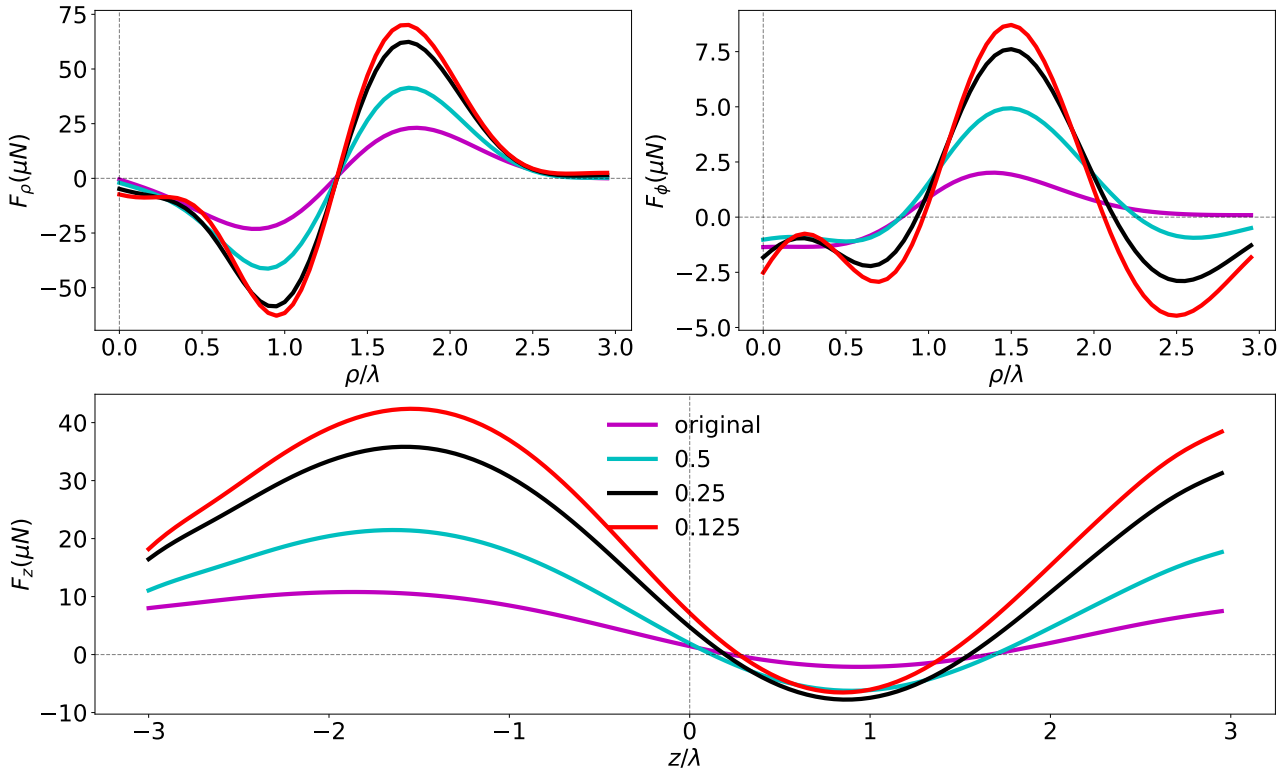

Figure 5.21: Radiation force exerted on a polyethylene sphere of radius $r = 0.45\lambda$ by a focused spherical vortex beam of topological charge $m' = 1$, $l = 8$ synthesized by different emission vectors with $\beta = 0$(original), 0.5, 0.25, 0.125.

5.3 Trapping and manipulation of a sphere with the acoustic vortex

Two types of vortex are used to trap the target experimentally: a focused vortex with topological charge m'=1 and aperture angle $\alpha_0 = 49°$ and a spherical vortex with the same aperture angle, topological charge and radial degree $l = 8$ as selected in the first section. The pressure field of the vortex in plane (x, z) and (x, y) are depicted in Fig. 5.22. As demonstrated in the figure, the spherical vortex has a trapping zone (zero pressure amplitude zone) with a spherical pattern at the center of the vortex beam, while the focused vortex has a smaller and cylindrical shape trapping zone in the axial direction. Since the shape of the trapping zone has an impact on the trapping capability of the sphere, spheres with different materials and sizes are chosen as listed in the Tab. 5.1.

Sphere	diameter (d (μm))	density ($\rho(g/cc)$)
polystyrene	355-425	1.098
polystyrene	2000	1.098
polystyrene	750-850	1.098
polyethylene	1000-1180	0.96
polyethylene	1000-1180	1

Table 5.1: The target spheres for trapping experience.

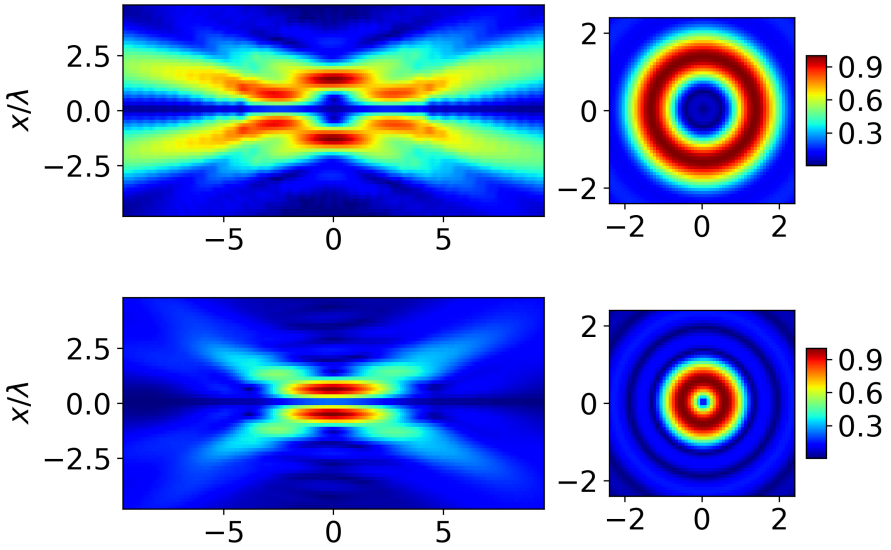

Figure 5.22: Pressure field of a spherical vortex (top) and focused vortex (bottom).

5.3.1 Experimental setup

The experimental setup is shown in Fig. 5.23. An array of 127 piezoelectric transducers is held by a vertical support to synthesize the desired beam in a large water tank. A high focal ratio acoustical lens is fixed in front of the transducers in order to focus the vortex. A very thin polyethylene film (with thickness $\approx 15\,\mu m$) that ensures minimal acoustic reflection is stretched on a bracket and is mounted on a three-axis motorized positioning system. The motors (Micro-Controller, Newport) are powered and controlled by a controller (Newport, MM-4006) with a maximum accuracy of $5\,\mu m$. Behind the optical window, an optical zoom image the area of interest and the image is recorded by a CMOS camera (ON Semi VITA1300, Model ID: FL3-U3-13Y3M-C). At the bottom of the vertical support, four wheels are installed to move the transducers.

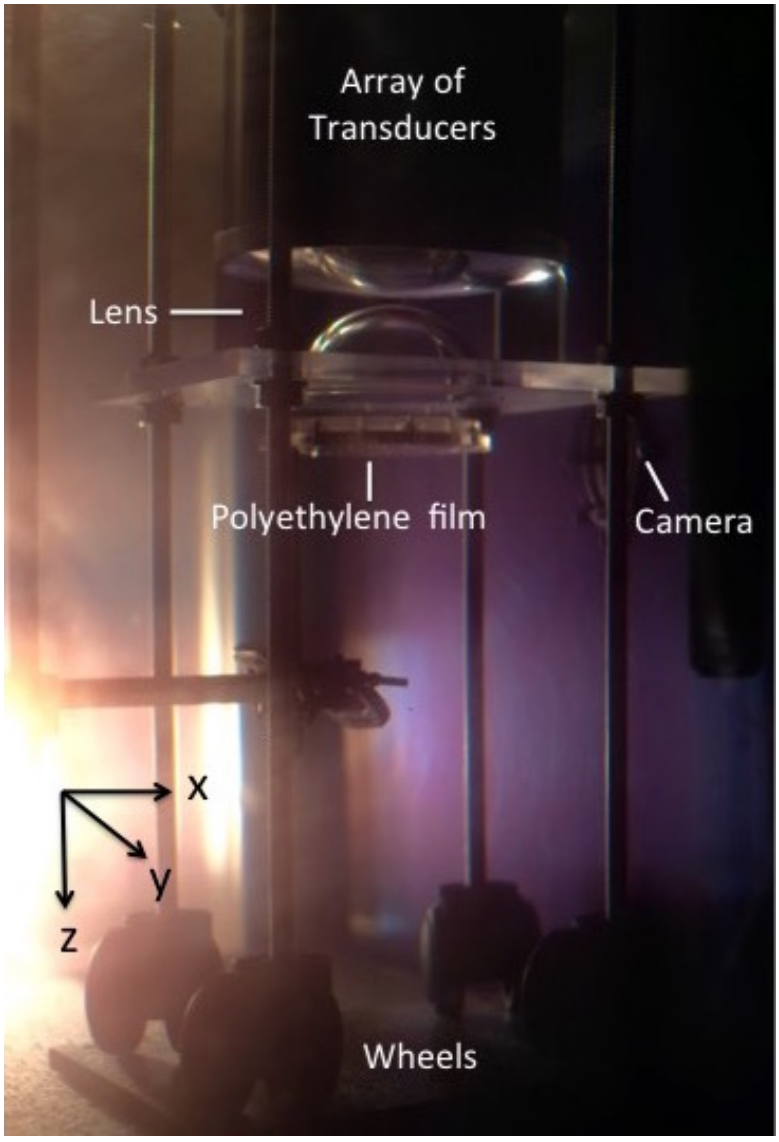

Figure 5.23: Experimental setup: an array of transducers are positioned vertically by a support; the emitted acoustic field is focused by the lens, a polyethylene film is stretched on a bracket which is connected to a motorized positioning system.

5.3.2 Finding the focal position of the vortex

In our experiment, we drive the transducers at a frequency $f = 1.2\,\mathrm{MHz}$ corresponding to a wavelength of $\lambda = 1.23\,\mathrm{mm}$ in water of $20\,^{\circ}\mathrm{C}$ where the speed of sound is about $1480\,\mathrm{m/\,s}$. A hydrophone of $0.2\,\mathrm{mm}$ diameter (Precision Acoustics Ltd, UK) scanning a grid of points defined near the focus measures the instantaneous pressure field to find the focal position of the vortex. The pressure field of the vortex in plane (x, y) has a ring shape pattern with zero amplitude at the center for both focused and spherical vortex as shown in Fig 5.22. As illustrated in the

figure, the ring of the focused vortex is smaller than the spherical vortex, as well as the zero amplitude region at the center which helps to identify the focal position more accurately. Thus, a focused vortex is synthesized experimentally to fix the focal position. Once the hydrophone is successfully positioned at the core of focal position, we then adjust the position of the camera to focus on the hydrophone, and at the same time make sure that the hydrophone is at the center of the camera screen. As depicted in Fig. 5.24, the hydrophone is clear and centered, the red dot on top of the hydrophone represents the focal position of the vortex. This step of fixing the focal position allows later to locate the sphere at the trapping zone of the vortex.

The camera used in our experiments has a maximum resolution of 1280×1024 with pixel size of 4.8 µm. As our experiment takes place in water, the light goes trough several optical medium and its refraction affects the magnification factor of our optical zoom. Thus, the calibration of our optical system is necessary. Since the hydrophone is mounted on the positioning system, by moving the hydrophone, the image size can be calculated according to the distance between two borders of the screen recorded on the motor controller. According to these experimental measurements, one pixel corresponds to 3 µm. Knowing the pixel size of the camera, can help to measure the radius of the trapping target, identify the equilibrium position of the trap, etc.

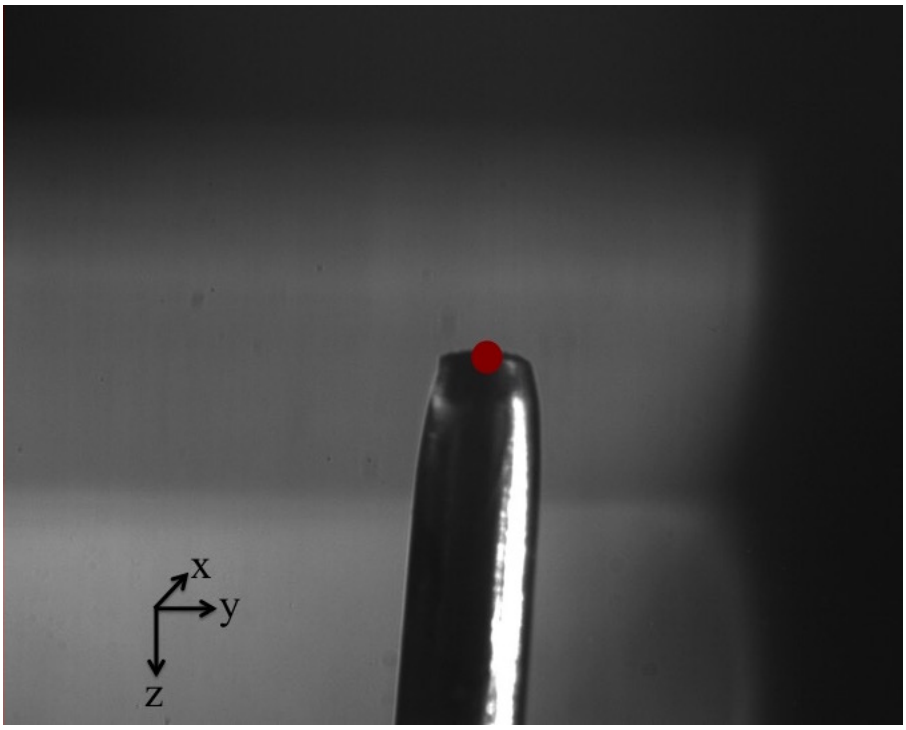

Figure 5.24: Photo of the hydrophone at the focal position.

5.3.3 Trap by a focused vortex

The trapping zone of a focused vortex is small, and as discussed in the previous section, resonances of scattering coefficients come up when the sphere is larger than $a = 0.2\lambda$. In our experiment, we use polystyrene beads of radii between 178 mm and 212 mm ($0.142\lambda - 0.17\lambda$) with density 1.098 g/cc as target spheres. After putting the beads on the film, by moving the film with the motorized positioning system, it is easy to locate the target bead at the trapping zone of the focused vortex. In Fig. 5.25, two beads are clear in the photo, indicating that they are both positioned in the focal plane. By moving the sphere to the center of the screen, the target sphere is positioned at the focal point of the focused vortex beam.

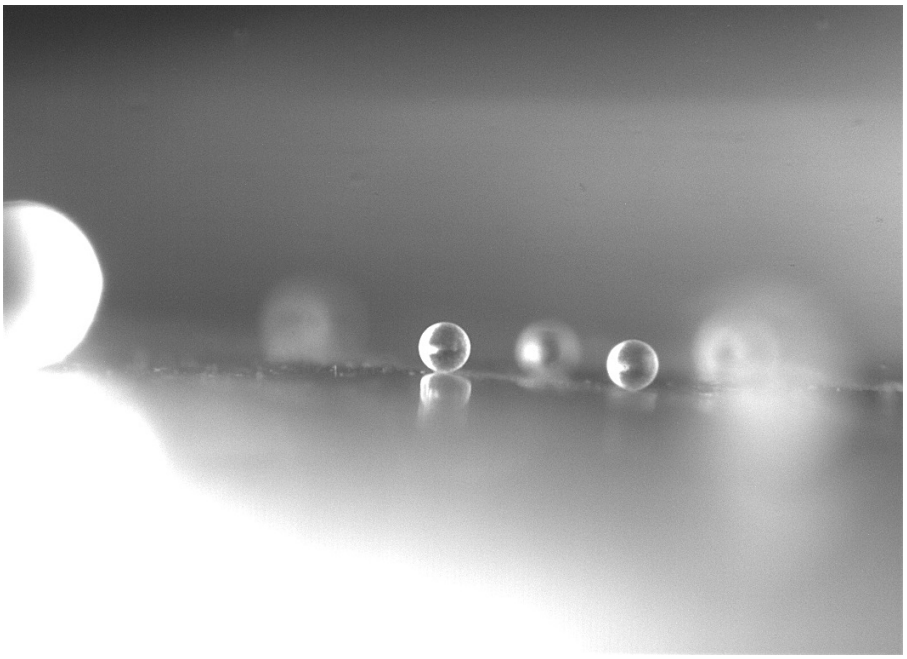

Figure 5.25: Photo of the polystyrene sphere at the focal position.

Once the bead is placed near the trapping zone, we then emit the focused vortex to trap it. The effect of the vortex beam is immediate and noticeable. As illustrated in Fig. 5.26, A is the initial position of the bead. The gray dashed curve represents the central axis of the vortex beam. As soon as we turn on the transducers, the bead with radius 0.15λ is firstly attracted by the radial force and moves towards the central axis and arrives at position B. Then the bead is lifted to position C, the equilibrium position. When it arrives at position C, the bead began to stabilize. It stays at the same position until the transducers are turned off. This experiment demonstrates that the focused vortex beam synthesized experimentally by the inverse filtering

method is able to trap a polystyrene sphere as estimated. To verify the selectivity of the vortex beam, several others spheres are placed in close vicinity of the target sphere. As depicted in Fig. 5.27, when the vortex beam is emitted, only one sphere is lifted. This confirms that the vortex trap is efficient and selective.

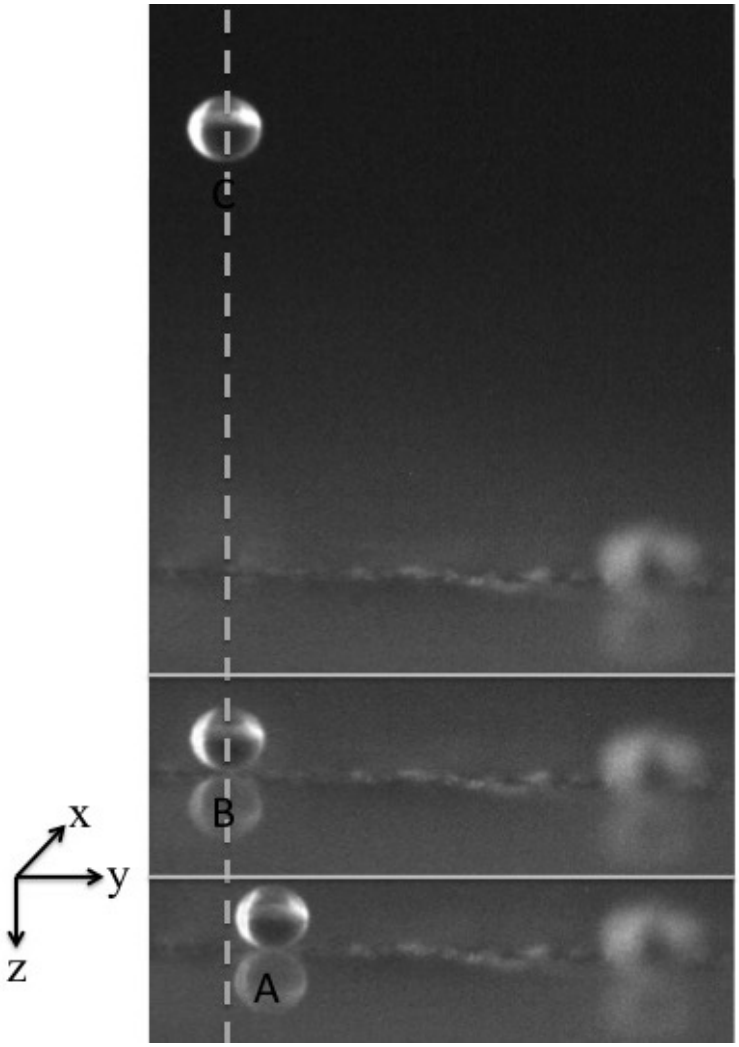

Figure 5.26: Snapshots of the trap by a focused vortex.

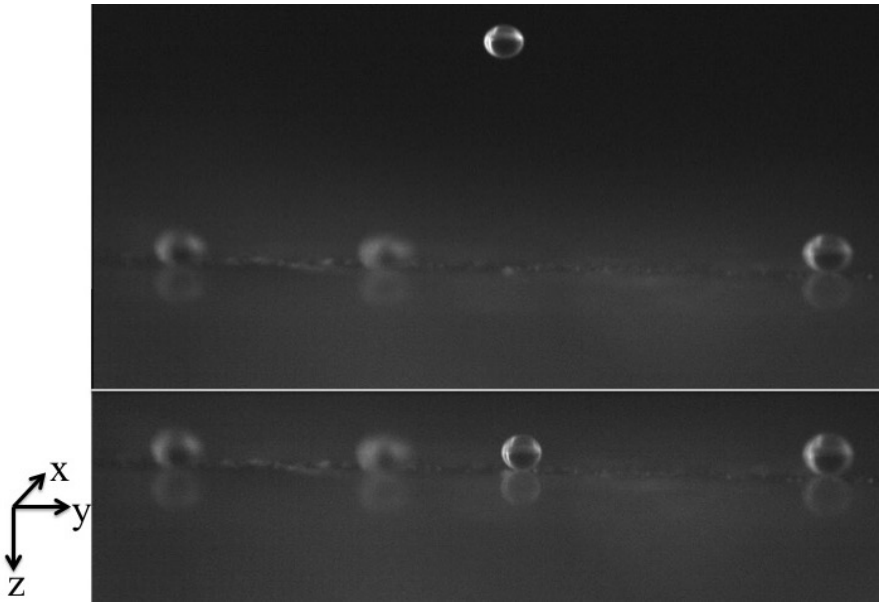

Figure 5.27: Snapshots showing the selectivity of a focused vortex beam.

Referring to the 3D manipulation, as the focused vortex is supposed to have the power of moving the trapped target in any desired direction, this capability of the 3D trap is also examined in our experiments. Figure 5.28 are the snapshots at different time and hence different location of the transducers array. The sphere is initially picked up in position A at T1, then transducers are moved towards the direction $-y$ at T2, the particle follows the movement of the transducers and reaches position B. The transducers are relocated towards direction $+y$, $+x$, and $-x$ at T3, T4, T5 respectively, the sphere is always trapped and moves along with the transducers as shown in figure.

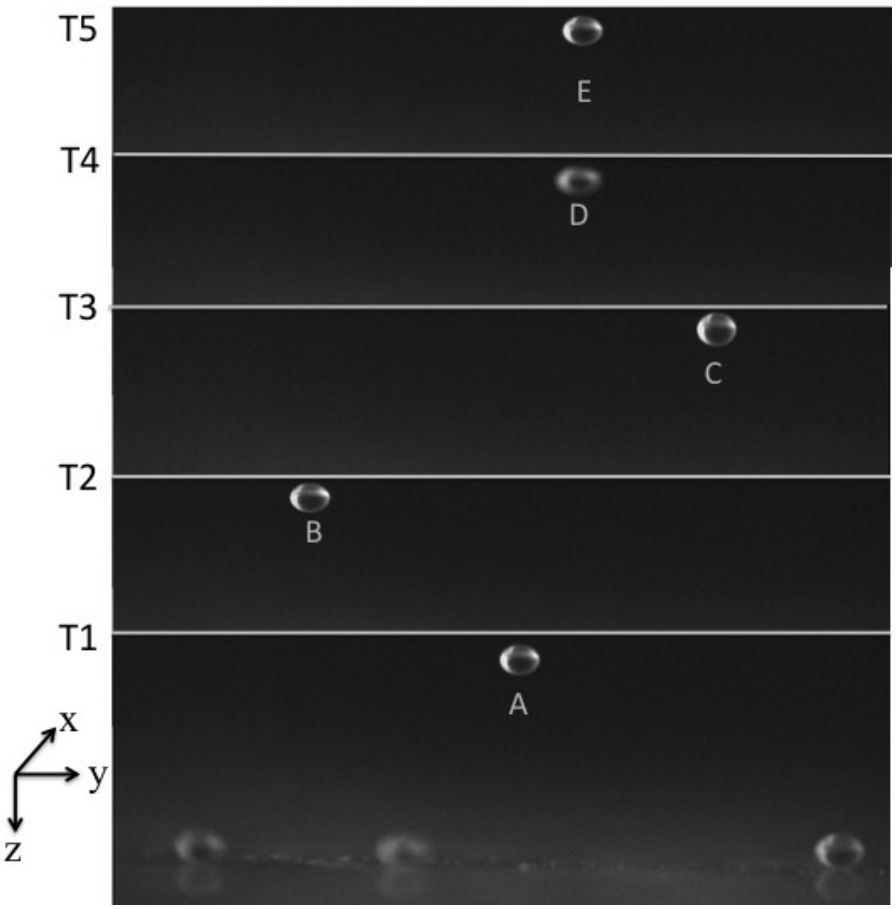

Figure 5.28: Positions of the bead by moving the transducers.

A polyethylene film with thickness 15 µm is used to support and move the spheres in our experiments. However, the radiation pressure due to a standing wave is much stronger than the one due to a progressive wave. As illustrated in chapter. 3, even 0.5% of counterprogating wave can induce notable oscillations in axial force. Even though, a very thin film is chosen to avoid the acoustic reflection, its influence to the radiation forces is not negligible. In order to observe the impact of the film on the axial forces, after the sphere is steadily trapped, the film is moved to different locations and the movement of the sphere is recorded by the camera. Figure 5.29 depicts the sphere positions at different moments with the film located at different positions. The red line in the figure represents the film position. At T1, the sphere is initially lying on the film at a position above the trapping zone. By lowering the film, when the sphere reaches the trapping zone, it is lifted and stabilizes at T2. Continuing descending the film, from T2 to T4, the sphere, as observed experimentally, at first, is slightly dragged down by the viscous force induced by the flow but remains trapped. When the film stops at a certain position, the sphere

is pulled up and stabilizes at a new equilibrium position as shown in the figure. At T5, the film is located far away from the sphere and disappears from the screen. At this moment, the sphere is no longer influenced by the flow which is induced by the movement of the film, and stays always at the same equilibrium position. The gray dashed curve represents the equilibrium position without the presence of the film. Then the film is moved in opposite direction and the new equilibrium positions of the sphere are recorded, T6 and T7. From T2 to T7, the variation of the sphere position is slight but not null which indicates that the influence of the film on the axial force is not negligible. When the film is the closest to the focal point as depicted in T7, the equilibrium position has goes up about 0.3λ. This position shift can be a result of standing wave created by a counterpropagating wave reflected by the film. Since the beam is sharply focused, the amplitude of this standing wave decreases rapidly as the membrane moves away. Therefore, to diminish the effect of the film on the radiation force, we should make sure the film is not too close to the target while trapping.

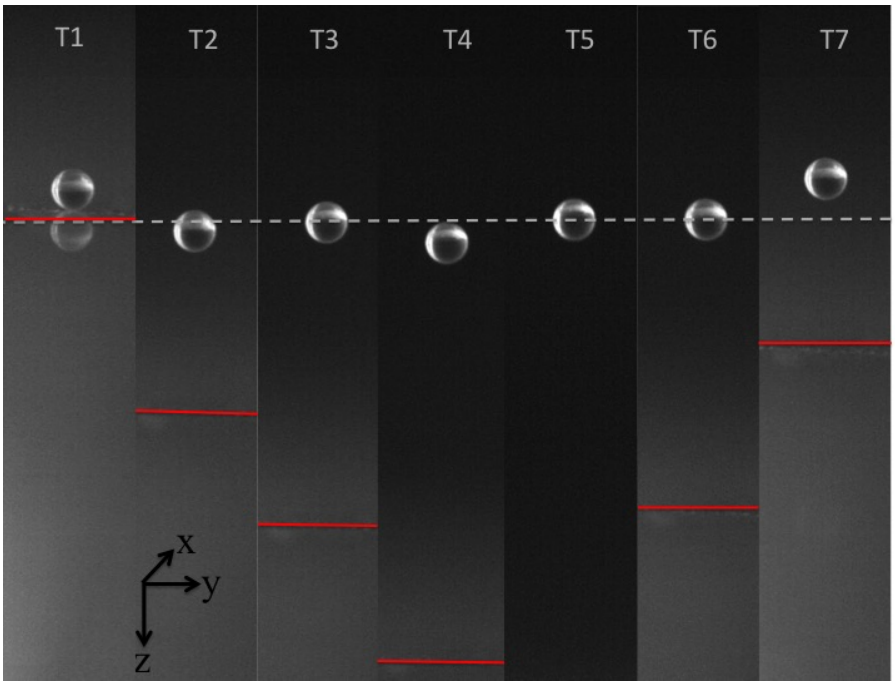

Figure 5.29: Snapshots of the hydrophone at the focal position.

5.3.4 Trap by a spherical vortex

In the case of a spherical vortex, as explained in the previous section, the trapping target becomes larger and the resonances start to come up which resulted in a more complicated

trapping condition. Consequently, the physical properties of the sphere become more important for the trapping effect. Two kinds of polyethylene spheres that are most likely to be trapped were tested in our experiments: sphere with radius between 500 µm and 590 µm ($0.4\lambda - 0.47\lambda$) with density 1 g/cc and 0.96 g/cc. According to the experimental results, none of these spheres were fully trapped by the spherical vortex beam and only radial trap was identified during the experiments. Three reasons can probably be responsible for the failure of the axial trap. First, polyethylene sphere attracts each others through an electrostatic force. They were dispersed in water with the help of a surfactant. We tried to apply this surfactant to the polyethylene membrane also. Nevertheless, this was far from perfect and the static force between the sphere surface and the film has to be overcome in order to lift the sphere. Second, the resonances of the scattering coefficients are of great importance to the axial trap. The frequency of these resonances is strongly dependent of the physical properties of the sphere material and these properties are not characterized by the supplier. Third, the polyethylene particles sphericity is very variable from one sphere to the other and never of good quality. Since the location and magnitude of the resonances are also strongly dependent on the geometry, this plays a role similar to change in material properties and may explain the axial trap failure. Even though the axial trap was not successful in our experiments with the spherical vortex trap, the radial trap has always been strong and constant. As shown in Fig. 5.30, a polystyrene sphere is radially trapped, while moving the polyethylene film, the particle stays trapped in the same position.

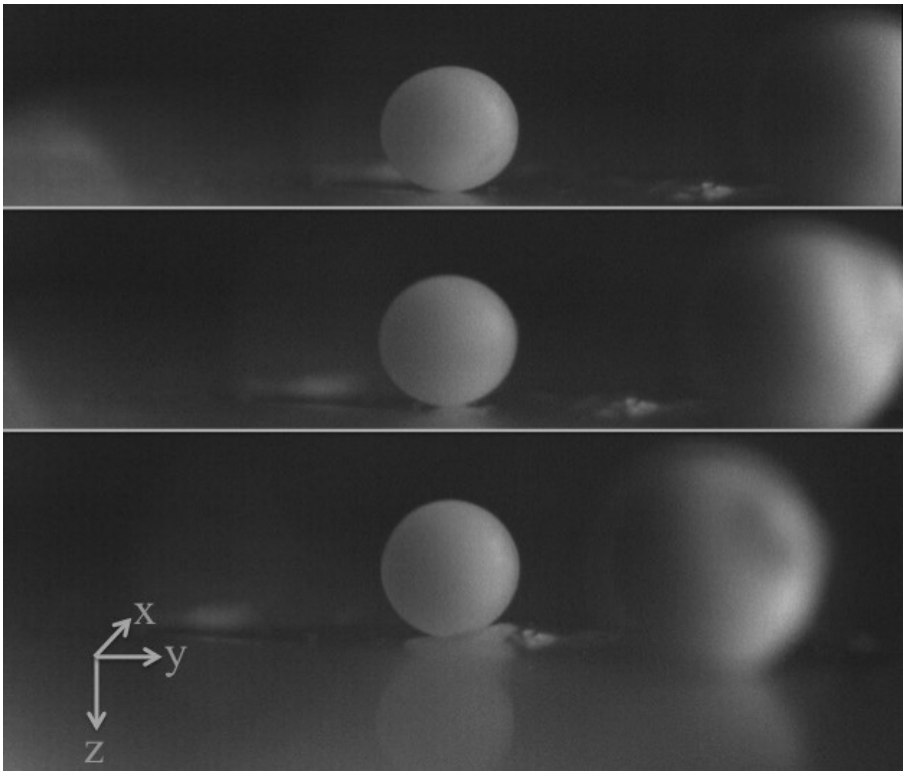

Figure 5.30: Snapshots of a polystyrene sphere trapped radially by a spherical vortex

5.4 Conclusion

In this chapter, we aimed at experimentally trap the elastic spheres using either a focused vortex beam or a spherical vortex beam. To trap and manipulate spheres smaller than 0.2λ, a focused vortex was used. According to our experiments, the focused vortex has successfully selected, trapped the target sphere. And we were able to move the sphere by moving the transducer array.

In the case of a sphere larger than 0.2λ, a spherical vortex beam was introduced. We have tailored the spherical vortex beam by choosing the topological charge and radial degree to ensure a higher pressure gradient in the axial direction, which gives rise to a more significant axial force. Moreover, the trapping zone is large with a radius about 0.5λ, and has a spherical pattern at the center of the beam. This vortex is supposed to be efficient in trapping large spheres. However, the axial trapping for a larger sphere is still challenging as the resonances of the scattering coefficients occur. In order to overcome this difficulty, we have studied the impacts of the resonances and the BSC on the axial restoring force which is the key for axial

trapping. Our analysis demonstrated that the axial restoring force depends highly on the resonances and appears most probably between the resonance peaks. Moreover, the BSC also have an influence on the axial force. By interacting with the scattering coefficient, the BSC affect the amplitude of the negative force. Therefore, the axial trap can be achieved either by choosing the appropriate spheres or adjusting the BSC. Referring to our experiments, despite all the studies we have made, the unknown physical properties of the target spheres make the three-dimensional trapping of a spherical vortex complicated. Moreover, the static force between the polyethylene sphere and the supporting membrane is significant. Even though we have applied the surfactant to reduce the friction, the result was not satisfactory. Furthermore, the polyethylene bead has a very poor sphericity, which also leads to a unpredictable radiation force. With all these practical difficulties, the axial trap was not identified experimentally. Nevertheless, we have observed a firm radial trap during the experiments.

Chapter 6

Conclusions and outlooks

Single beam acoustical tweezers using vortex beams have been developed recently as a powerful device for contactless manipulation. In order to make accurate control of this kind of tweezers, in this thesis, we have addressed two main studies: calibration of the radiation force and synthesis of vortex beams.

The force calibration is based on a three-dimensional model which describes the radiation force exerted on a spherical particles as a function of the expansion coefficients (BSC) and the scattering coefficients of the particle. We have demonstrated that the radiation pressure on a given sphere can be characterized by sampling the pressure field. Three methods were introduced and compared numerically and experimentally in chapter 3. These methods are: quadrature method on a spherical surface, sparse method of an inverse problem at random points in a spherical volume (OMP) and angular spectrum method (ASM) in the focal plane of the acoustical field. We noticed that the OMP and ASM methods can retrieve the BSC with good accuracy both in numerical simulations and experiments. Moreover, the SNR has a significant impact on the results, especially on the axial force. Even a slight noise forming a counterpropagating wave can lead to strong oscillations in the axial force. Therefore, reducing the SNR in the pressure field measurement is of great importance. The ASM, measuring the field at the focal plane of the focused beam, where the intensity is highest, was proven to be the optimal method.

For the wavefield synthesis, we used an array of transducers to emit the desired acoustic field by applying the inverse filtering technique. Two major steps in this method are: firstly, record the wave propagating information in the propagation operator; secondly, calculate the

pseudo-inverse of the propagation operator using SVD method. Each step has an adjustable factor that influences the result. These two factors are the distribution of the control points and the cut-off value.We have employed three distributions with different point spacing and displacements. The force calibration method introduced in chapter 3 was applied to compare the differences of the resulting BSC and radiation forces quantitatively. The comparison of these results demonstrated that it is necessary to use a fine mesh (interval $\approx 0.1\lambda$) to achieve a field that corresponds well with the target field. Moreover, we observed that the distribution of singular values contains information about the sampling quality of the control points. Adequate distribution of control points will result in a group of singular values gathering at a noise level which signifies the over-sampling and is indispensable for a satisfactory field synthesis result. The influence of the cut-off value was also analyzed. But its impacts on the pressure field and the radiation force is not noteworthy. Therefore, the distribution of the control points is the primary factor that influences the results of the field synthesis and special emphasis should be given to choose a suitable mesh. For both a focused vortex and a spherical vortex, we have found an optimal distribution. And the synthesized wavefields were in good agreement with the theoretical ones.

It is noticed that the axial force is always much smaller than the radial force, especially the axial restoring force, which is crucial for the trapping efficiency. Therefore, a spherical vortex was introduced in this work. Compared to a focused vortex, on the one hand, it forms a larger spherical trapping zone (with radius about 0.5λ) at the beam core. Thus, it is capable of trapping larger spheres. On the other hand, the spherical vortex has a higher pressure gradient in the axial direction, which gives rise to a more significant axial restoring force. With these characteristics, the spherical vortex is supposed to create an efficient and selective trap.

With the previous two steps of preparation, we finally arrived at the final step to trap and manipulate the elastic spheres experimentally. For small spheres with radii under 0.2λ, a focused vortex beam was used as a trapping field. During the experiments, a single sphere was trapped firmly in an equilibrium position. Consequently, the sphere can be transported wherever with the movement of the transducer array. For larger spheres with radii about 0.5λ, a spherical vortex beam was used. Nonetheless, as the resonances begin to come up, the axial trap becomes difficult. Although the radial trap is always strong and stable, the axial restoring force is not ensured. To achieve the axial restoring force, we have analyzed the

impact of scattering coefficient resonances as well as the BSC on the axial force. According to our analysis, the axial restoring force depends highly on the resonances and appears between the peaks of the resonances. In the meantime, the BSC can also influence the amplitude of the restoring force. For instance, the restoring force can be enhanced by increasing the aperture angle of the spherical vortex beam. We have tested and chosen the spheres that are highly likely to be trapped for the experiments. However, in our experiments, the axial trap was not observed owing to the complexity of the resonances with unknown physical properties of the target sphere and strong static force between the sphere and the supporting membrane. On the contrary, the radial trap that has been unidentified experimentally is always firm.

Note that at a frequency about 1 MHz, the maximum restoring force exerted by a spherical vortex is about 5 µN, the sphere volume is about 1 mm^3 and our choice of spheres are limited to light polymer spheres with a density comparable to water. The shear velocity of the polymer sphere is low which results in a small shear wavelength and thus the resonances begin at a small size (0.2λ). Besides, the physical properties of polymer spheres are not well characterized. Therefore, the axial trapping is hard to achieve. However, at high frequency, for instance 50 MHz, the size of the trapping zone decreases to a volume with 5 orders of magnitude lower. Particles with denser materials like glass can be used as target spheres. The physical properties of glass are well defined. In addition, the shear velocity of glass is also larger so no resonances appear at the interested size range. Hence the axial trapping is feasible. Consequently, the spherical vortex is much likely to have better selectivity in high frequency which makes it important in micro-metric manipulation.

The calibrated acoustical tweezers has a lot of potential in biological applications. With a trapped sphere, the acoustical tweezers can be used as a real handle. This handle can be attached to an organism to probe its visco-elastic module and even its shear modulus through torsion. In addition, in biological systems, it's important to characterize the radiation force exerted on the target, especially for the *in vivo* samples, since this may influence the vitality of the targets.

Also, acoustical tweezers with high spatial resolution are in need that allows manipulation as cell assemblies, RNA unfolding,etc. This can be achieved by increasing the frequency or improving the field synthesis method. However, the manipulation for particles at or under microscale is very challenging since the acoustic streaming becomes non-negligible or even

acts as a dominating force. Therefore, the studies of acoustic streaming is of importance in these scales. Besides, the manipulation of larger spheres is not easier, as we have explained in this work, the resonances of large sphere leads to unsustainable restoring force. To overcome this difficulty, the analysis of the relationship between the targets' physical properties and the resonances is demanded. Above all, even facing with so many challenges, the potential applications and the noninvasive properties of the acoustical tweezers are always the key drivers for the development of this powerful device.

Bibliography

[1] A. Ashkin, "Acceleration and trapping of particles by radiation pressure," *Phys. Rev. lett.*, vol. 24, no. 4, p. 156, 1970.

[2] A. Ashkin, J. M. Dziedzic, J. Bjorkholm, and S. Chu, "Observation of a single-beam gradient force optical trap for dielectric particles," *Opt. lett.*, vol. 11, no. 5, pp. 288–290, 1986.

[3] A. Ashkin, J. M. Dziedzic, and T. Yamane, "Optical trapping and manipulation of single cells using infrared laser beams," *Nature*, vol. 330, no. 6150, p. 769, 1987.

[4] K. Svoboda and S. M. Block, "Biological applications of optical forces," *Annu Rev Biophys Biomol Struct*, vol. 23, no. 1, pp. 247–285, 1994.

[5] E. J. Peterman, F. Gittes, and C. F. Schmidt, "Laser-induced heating in optical traps," *Biophys. J.*, vol. 84, no. 2, pp. 1308–1316, 2003.

[6] E. A. Abbondanzieri, J. W. Shaevitz, and S. M. Block, "Picocalorimetry of transcription by rna polymerase," *Biophys. J.*, vol. 89, no. 6, pp. L61–L63, 2005.

[7] K. C. Neuman and A. Nagy, "Single-molecule force spectroscopy: optical tweezers, magnetic tweezers and atomic force microscopy," *Nat Methods*, vol. 5, no. 6, p. 491, 2008.

[8] T. Strick, J.-F. Allemand, D. Bensimon, and V. Croquette, "Twisting and stretching single dna molecules," *Prog. Biophys. Mol. Bio.*, vol. 74, no. 1-2, pp. 115–140, 2000.

[9] T. Lionnet, s. Joubaud, R. Lavery, D. Bensimon, and V. Croquette, "Wringing out dna," *Phys. Rev. lett.*, vol. 96, no. 17, p. 178102, 2006.

[10] L. V. King, "On the acoustic radiation pressure on spheres," *Proc. Roy. Soc. Lond. Math. Phys. Sci.*, vol. 147, no. 861, pp. 212–240, 1934.

[11] K. Söllner and C. Bondy, "The mechanism of coagulation by ultrasonic waves," *Trans. Faraday Soc.*, vol. 32, pp. 616–623, 1936.

[12] L. P. Gor'kov, "On the forces acting on a small particle in an acoustical field in an ideal fluid," in *Sov. Phys. Dokl.*, vol. 6, pp. 773–775, 1962.

[13] J. Wu, "Acoustical tweezers," *J. Acoust. Soc. Am.*, vol. 89, no. 5, pp. 2140–2143, 1991.

[14] A. Eller, "Force on a bubble in a standing acoustic wave," *J. Acoust. Soc. Am.*, vol. 43, no. 1, pp. 170–171, 1968.

[15] E. Trinh, "Compact acoustic levitation device for studies in fluid dynamics and material science in the laboratory and microgravity," *Rev Sci Instrum*, vol. 56, no. 11, pp. 2059–2065, 1985.

[16] Y. Tian, R. G. Holt, and R. E. Apfel, "A new method for measuring liquid surface tension with acoustic levitation," *Rev Sci Instrum*, vol. 66, no. 5, pp. 3349–3354, 1995.

[17] J. Weber, C. Rey, J. Neuefeind, and C. Benmore, "Acoustic levitator for structure measurements on low temperature liquid droplets," *Rev Sci Instrum*, vol. 80, no. 8, p. 083904, 2009.

[18] R. Mondragon, L. Hernandez, J. E. Julia, J. C. Jarque, S. Chiva, B. Zaitone, and C. Tropea, "Study of the drying behavior of high load multiphase droplets in an acoustic levitator at high temperature conditions," *Chem. Eng. Sci.*, vol. 66, no. 12, pp. 2734–2744, 2011.

[19] K. Ohsaka and E. Trinh, "Three-lobed shape bifurcation of rotating liquid drops," *Phys. Rev. lett.*, vol. 84, no. 8, p. 1700, 2000.

[20] S. Santesson and S. Nilsson, "Airborne chemistry: acoustic levitation in chemical analysis," *Anal Bioanal Chem*, vol. 378, no. 7, pp. 1704–1709, 2004.

[21] W. Xie, C. Cao, Y. Lü, and B. Wei, "Levitation of iridium and liquid mercury by ultrasound," *Phys. Rev. lett.*, vol. 89, no. 10, p. 104304, 2002.

[22] M. A. Andrade, F. Buiochi, and J. C. Adamowski, "Finite element analysis and optimization of a single-axis acoustic levitator," *IEEE T. Ultrason. Ferr.*, vol. 57, no. 2, pp. 469–479, 2010.

[23] A. Marzo, A. Barnes, and B. W. Drinkwater, "Tinylev: A multi-emitter single-axis acoustic levitator," *Rev Sci Instrum*, vol. 88, no. 8, p. 085105, 2017.

[24] W. Xie and B. Wei, "Parametric study of single-axis acoustic levitation," *Appl. Phys. Lett.*, vol. 79, no. 6, pp. 881–883, 2001.

[25] W. Xie, C. Cao, Y. Lü, Z. Hong, and B. Wei, "Acoustic method for levitation of small living animals," *Appl. Phys. Lett.*, vol. 89, no. 21, p. 214102, 2006.

[26] S. Tran, P. Marmottant, and P. Thibault, "Fast acoustic tweezers for the two-dimensional manipulation of individual particles in microfluidic channels," *Appl. Phys. Lett.*, vol. 101, no. 11, p. 114103, 2012.

[27] J. Shi, D. Ahmed, X. Mao, S. C. S. Lin, A. Lawit, and T. J. Huang, "Acoustic tweezers: Patterning cells and microparticles using standing surface acoustic waves (SSAW)," *Lab on a Chip*, vol. 9, no. 20, pp. 2890–2895, 2009.

[28] O. Dron, C. Ratier, M. Hoyos, and J.-L. Aider, "Parametric study of acoustic focusing of particles in a micro-channel in the perspective to improve micro-piv measurements," *Microfluid Nanofluidics*, vol. 7, no. 6, p. 857, 2009.

[29] D. J. Collins, B. Morahan, J. Garcia-Bustos, C. Doerig, M. Plebanski, and A. Neild, "Two-dimensional single-cell patterning with one cell per well driven by surface acoustic waves," *Nat Commun*, vol. 6, p. 8686, 2015.

[30] T. Laurell, F. Petersson, and A. Nilsson, "Chip integrated strategies for acoustic separation and manipulation of cells and particles," *Chem. Soc. Rev.*, vol. 36, no. 3, pp. 492–506, 2007.

[31] O. Manneberg, B. Vanherberghen, B. Önfelt, and M. Wiklund, "Flow-free transport of cells in microchannels by frequency-modulated ultrasound," *Lab on a Chip*, vol. 9, no. 6, pp. 833–837, 2009.

[32] J. Shi, H. Huang, Z. Stratton, Y. Huang, and T. J. Huang, "Continuous particle separation in a microfluidic channel via standing surface acoustic waves (ssaw)," *Lab on a Chip*, vol. 9, no. 23, pp. 3354–3359, 2009.

[33] X. Ding, S.-C. S. Lin, B. Kiraly, H. Yue, S. Li, I.-K. Chiang, J. Shi, S. J. Benkovic, and T. J. Huang, "On-chip manipulation of single microparticles, cells, and organisms using surface acoustic waves," *P. Natl. Acad. Sci. USA*, vol. 109, no. 28, pp. 11105–11109, 2012.

[34] S. Li, X. Ding, F. Guo, Y. Chen, M. I. Lapsley, S.-C. S. Lin, L. Wang, J. P. McCoy, C. E. Cameron, and T. J. Huang, "An on-chip, multichannel droplet sorter using standing surface acoustic waves," *Anal. Chem.*, vol. 85, no. 11, pp. 5468–5474, 2013.

[35] D. J. Collins, C. Devendran, Z. Ma, J. Ng, A. Neild, and Y. Ai, "Acoustic tweezers via sub–time-of-flight regime surface acoustic waves," *Sci. Adv.*, vol. 2, no. 7, p. e1600089, 2016.

[36] M. Lanoy, C. Derec, A. Tourin, and V. Leroy, "Manipulating bubbles with secondary bjerknes forces," *Appl. Phys. Lett.*, vol. 107, no. 21, p. 214101, 2015.

[37] M. Lanoy, C. Derec, A. Tourin, and V. Leroy, "Manipulating air bubbles with secondary bjerknes forces," *J. Acoust. Soc. Am.*, vol. 139, no. 4, pp. 2153–2153, 2016.

[38] X. Ding, Z. Peng, S.-C. S. Lin, M. Geri, S. Li, P. Li, Y. Chen, M. Dao, S. Suresh, and T. J. Huang, "Cell separation using tilted-angle standing surface acoustic waves," *Proc. Natl. Acad. Sci. U.S.A.*, vol. 111, no. 36, pp. 12992–12997, 2014.

[39] P. Li, Z. Mao, Z. Peng, L. Zhou, Y. Chen, P.-H. Huang, C. I. Truica, J. J. Drabick, W. S. El-Deiry, M. Dao, *et al.*, "Acoustic separation of circulating tumor cells," *Proc. Natl. Acad. Sci. U.S.A.*, vol. 112, no. 16, pp. 4970–4975, 2015.

[40] M. Wu, Y. Ouyang, Z. Wang, R. Zhang, P.-H. Huang, C. Chen, H. Li, P. Li, D. Quinn, M. Dao, *et al.*, "Isolation of exosomes from whole blood by integrating acoustics and microfluidics," *Proc. Natl. Acad. Sci. U.S.A.*, vol. 114, no. 40, pp. 10584–10589, 2017.

[41] F. Petersson, A. Nilsson, C. Holm, H. Jönsson, and T. Laurell, "Continuous separation of lipid particles from erythrocytes by means of laminar flow and acoustic standing wave forces," *Lab on a Chip*, vol. 5, no. 1, pp. 20–22, 2005.

[42] D. Baresch, J.-L. Thomas, and R. Marchiano, "Spherical vortex beams of high radial degree for enhanced single-beam tweezers," *J. Appl. Phys.*, vol. 113, p. 184901, 2013.

[43] X. Chen, K. H. Lam, R. Chen, Z. Chen, P. Yu, Z. Chen, K. K. Shung, and Q. Zhou, "An adjustable multi-scale single beam acoustic tweezers based on ultrahigh frequency ultrasonic transducer," *Biotechnol Bioeng*, vol. 114, no. 11, pp. 2637–2647, 2017.

[44] H. G. Lim, H. H. Kim, C. Yoon, and K. K. Shung, "A one-sided acoustic trap for cell immobilization using 30-mhz array transducer," *IEEE T. Ultrason. Ferr.*, 2019.

[45] D. Baresch, *Acoustic tweezers: trapping and manipulation of an object by radiation pressure of a progressive wave.* PhD thesis, Université Pierre et Marie Curie-Paris, Paris 6, 2014.

[46] D. Baresch, J.-L. Thomas, and R. Marchiano, "Observation of a single-beam gradient force acoustical trap for elastic particles: acoustical tweezers," *Phys. Rev. lett.*, vol. 116, no. 2, p. 024301, 2016.

[47] M. Baudoin, J.-C. Gerbedoen, A. Riaud, O. Bou Matar, N. Smagin, and J.-L. Thomas, "Folding a focalized acoustical vortex on a flat holographic transducer: Miniaturized selective acoustical tweezers," *Sci. Adv.*, vol. 5, p. eaav1967, 2019.

[48] H. He, N. Heckenberg, and H. Rubinsztein-Dunlop, "Optical particle trapping with higher-order doughnut beams produced using high efficiency computer generated holograms," *J Mod Opt*, vol. 42, no. 1, pp. 217–223, 1995.

[49] N. Simpson, K. Dholakia, L. Allen, and M. Padgett, "Mechanical equivalence of spin and orbital angular momentum of light: an optical spanner," *Opt. lett.*, vol. 22, no. 1, pp. 52–54, 1997.

[50] D. G. Grier, "A revolution in optical manipulation," *Nature*, vol. 424, no. 6950, p. 810, 2003.

[51] J. F. Nye and M. V. Berry, "Dislocations in wave trains," *Proc R Soc Lond A Math Phys Sci*, vol. 336, no. 1605, pp. 165–190, 1974.

[52] A. Anhäuser, R. Wunenburger, and E. Brasselet, "Acoustic rotational manipulation using orbital angular momentum transfer," *Phys. Rev. lett.*, vol. 109, no. 3, p. 034301, 2012.

[53] R. Wunenburger, J. I. V. Lozano, and E. Brasselet, "Acoustic orbital angular momentum transfer to matter by chiral scattering," *New J Phys*, vol. 17, no. 10, p. 103022, 2015.

[54] A. H. Mack, D. J. Schlingman, L. Regan, and S. G. J. Mochrie, "Practical axial optical trapping," *Rev. Sci. Instrum.*, vol. 83, no. 10, p. 103106, 2012.

[55] A. R. Carter, Y. Seol, and T. T. Perkins, "Precision surface-coupled optical-trapping assay with one-basepair resolution," *Biophys. J.*, vol. 96, no. 7, pp. 2926–2934, 2009.

[56] N. Malagnino, G. Pesce, A. Sasso, and E. Arimondo, "Measurements of trapping efficiency and stiffness in optical tweezers," *Opt. Commun.*, vol. 214, no. 1-6, pp. 15–24, 2002.

[57] J. Lee, C. Lee, and K. K. Shung, "Calibration of sound forces in acoustic traps," *IEEE T. Ultrason. Ferr.*, vol. 57, no. 10, pp. 2305–2310, 2010.

[58] D. Baresch, J.-L. Thomas, and R. Marchiano, "Orbital angular momentum transfer to stably trapped elastic particles in acoustical vortex beams.," *Phys. Rev. lett.*, vol. 121, no. 07, p. 074301, 2018.

[59] A. A. Doinikov, "Acoustic radiation pressure on a compressible sphere in a viscous fluid," *J. Fluid Mech.*, vol. 267, pp. 1–22, 1994.

[60] K. Yosioka and Y. Kawasima, "Acoustic radiation pressure on a compressible sphere," *ACTA ACUST UNITED AC*, vol. 5, no. 3, pp. 167–173, 1955.

[61] T. Hasegawa and K. Yosioka, "Acoustic-radiation force on a solid elastic sphere," *J. Acoust. Soc. Am.*, vol. 46, no. 5B, pp. 1139–1143, 1969.

[62] T. Embleton, "Mean force on a sphere in a spherical sound field. i.(theoretical)," *J. Acoust. Soc. Am.*, vol. 26, no. 1, pp. 40–45, 1954.

[63] W. L. Nyborg, "Radiation pressure on a small rigid sphere," *J. Acoust. Soc. Am.*, vol. 42, no. 5, pp. 947–952, 1967.

[64] X. Chen and R. E. Apfel, "Radiation force on a spherical object in the field of a focused cylindrical transducer," *J. Acoust. Soc. Am.*, vol. 101, no. 5, pp. 2443–2447, 1997.

[65] P. L. Marston, "Axial radiation force of a bessel beam on a sphere and direction reversal of the force," *J. Acoust. Soc. Am.*, vol. 120, no. 6, pp. 3518–3524, 2006.

[66] P. L. Marston, "Scattering of a bessel beam by a sphere: Ii. helicoidal case and spherical shell example," *J. Acoust. Soc. Am.*, vol. 124, no. 5, pp. 2905–2910, 2008.

[67] P. L. Marston, "Radiation force of a helicoidal bessel beam on a sphere," *J. Acoust. Soc. Am.*, vol. 125, no. 6, pp. 3539–3547, 2009.

[68] G. T. Silva, "An expression for the radiation force exerted by an acoustic beam with arbitrary wavefront (l)," *J. Acoust. Soc. Am.*, vol. 130, no. 6, pp. 3541–3544, 2011.

[69] G. Silva, T. Lobo, and F. Mitri, "Radiation torque produced by an arbitrary acoustic wave," *EPL*, vol. 97, no. 5, p. 54003, 2012.

[70] G. T. Silva and H. Bruus, "Acoustic interaction forces between small particles in an ideal fluid," *Phys. Rev. E*, vol. 90, no. 6, p. 063007, 2014.

[71] L. Zhang, "From acoustic radiation pressure to three-dimensional acoustic radiation forces," *J. Acoust. Soc. Am.*, vol. 144, no. 1, pp. 443–447, 2018.

[72] M. Settnes and H. Bruus, "Forces acting on a small particle in an acoustical field in a viscous fluid," *Phys. Rev. E*, vol. 85, no. 1, p. 016327, 2012.

[73] T. S. Jerome, Y. A. Ilinskii, E. A. Zabolotskaya, and M. F. Hamilton, "Born approximation of acoustic radiation force and torque on soft objects of arbitrary shape," *J. Acoust. Soc. Am.*, vol. 145, no. 1, pp. 36–44, 2019.

[74] D. Baresch, J.-L. Thomas, and R. Marchiano, "Three-dimensional acoustic radiation force on an arbitrarily located elastic sphere," *J. Acoust. Soc. Am.*, vol. 133, no. 1, pp. 25–36, 2013.

[75] L. Rayleigh, "Xlii. on the momentum and pressure of gaseous vibrations, and on the connexion with the virial theorem," *The London, Edinburgh, and Dublin Philosophical Magazine and Journal of Science*, vol. 10, no. 57, pp. 364–374, 1905.

[76] B. P., "Les ondes ultra-sonores," *Revue d'Acoustique*, vol. 1, pp. 93–109, 1932.

[77] G. Hertz and H. Mende, "Acoustic radiation pressure in liquids," *Z. Physik*, no. 114, 1939.

[78] L. Brillouin, "Sur les tensions de radiation," *Ann. Phys. X*, vol. 4, pp. 528–586, 1925.

[79] L. Brillouin, "Les tensions de radiation ; leur interprétation en mécanique classique et en relativité," *Journal de Physique et le Radium*, vol. 6, no. 11, pp. 337–353, 1925.

[80] L. Brillouin, *Tensors in mechanics and elasticity.* Academic Press, New York, 1964, 1938.

[81] L. Landau and E. Lifshitz, *Fluid Mechanics.* New York: Pergamon, 1959.

[82] K. Beissner, "The acoustic radiation force in lossless fluids in eulerian and lagrangian coordinates," *J. Acoust. Soc. Am.*, vol. 103, no. 5, pp. 2321–2332, 1998.

[83] K. Beissner, "Acoustic radiation pressure in the near field," *J Sound Vib*, vol. 93, no. 4, pp. 537–548, 1984.

[84] K. Beissner, "Two concepts of acoustic radiation pressure," *J. Acoust. Soc. Am.*, vol. 79, no. 5, pp. 1610–1612, 1986.

[85] V. Anderson, "Sound scattering from a fluid sphere," *J. Acoust. Soc. Am.*, vol. 22, pp. 426–431, 1950.

[86] J. J. Faran Jr, "Sound scattering by solid cylinders and spheres," *J. Acoust. Soc. Am.*, vol. 23, no. 4, pp. 405–418, 1951.

[87] P. Epstein and R. Carhart, "The absorption of sound in suspensions and emulsions. i. water fog in air.," *J. Acoust. Soc. Am.*, vol. 25, no. 3, pp. 553–565, 1953.

[88] J. Allegra and S. Hawley, "Attenuation of sound in suspensions and emulsions: Theory and experiments," *J. Acoust. Soc. Am.*, vol. 51, no. 5, pp. 1545–1564, 1971.

[89] N. Einspruch, E. Witterholt, and R. Truell, "Scattering of a plane transverse wave by a spherical obstacle in an elastic medium," *J. Appl. Phys.*, vol. 31, no. 5, pp. 806–818, 1960.

[90] P. Waterman, "New formulation of acoustic scattering," *J. Acoust. Soc. Am.*, vol. 45, no. 6, pp. 1417–1429, 1969.

[91] P. Waterman, "Matrix theory of elastic wave scattering," *J. Acoust. Soc. Am.*, vol. 60, no. 3, pp. 567–580, 1976.

[92] D. Royer and E. Dieulesaint, *Ondes élastiques dans les solides*. Elsevier Masson, 1996.

[93] I. Gradshteyn and I. Ryzhik, *Table of Integrals, Series, and Products*, ch. 8. Burlington: Elsevier, 7 ed., 2007.

[94] M. Abramowitz and I. Stegun, *Handbook of mathematical functions*, ch. 8-9. New York: Dover Publications, 1965.

[95] J. Stratton, *Electromagnetic Theory*, ch. 6-7. New York: McGraw-Hill, 1941.

[96] A. Marzo, S. A. Seah, B. W. Drinkwater, D. R. Sahoo, B. Long, and S. Subramanian, "Holographic acoustic elements for manipulation of levitated objects," *Nat Commun*, vol. 6, p. 8661, 2015.

[97] B. T. Hefner and P. L. Marston, "An acoustical helicoidal wave transducer with applications for the alignment of ultrasonic and underwater systems," *J. Acoust. Soc. Am.*, vol. 106, no. 6, pp. 3313–3316, 1999.

[98] R. Marchiano and J.-L. Thomas, "Synthesis and analysis of linear and nonlinear acoustical vortices," *Phys. Rev. E*, vol. 71, no. 6, p. 066616, 2005.

[99] L. Rayleigh, "On the circulation of air observed in kundt's tubes, and on some allied acoustical problems," *Philos. Trans. Royal Soc.*, vol. 175, pp. 1–21, 1884.

[100] D. Baltean-Carlès, V. Daru, C. Weisman, S. Tabakova, and H. Bailliet, "An unexpected balance between outer rayleigh streaming sources," *J. Fluid Mech.*, vol. 867, pp. 985–1011, 2019.

[101] H. Schlichting, "Berechnung ebener periodischer grenzschichtstromungen," *Phys. z.*, vol. 33, pp. 327–335, 1932.

[102] J. T. Karlsen and H. Bruus, "Forces acting on a small particle in an acoustical field in a thermoviscous fluid," *Phys. Rev. E*, vol. 92, no. 4, p. 043010, 2015.

[103] F. Busse and T. Wang, "Torque generated by orthogonal acoustic waves—theory," *J. Acoust. Soc. Am.*, vol. 69, no. 6, pp. 1634–1638, 1981.

[104] D. Foresti and D. Poulikakos, "Acoustophoretic contactless elevation, orbital transport and spinning of matter in air," *Phys. Rev. lett.*, vol. 112, no. 2, p. 024301, 2014.

[105] I. Bernard, A. A. Doinikov, P. Marmottant, D. Rabaud, C. Poulain, and P. Thibault, "Controlled rotation and translation of spherical particles or living cells by surface acoustic waves," *Lab on a Chip*, vol. 17, no. 14, pp. 2470–2480, 2017.

[106] K. Volke-Sepúlveda, A. O. Santillán, and R. R. Boullosa, "Transfer of angular momentum to matter from acoustical vortices in free space," *Phys. Rev. lett.*, vol. 100, no. 2, p. 024302, 2008.

[107] K. Skeldon, C. Wilson, M. Edgar, and M. Padgett, "An acoustic spanner and its associated rotational doppler shift," *New J Phys*, vol. 10, no. 1, p. 013018, 2008.

[108] C. Eckart, "Vortices and streams caused by sound waves," *Phys. Rev.*, vol. 73, no. 1, p. 68, 1948.

[109] T. Brunet, J.-L. Thomas, R. Marchiano, and F. Coulouvrat, "Experimental observation of azimuthal shock waves on nonlinear acoustical vortices," *New J Phys*, vol. 11, no. 1, p. 013002, 2009.

[110] C. H. L. Beentjes, "Quadrature on a spherical surface," *Working note available on the website http://people. maths. ox. ac. uk/beentjes/Essays*, 2015.

[111] S. L. Sobolev, "Cubature formulas on the sphere invariant under finite groups of rotations," in *Selected Works of SL Sobolev*, pp. 461–466, Springer, 2006.

[112] B. Rafaely, "The spherical-shell microphone array," *IEEE T. Audio Speech*, vol. 16, no. 4, pp. 740–747, 2008.

[113] R. S. Womersley, "Efficient spherical designs with good geometric properties," in *Contemporary Computational Mathematics-A Celebration of the 80th Birthday of Ian Sloan*, pp. 1243–1285, Springer, 2018.

[114] T. T. Cai and L. Wang, "Orthogonal matching pursuit for sparse signal recovery with noise," *IEEE T. Inform. Theory*, vol. 57, no. 7, pp. 4680–4688, 2011.

[115] Y. C. Eldar, P. Kuppinger, and H. Bolcskei, "Block-sparse signals: Uncertainty relations and efficient recovery," *IEEE T. Signal Proces.*, vol. 58, no. 6, pp. 3042–3054, 2010.

[116] O. A. Sapozhnikov and M. R. Bailey, "Radiation force of an arbitrary acoustic beam on an elastic sphere in a fluid," *J. Acoust. Soc. Am.*, vol. 133, no. 2, pp. 661–676, 2013.

[117] C. R. Courtney, C. E. Demore, H. Wu, A. Grinenko, P. D. Wilcox, S. Cochran, and B. W. Drinkwater, "Independent trapping and manipulation of microparticles using dexterous acoustic tweezers," *Appl. Phys. Lett.*, vol. 104, no. 15, p. 154103, 2014.

[118] J.-L. Thomas and R. Marchiano, "Pseudo angular momentum and topological charge conservation for nonlinear acoustical vortices," *Phys. Rev. lett.*, vol. 91, no. 24, p. 244302, 2003.

[119] N. Jiménez, R. Picó, V. Sánchez-Morcillo, V. Romero-García, L. M. García-Raffi, and K. Staliunas, "Formation of high-order acoustic bessel beams by spiral diffraction gratings," *Phys. Rev. E*, vol. 94, no. 5, p. 053004, 2016.

[120] R. D. Muelas-Hurtado, J. L. Ealo, J. F. Pazos-Ospina, and K. Volke-Sepúlveda, "Generation of multiple vortex beam by means of active diffraction gratings," *Appl. Phys. Lett.*, vol. 112, no. 8, p. 084101, 2018.

[121] J. L. Ealo, J. C. Prieto, and F. Seco, "Airborne ultrasonic vortex generation using flexible ferroelectrets," *IEEE T. Ultrason. Ferr.*, vol. 58, no. 8, pp. 1651–1657, 2011.

[122] A. Riaud, M. Baudoin, O. B. Matar, L. Becerra, and J.-L. Thomas, "Selective manipulation of microscopic particles with precursor swirling rayleigh waves," *Phys. Rev. App.*, vol. 7, no. 2, p. 024007, 2017.

[123] Y. Jin, R. Kumar, O. Poncelet, O. Mondain-Monval, and T. Brunet, "Flat acoustics with soft gradient-index metasurfaces," *Nat Commun*, vol. 10, no. 1, p. 143, 2019.

[124] S. Gspan, A. Meyer, S. Bernet, and M. Ritsch-Marte, "Optoacoustic generation of a helicoidal ultrasonic beam," *J. Acoust. Soc. Am.*, vol. 115, no. 3, pp. 1142–1146, 2004.

[125] M. Fink, "Time reversal of ultrasonic fields. i. basic principles," *IEEE T. Ultrason. Ferr.*, vol. 39, no. 5, pp. 555–566, 1992.

[126] M. Tanter, J.-L. Thomas, and M. Fink, "Time reversal and the inverse filter," *J. Acoust. Soc. Am.*, vol. 108, no. 1, pp. 223–234, 2000.

[127] P. Wu, R. Kazys, and T. Stepinski, "Optimal selection of parameters for the angular spectrum approach to numerically evaluate acoustic fields," *J. Acoust. Soc. Am.*, vol. 101, no. 1, pp. 125–134, 1997.

[128] X. Zeng and R. J. McGough, "Optimal simulations of ultrasonic fields produced by large thermal therapy arrays using the angular spectrum approach," *J. Acoust. Soc. Am.*, vol. 125, no. 5, pp. 2967–2977, 2009.